

The role of planetary waves in coupling processes of the middle atmosphere

Dissertation
zur
Erlangung des akademischen Grades
doctor rerum naturalium (Dr. rer. nat.)
der Mathematisch-Naturwissenschaftlichen Fakultät
der Universität Rostock



vorgelegt von
Vivien Matthias, geb. am 05.09.1984 in Berlin, Deutschland
Rostock, November 2013

Betreuer: Prof. Dr. M. Rapp (Ludwig-Maximilians-Universität München)

Gutachter: Prof. Dr. M. Rapp (Ludwig-Maximilians-Universität München)
Prof. Dr. Ch. Jacobi (Universität Leipzig)

eingereicht am: 22. November 2013

verteidigt am: 31. März 2014

Abstract

The coupling of the middle atmosphere is influenced especially during winter by Planetary Waves (PWs). The most impressive vertical coupling process in the middle atmosphere, caused by the interaction of PWs with the mean flow, is the Sudden Stratospheric Warming (SSW), mainly occurring in the northern hemisphere. During the SSW a sudden warming of up to 80 K occurs in the stratosphere within a few days with a simultaneous cooling in the mesosphere and a wind reversal to westward winds in the middle atmosphere. The average behavior of major SSWs at polar latitudes is investigated by combining high-resolution local radar measurements with global satellite observations and assimilated model data. The results show a distinctively stronger PW activity in the mesosphere during major SSWs compared to minor warmings. Normally, SSWs occur strongest at high polar latitudes, become weaker towards the south and vanish at mid-latitudes. However, there are events which are southward extended or shifted. A comparison of a normal polar dominated SSW with three latitudinally displaced events shows a continuous westward wind band from the pole to the lower latitudes in the stratosphere during the latitudinally displaced SSWs. This effect and the southward extended warming are in connection with an increased PW activity between 30°N and 50°N and a changed stationary wave flux in the stratosphere compared to the normal SSW. A second coupling process, occurring nearly every second year during the fall transition, is the so called Hiccup. It shows very similar effects on average like a SSW but with a distinctively smaller magnitude. In contrast to the SSW, an upward propagation of the wind and temperature changes is observed and the assumption, that the Hiccup is caused by the sudden turn-on of the PW activity, is confirmed.

Zusammenfassung

Die Kopplung der mittleren Atmosphäre wird vor allem im Winter von planetaren Wellen (PW) beeinflusst. Der beeindruckendste vertikale Kopplungsprozess, der durch die Wechselwirkung von PW mit dem Grundstrom verursacht wird, ist die plötzliche Stratosphärenenerwärmung (SSW), die vorrangig in der nördlichen Hemisphäre auftritt. Während einer SSW erwärmt sich die Stratosphäre innerhalb weniger Tage um bis zu 80 K bei einer gleichzeitigen Abkühlung der Mesosphäre und einer Windumkehr auf westwärtigen Wind in der mittleren Atmosphäre. Das mittlere Verhalten von starken SSWs wird untersucht mittels einer Kombination aus hochaufgelösten lokalen Radarmessungen mit globalen Satellitenbeobachtungen und assimilierten Modelldaten. Die Ergebnisse zeigen eine deutlich größere PW-Aktivität in der Mesosphäre während starker SSWs als während schwacher SSWs. Normalerweise treten SSWs am stärksten am Pol auf, werden nach Süden hin schwächer und enden in den mittleren Breiten. Dennoch gibt es Ereignisse, die nach Süden ausgedehnt oder verschoben sind. Ein Vergleich einer normalen polar-dominierenden SSW mit drei breitenverschobenen Ereignissen zeigt ein kontinuierliches westwärts Windband vom Pol zu niedrigen Breiten während der breitenverschobenen SSWs. Dieser Effekt und die südlich ausgedehnte Erwärmung stehen in Verbindung mit einer erhöhten PW-Aktivität zwischen 30°N und 50°N und einem veränderten stationären Wellenfluss im Vergleich zur normalen SSW. Ein zweiter

Kopplungsprozess, der fast alle zwei Jahre während der Herbstumstellung auftritt, ist der sogenannte „Hiccup“ (Schluckauf). Er zeigt im Mittel ähnliche Effekte wie die SSW, wenn auch mit bedeutend kleinerer Magnitude. Im Gegensatz zur SSW wurde ein Aufwärtspropagieren der Wind- und Temperaturänderungen beobachtet und es konnte die Vermutung verifiziert werden, dass der Hiccup durch das plötzliche Auftreten der PW-Aktivität verursacht wird.

Contents

1	Introduction	1
2	Planetary waves and their general characteristics	4
2.1	Generation mechanism of PWs	6
2.2	Horizontal propagation	10
2.3	Charney-Drazin Criterion	11
2.4	Dispersion relation	12
2.5	Wave-mean flow interaction	13
3	Instruments, models and data interpretation methods	14
3.1	Radar	14
3.1.1	Meteor radar	14
3.1.2	MF radar	15
3.2	Microwave Limb Sounder onboard the Aura satellite	16
3.3	Model data	18
3.3.1	ECMWF	18
3.3.2	MERRA	19
3.3.3	CMAM20	19
3.4	Data interpretation methods	21
3.4.1	Estimation of the prevailing wind	21
3.4.2	Wavelet analysis	21
3.4.3	Spectral analysis of space-time series	22
3.4.4	The three-dimensional Plumb flux	24
4	Seasonal and year-to-year variability of PW activity	26
4.1	Seasonal variability of PWs	26
4.2	Year-to-year variability of PWs	30
5	SSWs: State of the art and objectives of this thesis	33
6	Characteristics of PWs during Sudden Stratospheric Warmings	41
6.1	Composite analysis of the temporal development of PWs during SSWs	42
6.2	Latitudinal variabilities of SSWs	48
6.2.1	Zonal wind characteristics	48
6.2.2	Temperature characteristics	51
6.2.3	PW characteristics	54

Contents

6.2.4	Extended discussion	59
6.3	Longitudinal variability of SSWs	63
7	Characteristics of the “Hiccup” of the fall transition	69
7.1	The Hiccup during fall 2006	69
7.2	Composite analysis of the temporal development of the Hiccup	72
7.3	Hiccup vs. SSW	75
8	Summary and Outlook	78
	Appendix A The quasi-geostrophic potential vorticity equation	81
	Appendix B The three-dimensional Plumb flux	84
	Appendix C Tables	90
	Bibliography	91
	Acknowledgements	103
	Curriculum Vitae	104

List of Symbols

a	Earth radius
β	Gradient of Coriolis parameter f ($\beta = \frac{\partial f}{\partial y}$)
c	Phase velocity
f, f_0	Coriolis parameter
H	Scale height
k, l, m	Zonal/ meridional/ vertical wavenumber in cartesian coordinates
λ	Longitude
N	Brunt-Väisälä frequency
ω	Frequency
Ω	Earth's angular velocity
p	Pressure
ϕ	Latitude
ψ	Streamfunction
Ψ	Geopotential
q	Potential vorticity
R	Gas constant
ρ	Density
s	Zonal wavenumber in spherical coordinates
S'	Nonconverging terms
t	Time
T	Temperature
θ	Potential temperature
θ_0	Reference potential temperature
$\vec{u} = (u, v, w)$	Wind vector with zonal, meridional and vertical component
$\vec{u}_g = (u_g, v_g)$	Geostrophic wind vector
$\vec{u}_a = (u_a, v_a, w_a)$	Ageostrophic wind vector
ξ	Relative vorticity
x, y, z	Cartesian coordinates
$(\bar{\quad})$	Zonal mean
$(\quad)'$	Deviation from the zonal mean

Chapter 1 Introduction

The middle atmosphere covers the height range between 12 and 100 km and includes the stratosphere ($\sim 12 - 50$ km) and the mesosphere ($\sim 50 - 100$ km). The distinction of the different layers is based on the vertical temperature structure of the atmosphere. The temperature increases throughout the stratosphere. The maximum at about 50 km altitude represents the stratopause, the boundary between the stratosphere and the mesosphere (see Figure 1.1). The mesospheric temperature decreases again and minimizes at temperature values as low as ~ 130 K in polar summer. This minimum is called the mesopause and defines the boundary between the mesosphere and the overlying thermosphere.

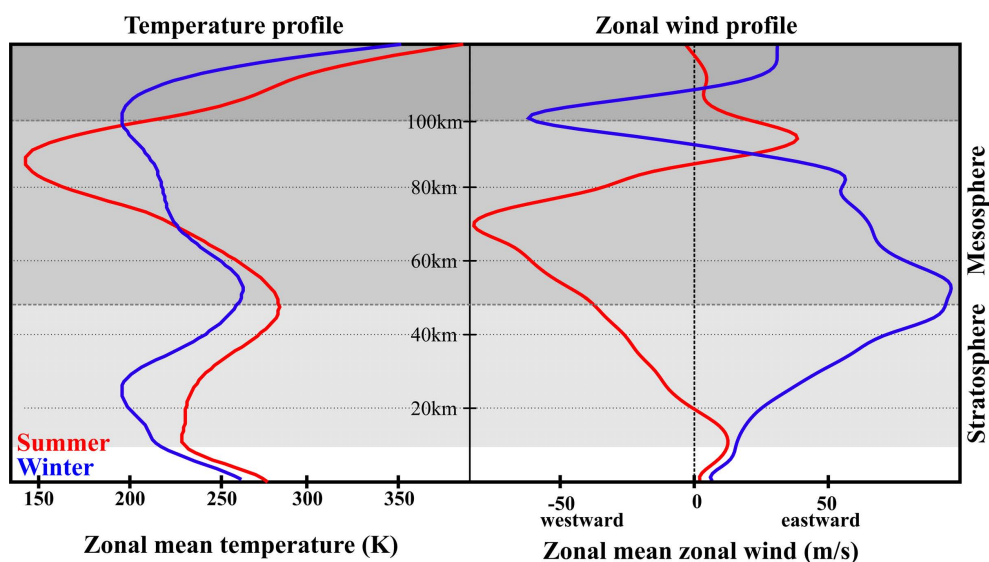


Figure 1.1 Zonal mean temperature profile from MSIS and zonal mean zonal wind profile from HWM07 for mean summer and winter at 70°N .

Figure 1.1 shows the typical zonal mean temperature and zonal mean zonal wind profiles of summer and winter at polar latitudes (70°N) from the empirical models MSIS¹ and HWM07². The mean temperature profiles for summer and winter are structurally similar. However, the summer mesosphere shows distinctively lower temperatures than

¹Mass-Spectrometer-Incoherent-Scatter (MSIS) model from NASA, see *Picone et al. (2002)*

²Horizontal Wind Model (HWM07), see *Drob et al. (2008)*

Chapter 1 Introduction

the winter mesosphere, even though the model temperatures during summer are higher than the average observed data (e.g., *Lübken et al.*, 1999). This behavior is in contrast to the presumption that the summer is warmer than the winter due to the higher solar radiation. This anomaly cannot be explained without the knowledge of atmospheric waves. These waves are characterized by their periods and by their spatial extensions. Locally generated gravity waves with periods of minutes to some hours and horizontal extensions from a few km up to about 1000 km are responsible to drive a meridional circulation from the summer to the winter pole in the mesosphere. They induce an upwelling of air masses above the summer pole and a downwelling above the winter pole. Especially during the winter months, these processes are influenced by Planetary Waves (PW) with a global extension and with periods between 2 and 30 days. PWs are excited by large scale airflow over orography, sea-land differences or baroclinic instability. Their restoring force is the latitudinal variation of the Coriolis force. The propagation of PWs depends strongly on the mean flow, i.e., they can only propagate upward if the mean flow is eastward and not too strong (*Charney and Drazin*, 1961). Thus, most PWs are generated in the troposphere and propagate upward into the mesosphere if the prevailing conditions permit. The mean zonal wind profiles in Figure 1.1 show therefore that the upward propagation of PWs is only possible during winter months but not in summer. Nevertheless, the summer mesosphere is disturbed by planetary 2- and 5-day waves which are generated in-situ in the lower mesosphere by baroclinic instability (e.g., *Plumb*, 1983). They can propagate upward from the lower mesosphere due to the wind reversal to eastward winds in the mesosphere during summer (e.g., *Geller*, 1983).

This PW activity can induce vertical coupling processes between the layers of the middle atmosphere. Vertical coupling processes in the middle atmosphere are a main topic of current geophysical research since they can also influence the troposphere and therefore our weather and climate (e.g., *Baldwin and Dunkerton*, 2001; *Polvani and Waugh*, 2004).

The most impressive and prominent vertical coupling process in the middle atmosphere due to PWs is the Sudden Stratospheric Warming (SSW). It was discovered by *Scherhag* (1952). SSWs are observed in the winter polar stratosphere and are characterized by a warming in the stratosphere with a simultaneous cooling in the mesosphere and a wind reversal to summerly westward winds in the middle atmosphere. The generally accepted reason for the SSW is the interaction of upward propagating PWs with the mean flow as first stated by *Matsuno* (1971). Matsuno's model divided the SSW into two phases. The first phase includes the interaction of upward propagating transient PWs with the mean flow and the second phase explains the temperature changes in the stratosphere and mesosphere. This model was a pioneering work. Over the decades, the SSW model was extended and improved by many studies (e.g., *Holton*, 1976; *Yoden et al.*, 1999; *Liu and Roble*, 2002; *Charlton et al.*, 2007; *Zülicke and Becker*, 2013). Nevertheless, there are still open questions and uncertainties which are not explained by models. One of these uncertainties is the altitude range in which the PWs interact with the mean flow. After Matsuno, the PWs interact with the mean flow in the upper stratosphere/lower mesosphere. However, observations (e.g., *Gregory and Manson*, 1975; *Hoffmann et al.*, 2002) show a wind reversal also in the Mesosphere/Lower Ther-

mosphere (MLT) region which leads to the hypothesis of an interaction of PWs with the mean flow also in this height region.

Another uncertainty is the latitudinal extension of SSW effects (e.g., the wind reversal). Most model simulations (e.g., *Charlton and Polvani, 2007*) and observations (e.g., *Hoffmann et al., 2007*) show that the SSWs are strongest at high polar latitudes, become weaker towards the South and vanish at mid-latitudes. However, recent studies of *Stober et al. (2012)* show stronger westward winds at mid than at polar latitudes during the SSW of 2010. Furthermore, *Chen et al. (2012)* even observed a continuous westward wind band between the pole and the subtropics.

The second vertical coupling process which is studied in this thesis, occurs during the transition period and is called the Hiccup. It shows similar effects like a SSW but with a distinctively smaller magnitude. The Hiccup was first observed by *Shepherd et al. (1999)* during the spring transition. Since then, only a few studies concerning the disturbance of the spring and fall transition have been published (e.g., *Taylor et al., 2001*; *Liu et al., 2001*). Different from the SSWs, the Hiccup is assumed to occur due to the sudden turn-on or turn-off of the PW activity.

The aim of this thesis is to improve our process understanding of the role of PWs in the two vertical coupling processes SSW and Hiccup. The main objectives of this thesis are the qualitative characterization of the following three aspects of these coupling processes: the altitudinal extent of the coupling between PWs and the mean flow, the latitudinal extent of SSW effects in general, and finally the general properties of the so far poorly studied Hiccup. To investigate the altitude range in which PWs interact with the mean flow, the average behavior of wind, temperature and PW activity in the middle atmosphere is studied by combining high-resolution local radar measurements and global satellite observations. The latitudinal extension of SSW effects is investigated by comparing the latitudinal behavior of wind, temperature and PWs between a normal polar dominated SSW, where the event in 2006 was chosen as a representative case, and three latitudinally displaced SSWs in 2009, 2010 and 2012. The characteristics of the Hiccup of the fall transition are studied by investigations of the mean wind, temperature and PW behavior in the lower and middle atmosphere. A comparison of the Hiccup and the SSW reveals similarities and differences of these two vertical coupling processes.

To address these main objectives, this thesis is organized as follows: Chapter 2 gives an overview of the PW theory and the basic characteristics of PWs. The here used instruments and methods are described in chapter 3. The seasonal and year-to-year variability of PW activity is shown in chapter 4. The state of the art of our current knowledge about SSWs is discussed in chapter 5. The altitudinal and latitudinal characteristics of PWs during SSW are studied in chapter 6. Characteristics of the Hiccup of the fall transition are investigated and compared with SSWs in chapter 7. Finally, the most important results of this thesis are summarized and perspectives for future work are discussed in chapter 8.

Chapter 2 Planetary waves and their general characteristics

Planetary waves (PWs) strongly influence the general circulation of the middle atmosphere. They can transport momentum horizontally and vertically over large distances from the wave source to the region where they break (e.g., *Holton and Alexander, 2000*). However, due to their phase speed which has the same order of magnitude as the mean wind velocity, their propagation ability depends on the mean flow (e.g., *Forbes, 1995*). This chapter first introduces how PWs look like in the real atmosphere. Then, the PW generation mechanism as well as the general PW characteristics are described.

How can one imagine a PW? Figure 2.1 schematically shows PWs in the northern hemisphere. A PW manifests itself in large (planetary) scale oscillation of temperatures, wind, pressure, density or trace gas distributions. These oscillations may propagate (e.g., *Pancheva et al., 2008a; Stober et al., 2012; Matthias et al., 2013*). The zonal wavenumber s of a PW is simply defined as the number of minima (maxima) along a latitudinal circle, i.e., Figure 2.1 shows on the left a PW with wavenumber $s = 1$ and on the right with $s = 2$.

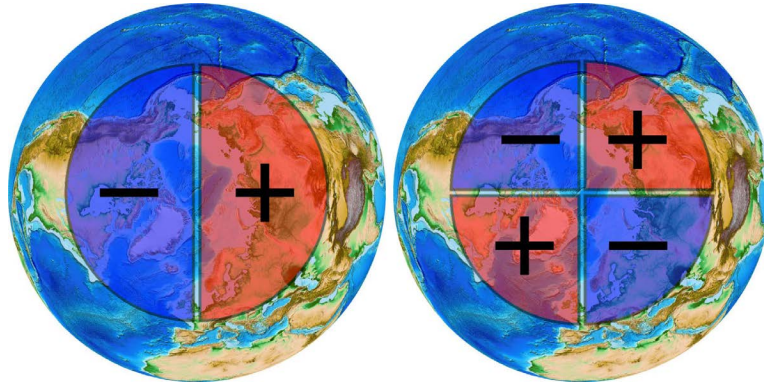


Figure 2.1 Schematic of a PW with the wavenumber $s = 1$ (left) and $s = 2$ (right).

A PW signature from global satellite temperature measurements on January 1st 2013 is shown in Figure 2.2(a). A huge cold area occurs in the western hemisphere while in the eastern hemisphere much higher temperatures dominate, i.e., here we see

a PW with wavenumber one. Considering only one latitude ϕ , here $\phi = 70^\circ\text{N}$, the temperature variation along the longitude (black line in Figure 2.2(b)) shows a clear wave-like structure.

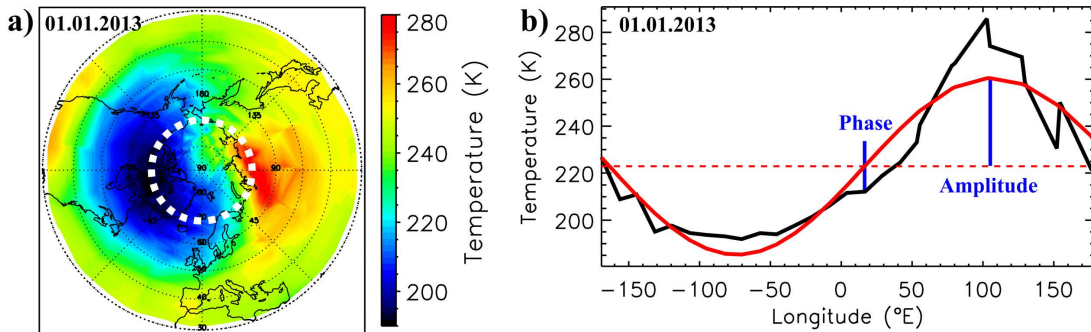


Figure 2.2 a): Example of a planetary temperature oscillation observed on 01.01.2013 in global satellite data (MLS¹) at an altitude of 40 km. The white dashed circle marks the latitude 70°N. **b):** Temperature variation as a function of longitude at 70°N (black) along with a harmonic fit (red) on 01.01.2013.

In general, PWs can be described in spherical coordinates by the wave function

$$u(t, \lambda) = A \sin(\omega t - s\lambda) + B \cos(\omega t - s\lambda) \quad (2.1)$$

where t is the time, λ the longitude, ω the frequency and s the wavenumber. Thus, fitting equation (2.1) to the measured temperature curve (black line in Figure 2.2(b)) gives an idealized wave (red curve). The amplitude of the wave is the maximum distance from the mean state (red dashed line) and can be calculated as $\sqrt{A^2 + B^2}$. Likewise, the phase of the wave during the zero-crossing (red dashed line) can be computed as $\arctan(B/A)$.

PWs can be classified roughly into four different types: transient, stationary and standing waves and oscillations. Figure 2.3 schematically shows these four wave types for the case of the northern hemisphere.

Transient PWs are waves whose phase depends on the longitude, i.e., they have a nonzero wavenumber. They propagate eastward or westward around the globe with the frequency ω .

Stationary PWs are stationary with respect to the longitude. Their frequency is zero since they do not propagate but their wavenumber s is non zero.

A standing PW is a superposition of two equal transient PWs ($s_1 = s_2$) which propagate in opposite directions. The resulting wave has nodes at fixed longitudes and is oscillating in between with the frequency $\omega = \omega_1 = \omega_2$. Such a PW type is rather unlikely due to the filtering effect of the zonal wind.

The oscillation is a special form of a PW. It oscillates in time with the same phase at all longitudes. Therefore, the frequency of an oscillation is nonzero while the wavenumber is zero. Hence, an oscillation does not move with respect to the longitude but with

¹Microwave Limb Sounder (MLS) onboard the Aura satellite. See section 3.2 for details.

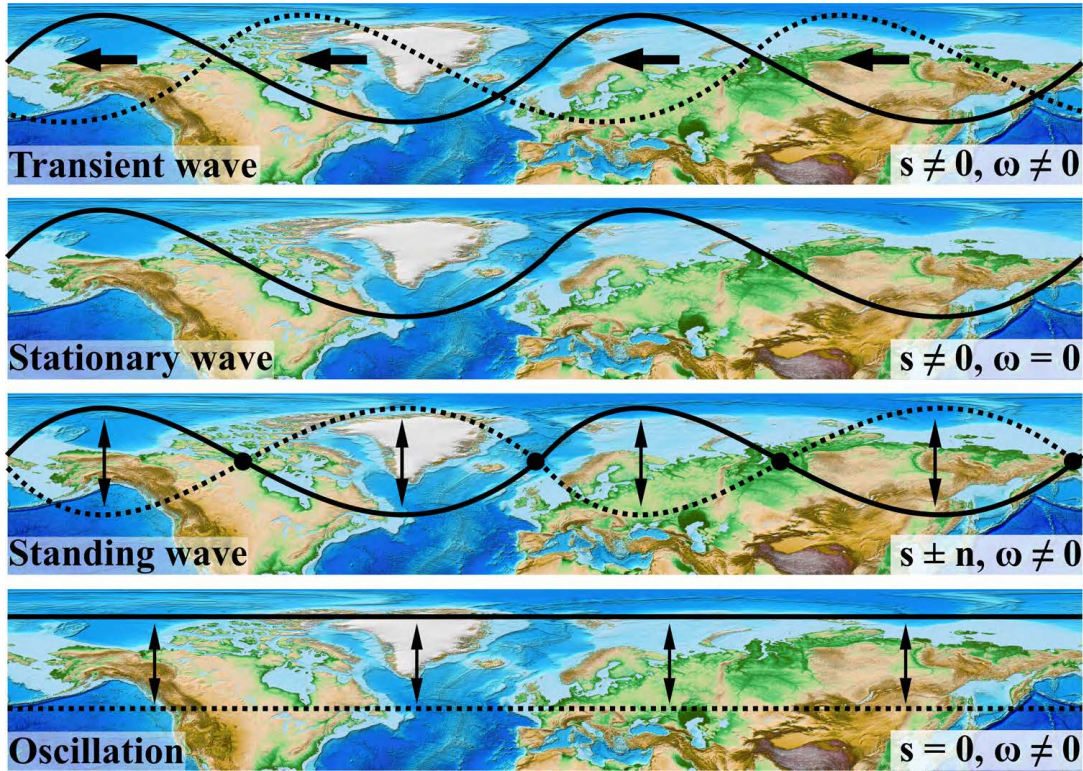


Figure 2.3 Schematic representation of the different planetary wave types.

respect to the latitude as shown in Figure 2.3. As an example, one may imagine the expansion and contraction of the polar vortex.

Another possibility to classify PWs is by their generation mechanism. The two most famous subclasses of PWs are tides, which are generated by the diurnal thermal heating of the atmosphere due to the absorption of the solar radiation, and planetary Rossby waves. They are generated due to big mountains, land-sea contrasts or adiabatic processes. The restoring force is the latitudinal variation of the Coriolis parameter (e.g., *Andrews et al.*, 1987). Planetary Rossby waves are named after their discoverer Carl-Gustaf Rossby (*Rossby*, 1939). In this thesis only planetary Rossby waves, hereafter PW in short, are considered with respect to vertical coupling processes in the middle atmosphere. In the following, the generation mechanism of these PWs is illustrated and general characteristics are presented.

2.1 Generation mechanism of PWs

The dynamics of the Earth's atmosphere is described by the equation of motion in a rotating frame (i.e., Navier-Stokes equation). To study the generation mechanism and the general characteristics of PWs this set of equations is far too complicated and not feasible. Therefore, a few approximations are made. First, a scale analysis leads to the primitive equations (e.g., *Andrews et al.*, 1987). Furthermore, a geometrical sim-

2.1 Generation mechanism of PWs

plification and a dynamical approximation is applied to this still complicated set of equations.

The geometrical simplification replaces the spherical coordinates (λ, ϕ) with the eastward and northward cartesian coordinates (x, y) and restricts the flow to a latitude band, i.e., to a plane. Therefore, the Coriolis parameter f is now

$$f = f_0 + \beta y \quad (2.2)$$

where $f_0 = 2\Omega \sin \phi$ and $\beta = \partial f / \partial y = 2\Omega a^{-1} \cos \phi$. This linear variation of f with y , which reflects the variation of the Coriolis force with latitude, is called the ‘‘beta-effect’’ (Rossby, 1939). This simplification is also called the ‘‘beta-plane approximation’’.

The second dynamical approximation uses the fact that only a large-scale and low frequency flow in the extratropics is considered. Under these approximations, the atmosphere is approximately described by the concept of geostrophic balance, i.e., the Coriolis effect is roughly balanced by the vertical component of the geopotential. Thus, the horizontal wind (u, v) may be approximated by the geostrophic wind (u_g, v_g) which flows in parallel to the isobars. The geostrophic wind is defined by the geostrophic streamfunction ψ as follows:

$$u_g = -\frac{\partial \psi}{\partial y} \quad \text{and} \quad v_g = \frac{\partial \psi}{\partial x} \quad \text{with} \quad \psi = \frac{\Psi}{2\Omega \sin \phi} \quad (2.3)$$

where Ψ is the geopotential and Ω the Earth’s rotating rate. Furthermore, to study the temporal development of the geostrophic flow, the ageostrophic velocities are defined as the difference between the wind and the geostrophic wind:

$$u_a \equiv u - u_g, \quad v_a \equiv v - v_g, \quad w_a = w.$$

A further scale analysis then results in the primitive equations on a beta-plane for quasi-geostrophic flow:

$$\frac{Du_g}{Dt} - f_0 v_a - \beta y v_g = X \quad (2.4a)$$

$$\frac{Dv_g}{Dt} + f_0 u_a + \beta y u_g = Y \quad (2.4b)$$

$$\frac{\partial u_a}{\partial x} + \frac{\partial v_a}{\partial y} + \frac{1}{\rho} \frac{\partial}{\partial z} (\rho w_a) = 0 \quad (2.4c)$$

$$\frac{D\theta_e}{Dt} + w_a \frac{\partial \theta_0}{\partial z} = Q \quad (2.4d)$$

where

$$\frac{D}{Dt} = \frac{\partial}{\partial t} + u_g \frac{\partial}{\partial x} + v_g \frac{\partial}{\partial y}.$$

The terms X and Y refer to nonconservative mechanical forcings and Q is the diabatic heating, ρ is the density, θ_e is the difference of the potential temperature θ and the reference potential temperature $\theta_0(z)$, i.e., $\theta_e = \theta - \theta_0(z)$. A detailed derivation of the primitive equations on a beta-plane for quasi-geostrophic flow can be found for example in Andrews *et al.* (1987).

Chapter 2 Planetary waves and their general characteristics

This set of equations is a good approximation of middle atmosphere dynamics for studying PW effects but is still unhandy. By combining these four equations, a single useful equation is obtained – the quasi-geostrophic potential vorticity equation:

$$\frac{Dq}{Dt} = \frac{f_0}{\rho} \frac{\partial}{\partial z} \frac{\rho Q}{\partial \theta_0 / \partial z} + \frac{\partial Y}{\partial x} - \frac{\partial X}{\partial y} \quad (2.5)$$

where

$$q = f_0 + \beta y + \frac{\partial v_g}{\partial x} - \frac{\partial u_g}{\partial y} + \frac{f_0}{\rho} \frac{\partial}{\partial z} \left(\frac{\rho \theta_e}{\partial \theta_0 / \partial z} \right) \quad (2.6)$$

is the so-called potential vorticity. A detailed derivation of equation (2.5) from the primitive equations on a beta-plane for a quasi-geostrophic flow is presented in Appendix A based on *Andrews et al.* (1987).

Linear wave theory is then further applied for the consideration of PWs. Therefore, the disturbance ansatz, i.e., $b = \bar{b} + b'$, where $(\bar{\quad})$ denotes the zonal mean and $(\quad)'$ the deviation from it, is applied to equation (2.5), where

$$u_g = \bar{u}, \quad v_g = v', \quad q = \bar{q} + q' \quad \text{and} \quad \psi = \bar{\psi} + \psi'.$$

Thus, the linearized quasi-geostrophic potential vorticity equation is given by

$$\left(\frac{\partial}{\partial t} + \bar{u} \frac{\partial}{\partial x} \right) q' + v' \frac{\partial \bar{q}}{\partial y} = S' \quad (2.7)$$

where S' represents the disturbance of the nonconserving terms and where from equation (2.6) and $p = \rho RT$ follows:

$$q' = \frac{\partial^2 \psi'}{\partial x^2} + \frac{\partial^2 \psi'}{\partial y^2} + \frac{f^2}{p} \frac{\partial}{\partial z} \left(\frac{p}{N^2} \frac{\partial \psi'}{\partial z} \right) \quad \text{and} \quad (2.8)$$

$$\frac{\partial \bar{q}}{\partial y} = \beta - \frac{\partial^2 \bar{u}}{\partial y^2} - \frac{f^2}{p} \frac{\partial}{\partial z} \left(\frac{p}{N^2} \frac{\partial \psi'}{\partial z} \right). \quad (2.9)$$

The potential vorticity is a quantity which is proportional to the dot product of vorticity and stratification. Vorticity is mathematically defined as the rotation of the velocity field of the flow. Since PWs are considered on a plane (x, y) which is independent of the z component, the vorticity vector is always parallel to the z -axis and therefore can be viewed as a scalar field. Thus, the potential vorticity is a conserved quantity following the flow. Equation (2.7) becomes

$$\left(\frac{\partial}{\partial t} + \bar{u} \frac{\partial}{\partial x} \right) q' + v' \frac{\partial \bar{q}}{\partial y} = 0. \quad (2.10)$$

This equation is the starting point for every further consideration of the general characteristics of PWs.

2.1 Generation mechanism of PWs

The development of PWs is considered by the simple case of a homogeneous, incompressible fluid of uniform depth, i.e., a barotropic PW without vertical propagation. Thus, the potential vorticity is proportional to the absolute vorticity which is defined as

$$q := \xi + f \quad (2.11)$$

where ξ is the relative vorticity owing the rotation of the fluid and f the planetary vorticity owing the rotation of the fluid around the earth (e.g., *Holton and Alexander, 2000*). Here, the planetary vorticity is equal to the Coriolis parameter $f = 2\Omega \sin(\phi)$. It has its maximum at the pole, minimum at the equator and is negative in the southern hemisphere.

Figure 2.4(a) shows a schematic of the development of a barotropic PW in cartesian coordinates and Figure 2.4(b) in spherical coordinates in the northern hemisphere in four steps.

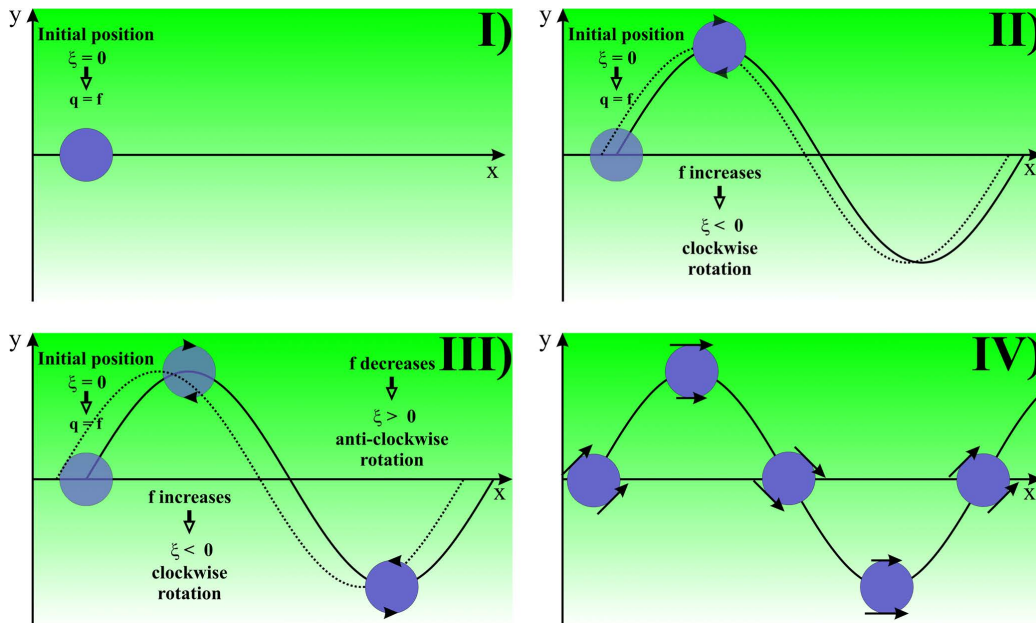


Figure 2.4(a) Schematic of the development of a barotropic PW in cartesian coordinates in four steps.

- I Consider a fluid parcel at a certain latitude ϕ_0 and assume initially that $\xi = 0$, i.e., no rotative motion of the fluid parcel around itself.
- II The fluid parcel is displaced northward, for example by the Rocky Mountains, see Figure 2.4(b). This means that the Coriolis parameter f increases and since equation (2.11) is conservative ($Dq/Dt = 0$), ξ has to decrease. Thus, the fluid parcel begins to rotate clockwise and therefore induces a southward movement.
- III This southward movement has enough energy to transport the fluid parcel south of its initial latitude ϕ_0 , the equilibrium. With this southward movement f decreases again and thus ξ increases and becomes positive south of its initial latitude.

Chapter 2 Planetary waves and their general characteristics

Therefore, the clockwise rotation of the fluid parcel weakens and reverses to an anti-clockwise rotation which induces a northward motion of the fluid parcel. In spherical coordinates a splitting occurs of the initially circular structure into a positive and negative part.

IV Thus, the fluid parcel oscillates around its initial latitude (equilibrium) and a PW is generated. Hence, the restoring force of a PW is the latitudinal variation of the Coriolis parameter.

PWs that are generated as described above can propagate vertically and horizontally only under certain conditions. These are discussed in the following sections.

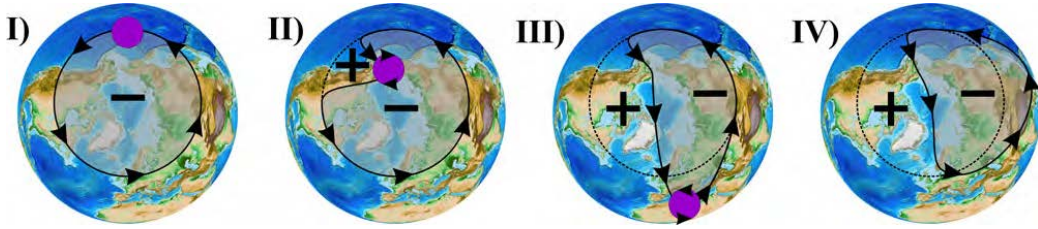


Figure 2.4(b) Schematic of the generation of a barotropic PW in the northern hemisphere in spherical coordinates in four steps.

2.2 Horizontal propagation

The starting point for the derivation of general characteristics of PWs is the linearized quasi-geostrophic potential vorticity equation (2.10) as mentioned above. Following *Holton and Alexander* (2000) for the horizontal propagation of a PW, it is assumed that the streamfunction ψ' and the zonal mean wind \bar{u} are given by

$$\psi' = e^{z/2H} e^{ik(x-ct)} \hat{\psi}(y, z) \quad \text{and} \quad \bar{u} = \bar{u}(y, z) \quad (2.12)$$

where $k = \frac{s}{a \cos(\phi)}$ is the zonal wavenumber in cartesian coordinates, c the phase velocity and H the scale height. Inserting this into equation (2.10) gives

$$\frac{\partial^2 \hat{\psi}}{\partial y^2} + \frac{f^2}{N^2} \frac{\partial^2 \hat{\psi}}{\partial z^2} + \underbrace{\left(\frac{\partial \bar{q}}{\partial y} - k^2 - \frac{f^2}{N^2 4H^2} \right)}_{=n^2} \hat{\psi} = 0 \quad (2.13)$$

where n is called the refractive index of a PW. The squared refractive index n^2 indicates regions in which a PW can horizontally propagate. PWs can horizontally propagate in regions where $n^2 > 0$ and avoid regions where $n^2 < 0$. Regions where $\bar{u} = c$ and thus $n^2 \rightarrow \infty$ are called critical layers.

Consider for example the stationary wave ($c = 0$). Thus, the squared refractive index n^2 is larger than zero if the zonal wind is eastward and not too strong. This is valid for the winter hemisphere at mid- and polar latitudes. Toward the equatorial zero wind line ($u = 0$) the refractive index increases rapidly and PWs can no longer propagate southward.

2.3 Charney-Drazin Criterion

The conditions under which vertical propagation of PWs is possible are described in the Charney-Drazin criterion (*Charney and Drazin, 1961*). Based on equation (2.13), we further assume that the zonal mean zonal wind is constant ($\bar{u} = \text{const}$) and the streamfunction is given by $\hat{\psi} = \psi_0 e^{imz} \sin(l y)$ where l is the meridional and m the vertical wavenumber. Thus, the term e^{imz} represents the vertical wave propagation. From this assumption it follows that $\partial \bar{q} / \partial y = \beta$ becomes constant. Inserting this simplification into (2.13) gives:

$$\left(\frac{\beta}{\bar{u} - c} - (k^2 + l^2) - \frac{f^2}{N^2} \left(m^2 + \frac{1}{4H^2} \right) \right) \hat{\psi} = 0. \quad (2.14)$$

Hence it follows

$$\bar{u} - c = \frac{\beta}{k^2 + l^2 + \frac{f^2}{N^2} \left(m^2 + \frac{1}{4H^2} \right)}. \quad (2.15)$$

For the vertical propagation $0 < m^2 < \infty$ follows

$$0 < \bar{u} - c < U_{\text{crit}} \equiv \frac{\beta}{k^2 + l^2 + \frac{f^2}{N^2 4H^2}}. \quad (2.16)$$

Equation (2.16) is called the Charney-Drazin criterion which implies that PWs can only propagate upward in eastward winds that are not too strong. The critical speed limit U_{crit} depends on the zonal and meridional wavenumber and decreases with increasing wavenumber and thus narrowing the window for the zonal wind in which a PW can propagate upward.

To illustrate the Charney-Drazin criterion, Figure 2.5 shows at the top the seasonal variation of the zonal wind at Andenes (69°N, 16°E) for the year 2009 from assimilated model (MERRA²) data (20 – 72 km) and MF radar³ data (74 – 96 km). At the bottom, the seasonal variation of upward propagation ability of the stationary wave 1 is shown, i.e., the application of the Charney-Drazin criterion to the seasonal variation of the zonal wind. Orange colored regions represent the ability and white/blue regions the disability of PWs to propagate upward. White regions mark areas where westward winds dominate and blue regions where the eastward wind is too strong.

During summer, westward winds dominate and hence an upward propagation of PWs from the troposphere into the mesosphere is not possible. Only at the mesopause where the wind reverses, upward propagation of PWs is again possible. The winter months are dominated by eastward winds and thus allow PWs to propagate upward from the troposphere into the mesosphere. One exception can be found at the end of January where the zonal wind reverses between the troposphere and mesosphere to westward wind for a few days. This phenomenon is called a Sudden Stratospheric Warming and is one of the main topics of this thesis. It is closer investigated in chapter 6.

²MERRA is an assimilated model from NASA and is described in chapter 3.

³The Mid Frequency (MF) radar is described in chapter 3.

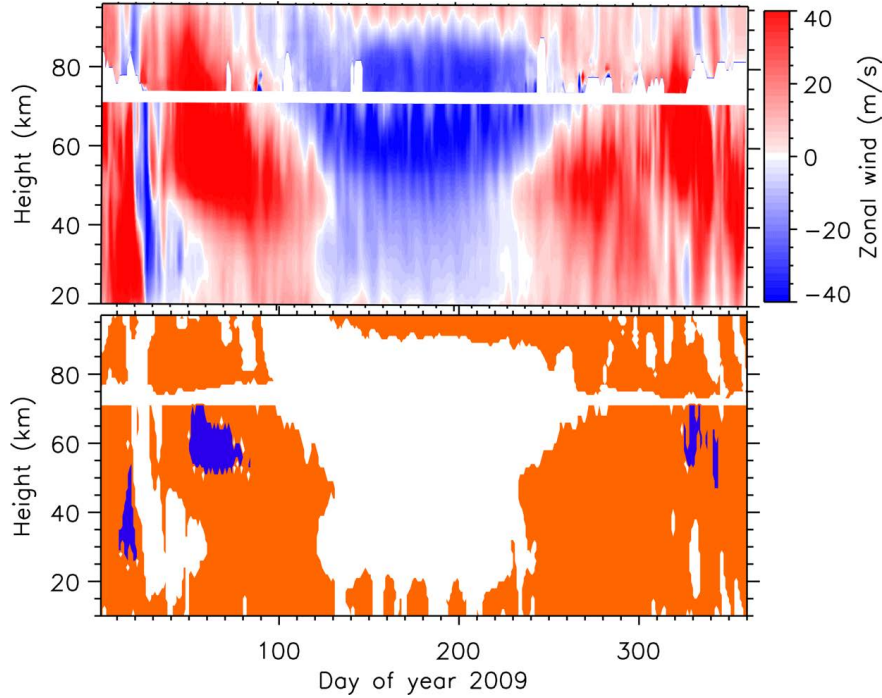


Figure 2.5 **Top:** Seasonal variation of the zonal wind at Andenes in 2009. **Bottom:** Seasonal variation of the vertical propagation ability of the stationary wave 1 ($c = 0, s = 1$) at Andenes (69°N) in 2009, i.e., application of the Charney-Drazin criterion to the seasonal variation of the zonal wind. Orange colored regions mark the possibility for upward propagation of the stationary wave 1. White/blue regions mark the disability of the PW to propagate upward due to westward/too strong eastward winds.

Applying the Charney-Drazin criterion to other stationary and transient waves gives in general a similar picture as in Figure 2.5. During summer it is hard for PWs to propagate upward from the troposphere into the mesosphere while the dominating eastward winds during winter allow a vertical propagation of PWs from the troposphere into the mesosphere.

2.4 Dispersion relation

The dispersion relation of a wave describes the property of a wave to travel in a certain medium and connects the frequency, wavenumber and phase velocity of a wave with each other. Following *Andrews et al.* (1987), the dispersion relation follows directly from equation (2.15). The resulting phase velocity c is then given by

$$c = \frac{\omega}{k} = \bar{u} - \frac{\beta}{\underbrace{k^2 + l^2 + \left(\frac{f_0}{N}\right)^2 \left(m^2 + \frac{1}{4H^2}\right)}_{\geq 0}}. \quad (2.17)$$

The last term on the right hand side of this equation is always positive. Thus, the zonal phase propagation of a PW is always westward relative to the mean flow. Thereby, PWs differ from other waves like gravity waves which are able to propagate westward and eastward relative to the mean flow.

2.5 Wave-mean flow interaction

In general, PWs transport heat and momentum flux from the equator to the pole. To understand how coupling processes arise, it is important to know under which circumstances PWs interact with the mean flow, i.e., when they deposit their energy to the mean flow. Again, *Charney and Drazin* (1961) formulated conditions under which no wave-mean flow interaction takes place. This is known as the Charney-Drazin theorem or the non-acceleration theorem. The Charney-Drazin theorem declares that there is no wave-mean flow interaction if the wave

- i. is steady,
- ii. non-dissipative (no critical layer in the zonal wind) and
- iii. has small amplitudes.

Thus, PWs with these characteristics have no influence on the mean flow and can not be responsible for vertical coupling processes like SSWs. This changes if there is a critical layer or the waves have extraordinary large amplitudes. A discussion of the applicability of the Charney-Drazin theorem to SSW conditions can be found in chapter 5. A detailed derivation of the Charney-Drazin theorem is beyond the scope of this thesis but can be found in *Charney and Drazin* (1961) or for example in *Andrews et al.* (1987).

On the basis of the PW theory described in this chapter also the propagation of the stationary PW flux can be considered. This flux can be calculated by means of the two dimensional Eliassen-Palm flux or the more general and three dimensional Plumb flux. The Plumb flux is used in this thesis for the study of the stationary wave flux during SSWs. A description of the Plumb flux is given in section 3.4.4 and a derivation is found in Appendix B.

Summarizing the general characteristics of PWs, the restoring force of PWs is the latitudinal variation of the Coriolis force. They can only propagate horizontally and vertically in eastward winds that are not too strong (Charney-Drazin criterion) and propagate only westward relative to the mean flow. PWs which are steady, conservative and have a small amplitude do not interact with the mean flow (Charney-Drazin theorem).

To investigate characteristics of PWs like period, amplitude, wavenumber and propagation direction during vertical coupling processes, a combination of high-resolution local radar measurements at different locations, global satellite observations and assimilated model data are used. The following chapter 3 gives an overview of the instruments and models used in this thesis as well as of the data interpretation methods.

Chapter 3 Instruments, models and data interpretation methods

To study the characteristics of PWs during coupling processes in the middle atmosphere, three different types of data sets are analyzed: high-resolution local radar measurements, global satellite observations and global assimilated model data. By combining high-resolution radar measurements with global satellite observations, the period and wavenumber as well as the temporal development of a PW can be analyzed. With the help of the assimilated model data the radar gap in the stratosphere is filled and the 3-dimensional Plumb flux, characterizing the impact of stationary PWs on the background atmosphere, can be calculated.

In the following the characteristics of the here used radar and satellite instruments as well as of the assimilated models are described and data interpretation methods are presented.

3.1 Radar

Temporal and vertical high-resolution continuous wind measurements are obtained in the mesosphere from radar observations. Therefore, two different radar systems are used in this study: the Meteor Radar (MR) and the Mid Frequency (MF) radar. The characteristics of these radar systems as well as the wind calculation methods are described shortly in the following.

3.1.1 Meteor radar

When a meteor enters the atmosphere it is leaving behind a trail of ionized gas between 75 and 105 km at which radio waves of a MR can be specular reflected. The All-Sky Interferometry MR (SKiYMET) used in this study consists of one transmitting antenna and 5 receiving antennas which are arranged in an asymmetric cross with distances of 2 and 2.5 wavelengths of the emitted radio wave on the short and long axis, as presented in Figure 3.1. This asymmetry enables one to determine an almost unambiguous meteor position using interferometry. For the estimation of the wind field the so-called Doppler method is used. Therefore, the radial drift of the underdense meteor trail, due to the atmospheric neutral winds, is measured by observing its Doppler shift. Due to the broad beam of the MR, the radial velocity of a sufficient number of meteor echoes is derived in different directions of the upper atmosphere and therefore enables to fit an average wind field in the MLT region. A detailed description of the SKiYMET and of

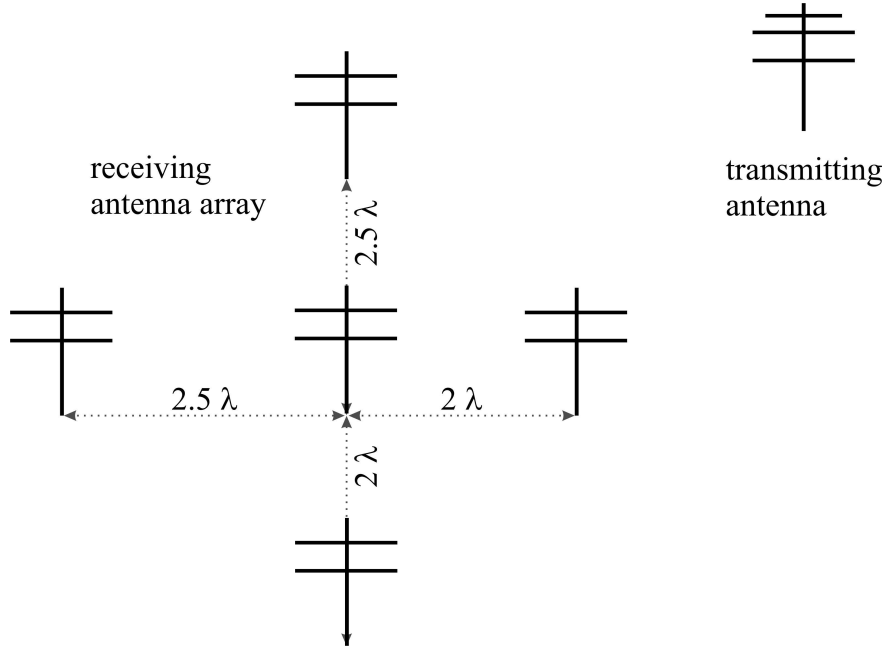


Figure 3.1 Scheme of the antenna array for a meteor radar like in Andenes.

the wind measurements can be found in *Hocking et al.* (2001).

In this thesis, meteor wind measurements from four different locations are used: Tavi-stock (43°N, 81°W), named CMOR¹, Juliusruh (54°N, 13°E), Andenes (69°N, 16°E) and Eureka (80°N, 86°W). CMOR operates at three frequencies (17.45, 29.85 and 38.15 MHz) while the other three MRs operate at 32.55 MHz. A summary of the specific characteristics of the four MR systems is given in Table C.1 in Appendix C.

3.1.2 MF radar

A radio wave emitted from a MF radar is partially reflected or scattered at a boundary between media of different refractive indices of ionized irregularities between 60 and 110 km. A MF radar consists basically of a transmitting and a separate (spaced) receiving antenna array which is important for wind measurements. Figure 3.2 shows the structure of MF radars used in this study at Saskatoon (52°N, 107°W), Juliusruh (54°N, 13°E) and Andenes (69°N, 16°E) which operate at a frequency of 2.22, 3.17 and 1.98 MHz respectively. A detailed description of the characteristics of each MF radar can be found in *Meek and Manson* (1987), *Keuer et al.* (2007) and *Singer et al.* (1997) and a summary of the characteristics in Table C.2 in Appendix C.

For the estimation of the horizontal wind field the Full Correlation Analysis (FCA) is used. The underlying assumption of the FCA method is the Taylor hypothesis which says that the refractive index irregularities are carried with the wind. The spaced receiving antennas receive the same signal at different times where the time delay is

¹CMOR = Canadian Meteor Orbit Radar

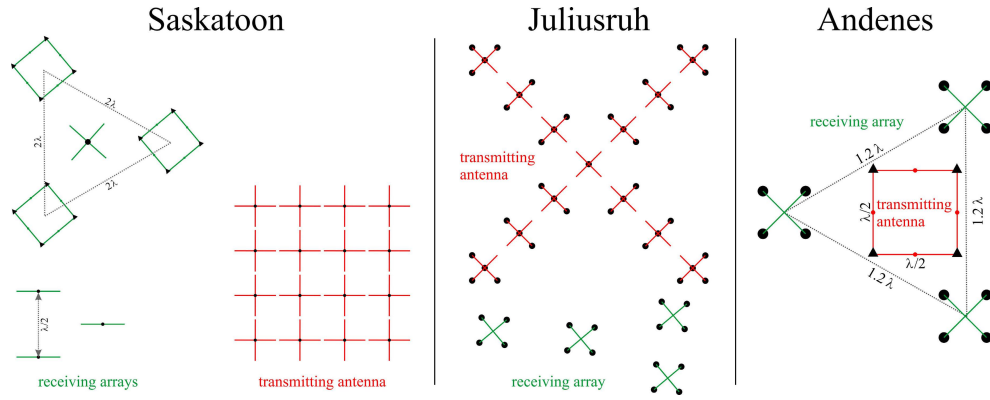


Figure 3.2 Schemes of the antenna arrays for the MF radars at Saskatoon, Juliusruh and Andenes.

calculated by cross correlation of the signals. From this the horizontal wind velocities can be obtained. A detailed description of the FCA method is given in *Briggs* (1984).

A global view of all MR and MF radars used in this thesis is shown in Figure 3.3. The figure shows a map of a part of the northern hemisphere in which the MR locations are marked with a black point and the MF radar locations with a red point.



Figure 3.3 Map of all radar stations used in this thesis split into MR and MF radar stations.

3.2 Microwave Limb Sounder onboard the Aura satellite

In the following, the Aura satellite as well as its instrument, the Microwave Limb Sounder (MLS), will be compactly described. For more information on the Aura satellite see *Schoeberl et al.* (2006) and on MLS see *Waters et al.* (2006). Aura is a National Aeronautics and Space Administration (NASA) satellite which was launched on July 15, 2004 to provide information of the Earth’s middle atmosphere as a part of the Earth Observing System (EOS) programm. It was launched into a sun-synchronous polar orbit at 705 km altitude with 98° inclination. Aura is part of the Afternoon

3.2 Microwave Limb Sounder onboard the Aura satellite

Train, short "A-Train", an extended instrument package focusing on climate change, named after its equator crossing time which is within several minutes of 1:30 pm local time. More detailed information about the A-Train can be found in *NASA* (2003). Aura itself has 4 instruments (see Figure 3.4): the High Resolution Dynamics Limb Sounder (HIRDLS), the here used Microwave Limb Sounder (MLS), the Ozone Monitoring Instrument (OMI) and the Tropospheric Emission Spectrometer (TES). The frontal position of MLS on Aura (see Figure 3.4) and the therefore forward looking direction of MLS allows a vertical scan of the limb in the orbital plane (see Figure 3.5). Thus, MLS has a coverage between 82°S and 82°N, i.e., nearly from pole to pole. Nevertheless, the actual temporal resolution at one location is one day. Observations of MLS on the ascending (north going) and descending (south going) side of the orbit have approximately the same local solar time.

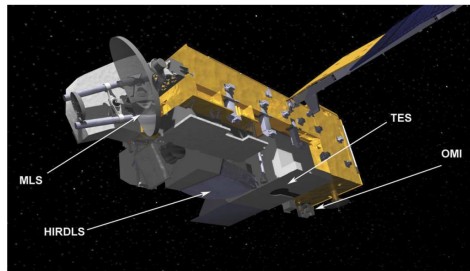


Figure 3.4 Model of the Aura satellite showing the location of the four instruments HIRDLS, MLS, OMI and TES, taken from *Waters et al.* (2006).

MLS itself contains five radiometers with different frequencies each useful for the measurement of thermal emission of special constituents. For example, the 118 GHz radiometer measures the thermal microwave emission from O_2 molecules to provide temperature and geopotential height (GPH) data which are used in this thesis. MLS scans the limb from the ground upward 240 times per orbit with ~ 14 orbits per day. This gives an along track separation of 165 km or 24.7 s between adjacent limb scans. After each scan all radiometers are calibrated by mirror rotating to the view of cold space and to the on-board ambient temperature THz black body calibration target. Thus, each limb scan inclusive calibration needs ~ 25 s.

The MLS raw data go through three data processing levels which are described in detail in *Livesey et al.* (2006). The retrieval algorithm gives beside the estimated atmospheric state also information about data quality. Temperature and GPH are coupled through the assumed hydrostatic balance. Thus, their characteristics are very similar. The scientific useful height range of both products is 316 hPa to 0.001 hPa (approximately 8 – 97 km) with a vertical resolution of 5.6 km at 316 hPa, 5.2 km at 100 hPa, 3.5 km at 31.6 hPa, 4.3 km at 10 hPa, 6.5 km at 3.16 hPa and up to 14 km at 0.01 hPa. Comparison of MLS measurements with assimilated model data and pre-validated satellite observations show an observed bias of -2 to 2 K in the troposphere and stratosphere and a cold bias of $-4 \dots -9$ K in the mesosphere for temperature measurements. The GPH product has an observed bias of 50 m to 150 m

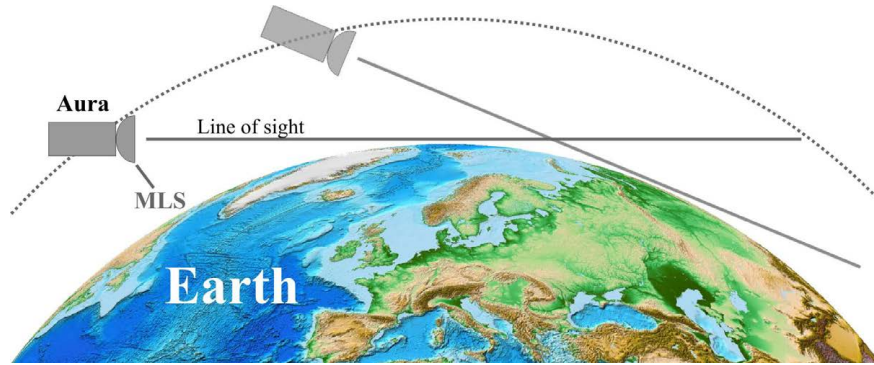


Figure 3.5 Line of sight of the MLS instrument on Aura

in the troposphere and stratosphere and up to -450 m at 0.001 hPa. More information about the validation of MLS temperature and GPH products can be found in *Schwartz et al.* (2008) and about the products in general in *Livesey et al.* (2007).

3.3 Model data

In this thesis also assimilated model data are used to fill the radar gap in the stratosphere, to consider latitudinal variations of the zonal wind and to estimate the stationary wave flux (Plumb flux). Assimilated models or reanalysis integrate a variety of observations with numerical models and are therefore able to provide a wide selection of atmospheric variables with observational influence that are not easy to observe with such a spatial and temporal resolution. In the following an overview is given of the three assimilated models used in this thesis.

3.3.1 ECMWF

The European Centre for Medium-Range Weather Forecasts (ECMWF) has a multiple set of products. For this study the reanalysis ERA-Interim is used which contains data from 1979 to present. The underlying model of ERA-Interim is the ECMWF Integrated Forecast System (IFS) which incorporates an atmospheric general circulation model, an ocean wave model and a land surface model. For the data assimilation the majority of observation comes from satellites (e.g., ozone, brightness temperature, total precipitable water, ...) but also from ships, drifting buoys and land stations (e.g., surface pressure, 2 m relative humidity, 10 m winds) and from radiosondes, pilot balloons, aircrafts, dropsondes and wind profilers (e.g., upper-air temperature, wind and upper specific humidity). The observations are combined with prior information from the forecast model IFS to estimate the evolving state of the global atmosphere. ERA-Interim has a temporal resolution of 6 hours and a horizontal resolution of 1° in the longitude and latitude. ERA-Interim includes 21 pressure levels between 1000 hPa and 1 hPa (0 – 48 km). For a detailed description of ERA-Interim see *Dee et al.* (2011) and for a description of the ERA-Interim product archive see *Berrisford et al.* (2009).

3.3.2 MERRA

MERRA is the acronym for Modern-Era Retrospective Analysis for Research and Applications. The underlying model of MERRA is the GEOS-5 Atmospheric General Circulation Model (AGCM) from the Global Modeling and Assimilation Office (GMAO) which is part of the NASA. For the data assimilation a variety of observational systems and observed variables is used: radiosondes, wind profiles, dropsondes, aircraft reports, diverse satellite observations of atmospheric parameters, buoys, ships, surface land observations and rain rate. A detailed list of all observational data sources used in MERRA can be found under <http://gmao.gsfc.nasa.gov/merra>. With these observations MERRA is able to cover a time period from 1979 to present and started its production in March 2008. Similar to ECMWF, MERRA is available in different products. The version used here has a horizontal resolution of $1/2^\circ$ in the latitude and $2/3^\circ$ in the longitude and has a temporal resolution of 6 hours with data provided at 0, 6, 12 and 18 UTC. In the vertical, there are 72 model and pressure levels from 985 hPa to 0.01 hPa (0.1 – 75 km) with a variable vertical resolution between 100 m in the troposphere and up to 4 km in the lower mesosphere. The advantage of MERRA compared to ECMWF is the vertical range up to the lower mesosphere while ECMWF has values only up to the upper stratosphere (48 km). Due to the later availability of MERRA, ECMWF was used in the earlier studies of this thesis.

MERRA shows a good agreement with ECMWF (e.g., *Rienecker et al.*, 2011) and MLS (e.g., *Yoo et al.*, 2013). For a detailed description of MERRA see *Rienecker et al.* (2011) and for an overview of MERRA products see *Lucchesi* (2012).

3.3.3 CMAM20

CMAM20 is an assimilated version of the Canadian Middle Atmosphere Model (CMAM) which is nudged to reanalysis data below 1 hPa between 1991 and 2011, i.e., 20 years of data. CMAM itself is a chemistry-climate model which extends from the surface to ~ 100 km and is described in detail in *de Grandpré et al.* (2000), *Jonsson et al.* (2004) and *Scinocca et al.* (2008). The horizontal winds and temperatures of CMAM20 are nudged to the horizontal winds and temperatures of ERA-Interim below 1 hPa. However, it is a free-running model above 1 hPa. CMAM20 has a horizontal resolution of 3.75° in latitude and longitude and a temporal resolution of 6 hours. CMAM20 consists of 71 pressure levels between 1000 hPa and 0.008 hPa with a vertical resolution of several tens of meters in the lower troposphere and 2.5 km in the mesosphere. The official early release of the CMAM20 model is available since December 2012.

For the study of a vertical coupling process during the fall transition, called “Hiccup”, a pre-version of the CMAM20 is used with data between 1989 and 2009. This study developed from a collaboration with Theodore Shepherd at the University of Toronto and is presented in chapter 7. The pre-version of the CMAM20 differs from the above described official version only in lower temporal resolution which is 11 hours.

The above described instruments and models have different height ranges and temporal availabilities which are shown in Figure 3.6. Winds in the mesosphere are predom-

inantly shown from MF radar observations in this thesis. Corresponding data cover lower altitudes than MR data and thus providing a better view on the mesospheric wind behavior. However, above 82 km the wave analysis is made using MR winds since it is well known that MF radar winds have too low bias (e.g., *Jacobi et al.*, 2009).

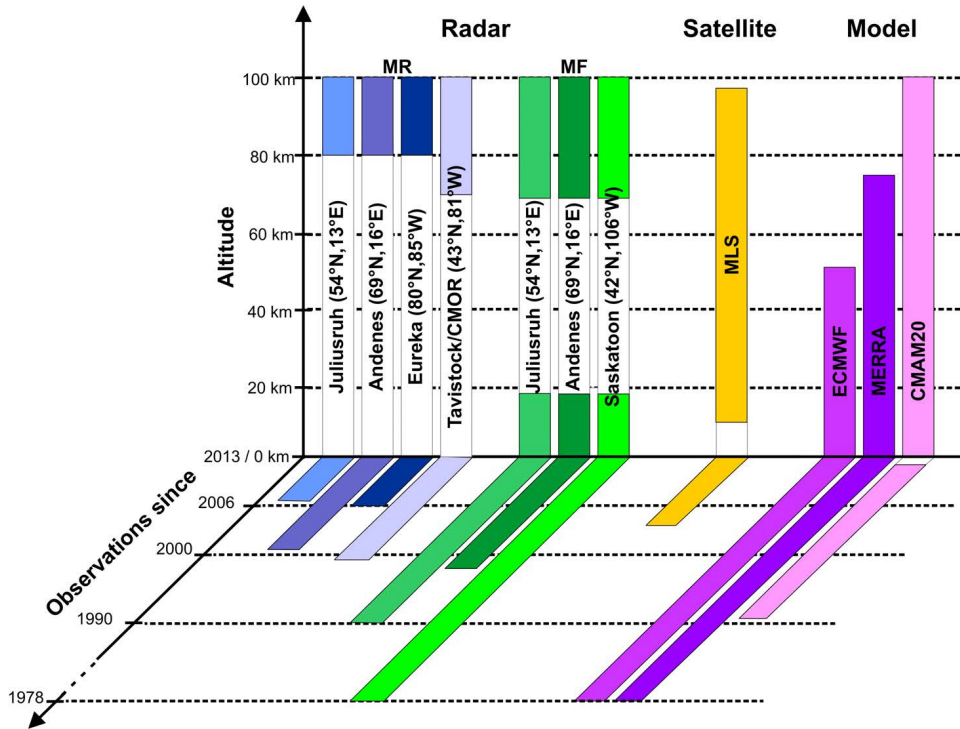


Figure 3.6 Overview of the height range and operation times of all instruments and models used in this thesis.

In general, composite analysis, as conducted in chapters 6 and 7, need long time series for stable results. In chapter 6 these analyses are conducted and compared with different instruments and models. Therefore, the interpretation of these analyses should include a consideration of the different length of time series of the different instrument as well as the different height ranges.

The assimilated model data differ in their height range and temporal availability. As mentioned before the advantage of MERRA compared to ECMWF is the extended height range of MERRA up to 75 km. CMAM20 covers an even larger altitude range than MERRA and is hence used for the study of the Hiccup during the fall transition (see chapter 7). While it would have been interesting to use CMAM20 data also for other studies in this thesis, we note that this was only possible for the Hiccup-study which was jointly conducted with one of the CMAM-PIs, i.e., Prof. Theodore G. Shepherd.

3.4 Data interpretation methods

For the study of the characteristics of PWs a combination of high-resolution radar measurements and global satellite observations is used. The periods and temporal development of PWs are investigated first by temporal and altitudinal high-resolution radar measurements with the Wavelet analysis. Afterwards, with the help of the spectral analysis of global space-time series the wavenumber and propagation direction of a PW is estimated. To study the stationary wave flux, the so-called Plumb flux is calculated from global assimilated model data. These methods as well as the estimation of the prevailing wind, estimated from radar winds, are described in the following.

3.4.1 Estimation of the prevailing wind

The mesospheric wind field is dominated by strong thermal tidal activity. Thus, to study the prevailing wind, the terdiurnal, semidiurnal and diurnal tide has to be removed from the original estimated wind. This can be done by a least squares fit of hourly mean winds for a 4-day interval shifted by one day. The basic function describing these tidal components is given by

$$y_i = U + \sum_{j=1}^3 \left(A_j \cos \frac{2\pi}{T_j} t_i + B_j \sin \frac{2\pi}{T_j} t_i \right) \quad (3.1)$$

with the periods $T_j = (8 \text{ h}, 12 \text{ h}, 24 \text{ h})$ and where U , A_j and B_j are the coefficients to be fitted and y_i the wind value at the time t_i . The coefficient U represents the prevailing (background) wind where the tidal activity is subtracted. Note, that for wave analyses the tides are not removed.

3.4.2 Wavelet analysis

A Wavelet analysis is similar to a Fourier analysis – a convolution of the time series with a wavelike basic function. The big advantage of a Wavelet analysis compared to a Fourier analysis is that beside the information of the included frequencies also a temporal development of them is given. The basic function of a Wavelet transform, the Wavelet function $\psi_{s,\tau}(t)$, is generated from the Mother-Wavelet $\psi(t)$ by dilation and translation

$$\psi_{s,\tau}(t) = \frac{1}{\sqrt{s}} \psi \left(\frac{t - \tau}{s} \right). \quad (3.2)$$

There are two conditions for a function to be a Wavelet: First it has to be localized in the time and frequency space and second it has to have a zero mean (e.g., *Farge, 1992*). For geophysical applications the Morlet-Wavelet $\psi_m(t) = \pi^{-1/4} \exp(iw_0 t) \exp(-t^2/2)$, a plane wave modulated by a Gaussian, is used in general. The nondimensional frequency w_0 is chosen to be $w_0 = 6$ and thus satisfying the above mentioned two conditions of a Wavelet. For a time series x_n with $n = 0, \dots, N - 1$ and equal time spacing δt the Wavelet transform is given by

$$W_n(s) = \sum_{i=0}^{N-1} x_i \psi^* \left(\frac{(i - n)\delta t}{s} \right) \frac{1}{\sqrt{s}} \quad (3.3)$$

Chapter 3 Instruments, models and data interpretation methods

where $()^*$ denotes the complex conjugate. The convolution theorem indicates that $f * g = \mathfrak{F}^{-1}(\mathfrak{F}(f) \cdot \mathfrak{F}(g))$ where \mathfrak{F} denotes the Fourier transform. Applying this to the Wavelet transform gives

$$W_n(s) = \sum_{k=0}^{N-1} \hat{x}_i \hat{\psi}^*(sw_k) e^{(iw_k n \delta t)} \quad (3.4)$$

with

$$w_k = \begin{cases} \frac{2\pi k}{N\delta t} & \text{for } k \leq \frac{N}{2} \\ -\frac{2\pi k}{N\delta t} & \text{for } k > \frac{N}{2} \end{cases}. \quad (3.5)$$

With this, the Wavelet transform can be very efficiently calculated via FFT (Fast Fourier Transformation). Therefore, by varying the scale s and translation along the localized time index n one can construct a picture showing the amplitudes and their temporal development of the frequencies in the time series. To compare the Wavelet transform at each scale s with each other a normalization is necessary. Usually, this normalization is chosen to be $\sqrt{\delta t/s}$. The amplitude of the Wavelet transform can then be calculated by $|W_n(s)|\sqrt{\frac{\delta t}{s}}$.

In this study also the fluctuations in amplitude of a specific band of scales are investigated. The calculation of the scale-averaged Wavelet amplitude W_n^{avg} over the scales $s_{\text{avg}} = \{s_{m_1}, \dots, s_{m_k}\}$ is performed as

$$W_n^{\text{avg}} = \frac{1}{k} \sum_{j=1}^k \frac{|W_n(s_{m_j})|}{\sqrt{s_{m_j}}}. \quad (3.6)$$

The Wavelet transform is a two parametric function generated from an initially one dimensional function. Thus, it is not possible to get an arbitrary accurate resolution in frequency and time space of a Wavelet transform due to the uncertainty relation. Therefore, the interpretation of a Wavelet transform has to be done carefully.

The mathematical definition of a Wavelet transform includes an unbounded integral. In practice, data sets are finite and influence therefore the boundary area of the Wavelet transform, the so called cone of influence (COI), where edge effects become important. To avoid these effects in the time period that is investigated an extended time interval is chosen.

In this thesis the Wavelet transform is conducted using the software provided by *Torrence and Compo* (1998). For a detailed description of the mathematical background see *Daubechies* (1995) and for more information of the practical use of the Wavelet analysis see *Farge* (1992) and *Torrence and Compo* (1998).

3.4.3 Spectral analysis of space-time series

The spectral analysis of space-time series is a two dimensional least squares fitting technique originally invented and described in detail by *Wu et al.* (1995). The advantage of using a least squares method is that it can handle unevenly spaced samples, as it is

3.4 Data interpretation methods

the case with the MLS data set used here. The basic function is given by

$$y = A \cos(2\pi\{\omega t - s\lambda\}) + B \sin(2\pi\{\omega t - s\lambda\}) \quad (3.7)$$

where y is the value measured at the universal time (UT) t in days and at longitude λ normalized by 360° at a chosen frequency ω and wavenumber s . By varying the frequency and wavenumber the frequency/wavenumber spectrum of a wave is obtained. A negative wavenumber means westward propagation and a positive eastward propagation of the PW.

The two dimensional space-time analysis can be reduced to a single variable by making the transformation $\omega't' = \omega t + s\lambda$. Thus, there is no fundamental difference between the one and two dimensional fitting technique. The amplitude $R(\omega, s)$ and phase $\rho(\omega, s)$ of a wave with frequency ω and wavenumber s is calculated as

$$R(\omega, s) = \sqrt{A^2(\omega, s) + B^2(\omega, s)} \quad \text{and} \quad \rho(\omega, s) = \arctan(B/A). \quad (3.8)$$

Therefore, the two dimensional spectral analysis is a useful tool for obtaining the amplitude and phase of a wave if the periodicity is known. The periodicity is here estimated applying a Wavelet analysis (see subsection 3.4.2) to the radar measurements in the mesosphere. The combination of local radar measurements and global satellite observations allows us to determine the characteristics of a PW.

The spectral resolution of this analysis technique is given by

$$(\Delta\omega T)^2 + (\Delta s)^2 = a^2 \quad (3.9)$$

where T is the total sample length, $\Delta\omega$ the resolution in frequency, Δs the resolution in wavenumber and a a constant with values between 1 and 1.45 (see *Wu et al., 1995*). Thus, the resolution for the frequency can be improved by increasing the total sample length but not the wavenumber. To distinguish between a 10- and 9-day wave with the same wavenumber a data set of a total length of at least 90 days is needed, which is much longer than the duration of the wave event and therefore smooths the signal. The solution is to study not a single period but a period range with a sample length that is four times longer than the mean period of the investigated period range. This is a good compromise between resolution and signal smoothing. In this study, especially the 10- and 16-day waves are investigated. Thereby, the 10-day wave contains periods between 8 and 12 days and is analyzed with a sample length of 40 days while the 16-day wave contains periods between 12 and 20 days and is analyzed with a sample length of 70 days.

The interpretation of the frequency/wavenumber spectra has to be made carefully. Since the solution of equation (3.7) is not unique, aliasing effects may occur. Due to the irregular sampling of the MLS data set their magnitude is smaller than the magnitude of the original wave. Aliasing effects have to be considered especially during investigations of PWs with lower periods as it is discussed for the 2-day wave by *Tunbridge et al. (2011)*.

To test the aliasing effects of the here investigated 10- and 16-day wave, Figure 3.7 shows the period/wavenumber spectra of a synthetically generated 10-day wave (left) and 16-day wave (right) with wavenumber -1 (westward propagating) sampled like

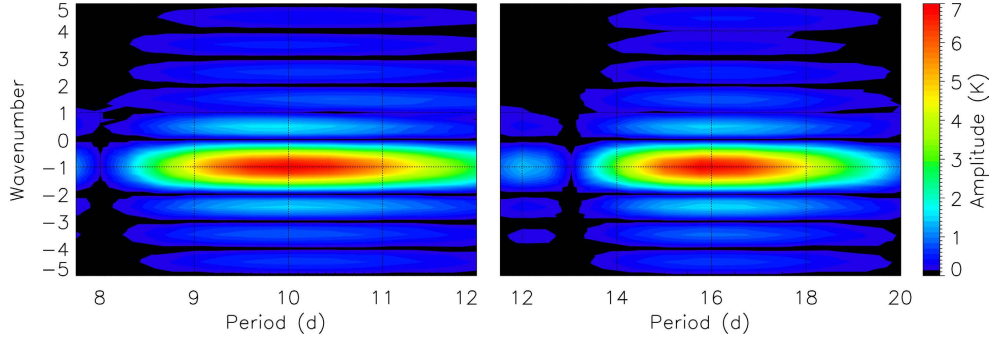


Figure 3.7 Aliased signal of a synthetic generated PW with a period of 10 days (left) and 16 days (right), each with a wavenumber -1 (westward propagating) sampled like MLS at 70°N .

the MLS data at 70°N . The amplitude of the aliased wave components is much smaller than that of the actual wave. These components have a similar period as the actual wave but differ in their wavenumbers. Hence aliasing effects can be easily distinguished from the original wave in these cases.

3.4.4 The three-dimensional Plumb flux

The three-dimensional Plumb flux is a generalization of the better known and two-dimensional Eliassen-Palm flux (EP flux). The Plumb flux is an indicator of the propagation of stationary wave activity and its zonal mean is consistent with the EP flux. The derivation of the Plumb flux can be found in Appendix B and is taken from *Plumb* (1985). The three-dimensional Plumb flux vector in spherical coordinates is defined as (see *Plumb*, 1985):

$$F_{\text{plumb}} = (F_\lambda, F_\phi, F_z) = p \cos(\phi) \begin{pmatrix} v'^2 - \frac{1}{2\Omega a \sin 2\phi} \frac{\partial(v'\Phi')}{\partial\lambda} \\ -u'v' + \frac{1}{2\Omega a \sin 2\phi} \frac{\partial(u'\Phi')}{\partial\lambda} \\ \frac{2\Omega \sin \phi}{J} \left[v'T' - \frac{1}{2\Omega a \sin 2\phi} \frac{\partial}{\partial\lambda} (T'\Phi') \right] \end{pmatrix} \quad (3.10)$$

$$\text{with } J = \frac{\partial \bar{T}}{\partial z} + \frac{\kappa \bar{T}}{H} \quad (\text{static stability}) \quad (3.11)$$

where F_λ , F_ϕ and F_z are the longitudinal, latitudinal and vertical components of the Plumb flux vector and where λ is the longitude, ϕ the latitude, z the altitude, u and v are the zonal and meridional wind components, Φ the geopotential, T the temperature, p the pressure divided by 1000 hPa, a the Earth's radius, H the scale height, Ω the Earth's angular velocity and $\kappa = \frac{R}{c_p} \approx 0.286$. A bar ($\bar{\quad}$) denotes the zonal mean and a prime ($'$) the deviation from it.

Note, that the interpretation of a single arrow (see e.g., Figure 6.12) should be made with caution since the Plumb flux is not a strictly local quantity due to the definition of the stationary wave field by the deviation from the zonal mean flow. However, the

3.4 Data interpretation methods

three-dimensional Plumb flux is a good diagnostic tool for the propagation of stationary wave flux. To present the Plumb flux in practice, one of the three dimensions has to be averaged or restricted to a certain range or area.

The combination of local radar measurements and global satellite observations and their corresponding analysis methods allows a study of the characteristics of PWs. From chapter 2 it is known that there is a seasonal difference in the vertical propagation ability of PWs due to the Charney-Drazin criterion. Before we start investigating PWs during vertical coupling processes, we first introduce the seasonal and year-to-year variability of PWs in the stratosphere and mesosphere at Andenes (69°N) in the following chapter.

Chapter 4 Seasonal and year-to-year variability of PW activity

Due to the Charney-Drazin criterion (see section 2.3) the ability of PWs to propagate upward from the troposphere into the stratosphere and mesosphere varies throughout the year. Thus, the PW activity varies with the season in the middle atmosphere. In this chapter the seasonal and year-to-year variability of transient and stationary PWs in the middle atmosphere is studied using local radar observations at Andenes as well as satellite and model data at 69°N.

4.1 Seasonal variability of PWs

To study the seasonal variability of PWs the year 2009 was representatively chosen. In section 2.3, Figure 2.5 (top) shows the seasonal variation of the zonal wind at Andenes from MERRA (20 – 70 km) and MF radar (74 – 96 km) for 2009. The summer months are dominated by westward winds up to the mesopause where the wind reverses to eastward winds. Contrary to the summer season, the winter months are dominated by eastward winds in the stratosphere and mesosphere. Hence, there is a wind reversal from eastward/westward to westward/eastward during spring/autumn. During winter especially the mesosphere is highly variable in time while the summer occurs very stable with only little variability. The short term wind reversal in the stratosphere and mesosphere from eastward to westward wind at the end of January is remarkable. This phenomenon is an effect of the later more closely investigated Sudden Stratospheric Warming (SSW).

This seasonal variation of the zonal wind is typical at mid and high latitudes and representative also for other years (e.g., *Andrews et al.*, 1987; *Hoffmann et al.*, 2002, 2010). Only the SSW induced wind reversal in the winter months varies with time and strength (e.g., *Hoffmann et al.*, 2002). SSWs can be roughly classified into minor and major ones (see e.g., *Labitzke and Naujokat*, 2000). In 2009 a major SSW occurred, i.e., the zonal mean zonal wind at 10 hPa reverses while during minor warmings the zonal wind only weakens but does not reverse.

From the Charney-Drazin criterion we know that the vertical propagation ability of PWs depends on the background wind and thus has also a seasonal variation. Figures 4.1 and 4.2 show the wavelet spectrum of the meridional wind at Andenes at 85 km derived from MR data for the four seasons in 2009: winter 2008/09 (December to February), spring (March to May), summer (June to August) and autumn (Septem-

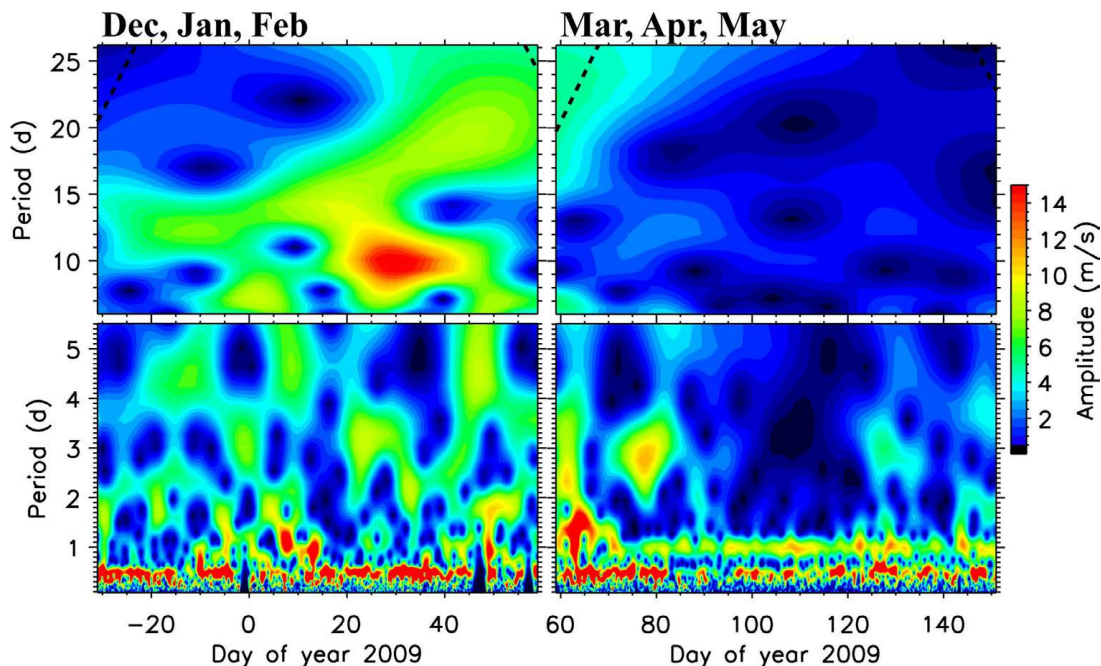


Figure 4.1 Wavelet spectrum of the winter 2008/09 from December to February (left) and of spring 2009 from March to May (right) at 85 km from Andenes MR.

ber to November). Note that with local radar measurements only transient PWs can be observed.

During winter 2008/09, where eastward winds dominate, an increased PW activity occurs in the mesosphere due to the ability of PWs to propagate upward from the troposphere into the mesosphere as shown in section 2.3. Here, a strong 10-day wave (period: 8 – 12 d) occurs at the end of January simultaneously with the wind reversal in the stratosphere and mesosphere (see Fig. 2.5) while a weaker 16-day wave (period: 12 – 20 d) occurs almost throughout the whole winter. These waves seem to be the most dominant ones during SSWs (e.g., *Jacobi et al.*, 1998b; *Palo et al.*, 2005; *Pancheva et al.*, 2008b; *Matthias et al.*, 2012a). In the period range between 2 and 8 days, there occur less intense PWs during winter compared to the dominating 10- and 16-day wave. There are also strong semidiurnal tides as well as the much weaker and less frequently occurring diurnal tides. The tidal behavior is beyond the scope of this thesis but is investigated for example in *Lindzen* (1967) or more recently by *Pancheva et al.* (2009a) and many more.

During spring the wave activity decreases with time simultaneously with the wind reversal from eastward to westward wind in the stratosphere and mesosphere. The two dominating PWs during winter vanish completely in spring. Only PWs with periods below 6 days occur occasionally during spring (e.g., *Jacobi et al.*, 1998b) but get weaker towards the summer. Similar to the winter period, there is a strong semidiurnal tidal activity as well as an increased diurnal tidal activity (e.g., *Jacobi et al.*, 1999).

The summer is the most quiet season referred to the PW activity due to the dominating westward wind in the stratosphere and lower mesosphere. Besides a strong diurnal

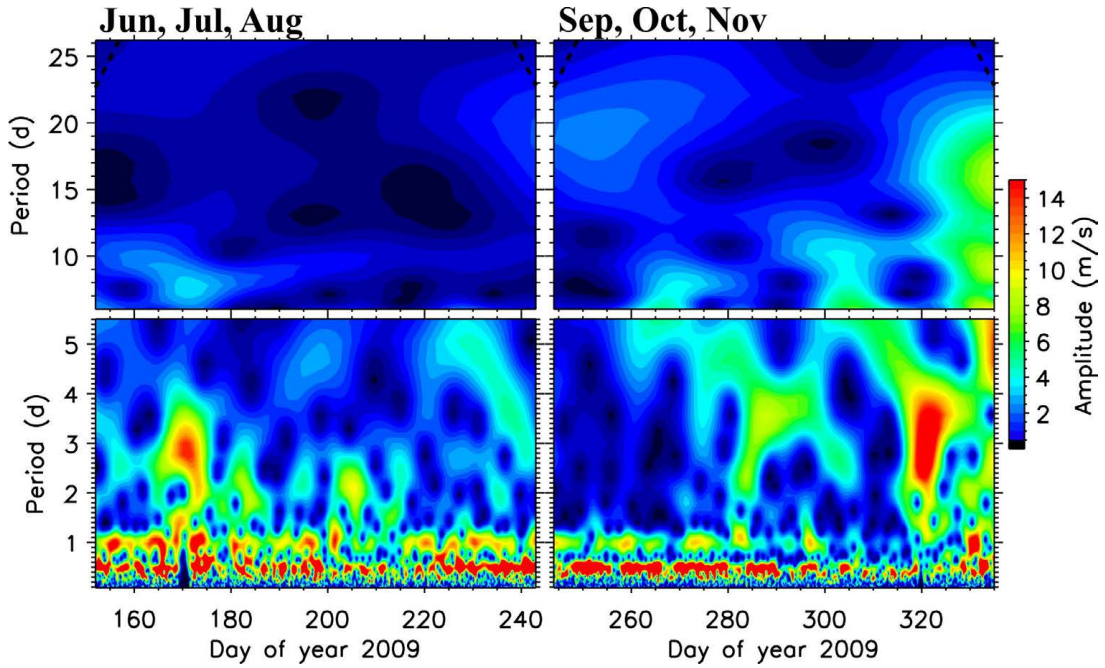


Figure 4.2 Wavelet spectrum of summer 2009 from June to August (left) and of autumn 2009 from September to November (right) at 85 km from Andenes MR.

and semidiurnal tidal activity, the only occurring PWs in the mesosphere are the 2- (period 1.6 – 3.3 d) and 5-day waves (e.g., *Jacobi et al., 1998b; Wu et al., 1994*).

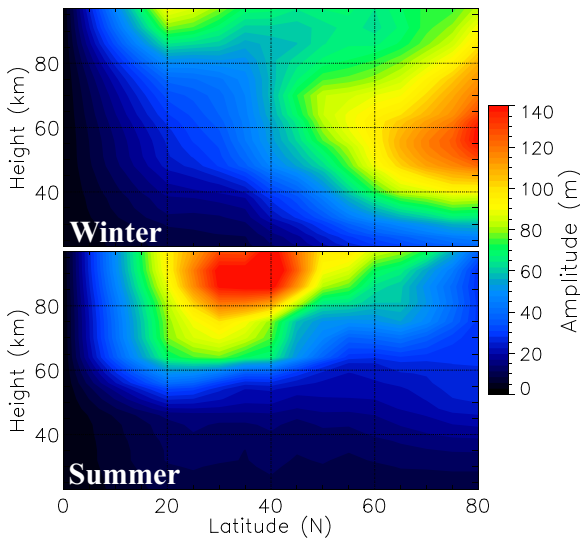


Figure 4.3 Averaged seasonal structure of the 2-day wave with wavenumbers between -5 and 5 from MLS GPH data for the winter 2008/09 (top) and summer 2009 (bottom).

there is a high wave activity of transient PWs

in winter in the mesosphere with a During autumn the wave activity increases with time simultaneously with the wind reversal from westward to eastward wind in the stratosphere and mesosphere. Similar to the spring period, only PWs with periods below 6 days occur and become stronger towards the winter. The semidiurnal tidal activity is again strong (e.g., *Jacobi et al., 1999*) while the diurnal tidal activity decreases with time.

This seasonal variation of the zonal wind and PW activity is typical for mid and high latitudes in the northern hemisphere (e.g., *Jacobi et al., 1998b; Chshyolkova et al., 2006; Hoffmann et al., 2010*).

Summarizing,

large variety of periods while the summer remains very quiet with only planetary 2- and 5-day waves in the mesosphere.

From the above presented results we have seen that one of the few PWs occurring during winter and summer in the mesosphere is the 2-day wave. Figure 4.3 shows the average seasonal latitudinal and altitudinal structure of 2-day waves with wavenumbers between -5 and 5 from MLS GPH data for the winter 2008/09 and summer 2009. Typical wavenumbers for a 2-day wave are between -2 and -4 in summer and winter (e.g., *Pancheva et al.*, 2004; *Limpasuvan et al.*, 2005). During winter there is a strong polar activity of the 2-day wave in the stratosphere and mesosphere decreasing with decreasing latitude. However, the 2-day wave in summer occurs only in the mesosphere, has its maximum at 30°N and decreases with increasing latitude.

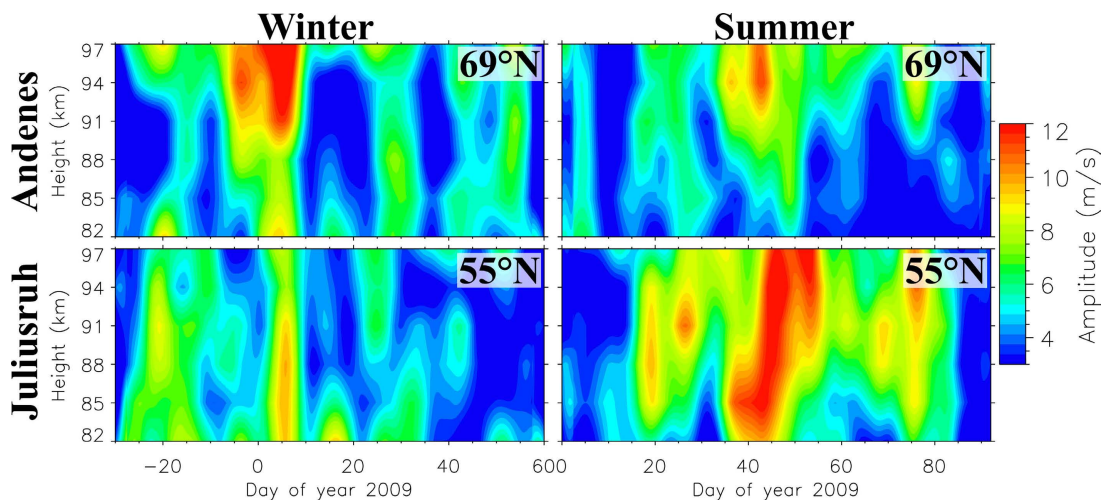


Figure 4.4 Amplitude of the 2-day wave at Andenes (top) and Juliusruh (bottom) for the winter 2008/09 (left) and summer 2009 (right) from meridional wind data from the corresponding MR.

The latitudinal differences of the mesospheric 2-day wave activity are also observable in MR wind measurements. Figure 4.4 shows the amplitude of the 2-day wave at Andenes and Juliusruh during winter 2008/09 and summer 2009 from meridional wind data of the corresponding MR. Similar to the global observation above, the 2-day wave has stronger amplitudes in winter at high latitudes than at mid latitudes and in summer vice versa.

These results together with the Charney-Drazin criterion allow the presumption that the 2-day wave in summer is not generated in the troposphere as during winter but in the mesosphere. Actually, the 2-day waves in the summer mesosphere are in-situ generated by baroclinic instabilities in the lower mesosphere (e.g., *Plumb*, 1983; *Offermann et al.*, 2011).

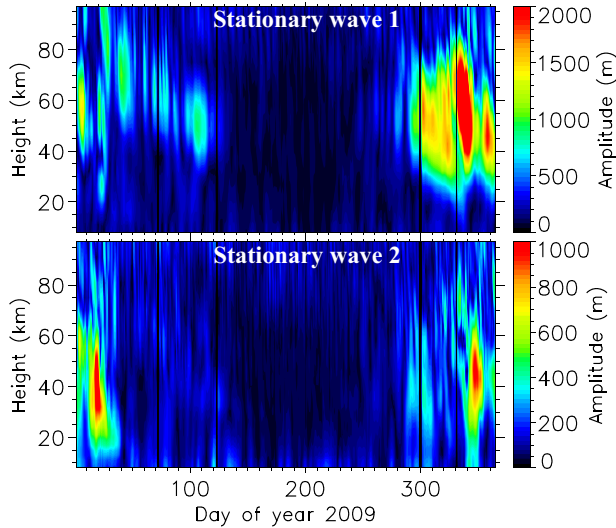


Figure 4.5 Seasonal variation of the amplitude of the stationary wave 1 (top) and stationary wave 2 (bottom) from MLS GPH data at $70^{\circ}\text{N} \pm 2.5^{\circ}$ for the year 2009.

much weaker than the stationary wave 1 and occurs also only during winter months. However, the occurrence rate of the stationary wave 2 is smaller than that of the stationary wave 1.

Even if these seasonal results of transient and stationary PWs are roughly representative for other years there are still considerable year-to-year variations in the PW activity. Therefore, the next section compares the PW activity of the three sequentially years 2009, 2010 and 2011.

4.2 Year-to-year variability of PWs

PWs vary in strength and occurrence time from year to year. This variation is exemplarily shown for the years 2009, 2010 and 2011 in this section. Figure 4.6 shows the mesospheric wave spectra for the years 2009, 2010 and 2011 similar to Figure 4.1. Comparisons of the winter months in 2009 and 2010 with 2011 show that there is a strong activity of a 10- and 16-day wave in 2009 and 2010 but only a weaker one in winter 2010/11. These differences in the PW activity affect the occurrence of a SSW as later discussed in chapter 6. Note, that during winter 2008/09 and 2009/10 a major SSW occurs while the winter 2010/11 remains very quiet with respect to SSWs. Noticeable is also that the PW activity with periods above 8 days extends more into spring in 2011 without a SSW than in 2009 and 2010 with a major SSW.

There are also differences in strength and occurrence in the PW activity with periods below 8 days during winter. They are more variable and their relation to SSWs are still not completely clear (see e.g., *Liu et al.*, 2004; *Gu et al.*, 2013).

The PWs with the largest amplitudes are stationary waves. Figure 4.5 shows the seasonal variation of the stationary wave 1 and 2 from MLS GPH data at 70°N . This figure shows a strong activity of the stationary wave 1 during winter months and almost no activity during summer which is again determined by the Charney-Drazin criterion (see section 2.3). The strong wintery activity is much weaker at the beginning than at the end of the year 2009 due to the major warming that took place at the end of January. In chapter 6 it is shown that the PW activity after a warming decreases rapidly due to the reversed zonal wind.

The stationary wave 2 is in general

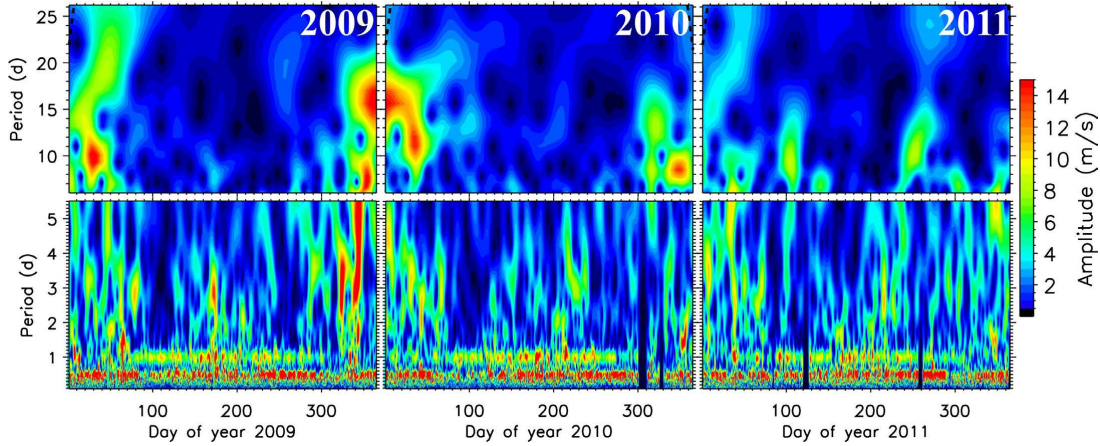


Figure 4.6 Seasonal variation of the wavelet spectrum of PWs of the meridional wind at 85 km from Andenes MR of 2009, 2010 and 2011. The black dashed lines on the edge mark the cone of influence. Waves underneath are trustworthy.

The activity of the 2-day wave during summer varies also from year to year. While the summer 2010 shows only low activity, there occurs a very strong 2-day wave in 2009. The seasonal variation of the tidal activity is roughly the same during all years but shows in detail distinctive differences due to the different wave-tide interactions (e.g., *Pancheva et al.*, 2002; *Pancheva*, 2006; *Hoffmann et al.*, 2007).

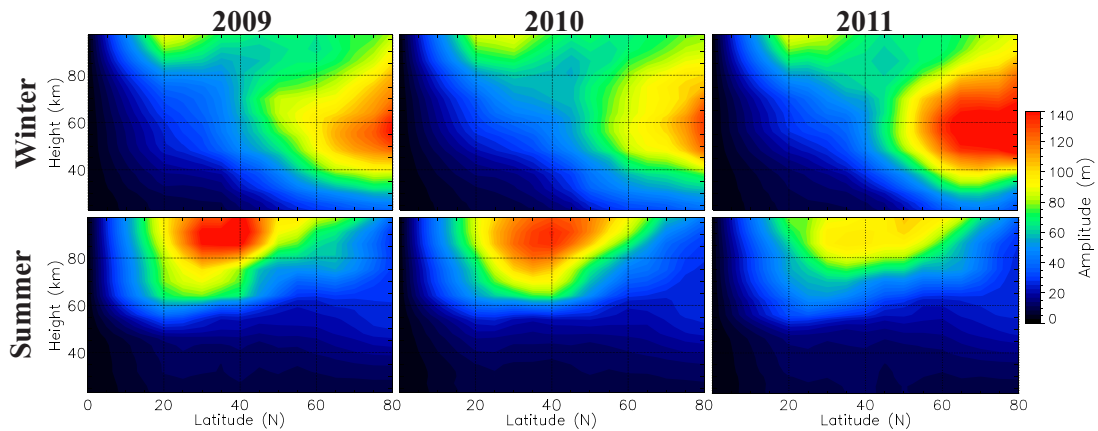


Figure 4.7 Averaged seasonal latitudinal structure of the 2-day wave with wavenumbers between -5 and 5 from MLS GPH data for the corresponding winter (top) and summer (bottom) for the years 2009, 2010 and 2011.

As before, the activity of the 2-day wave is considered in more detail in Figure 4.7 as a mean over the summer and winter months in 2009, 2010 and 2011. The strongest 2-day wave activity occurs during winter 2011 in the high latitudinal stratosphere and mesosphere and the weakest one in summer 2011 in the mesosphere. One reason for these differences is the nonlinear wave-wave interaction not only on a year-to-year basis

Chapter 4 Seasonal and year-to-year variability of PW activity

but also on a daily basis (e.g., *Jacobi et al.*, 1998a). The behavior of the 2-day wave during summer and winter and especially during SSWs is still not completely understood but is beyond the scope of this thesis.

The year-to-year variability of the stationary wave 1 and 2 from MLS GPH data is shown in Figure 4.8 for the sequential years 2009, 2010 and 2011. Again the stationary waves are active only during winter months but vary in strength and occurrence from year to year. At the beginning of 2009 and 2010, where a major SSW occurs in each year, the stationary wave 1 activity is temporally shorter and weaker than in 2011 where no significant warming occurs. However, the stationary wave 2 is strongest in January in 2009 compared to the other years due the vortex splitting during the 2009 SSW (e.g., *Manney et al.*, 2009). Hence, the activity of the stationary wave 1 and 2 depends on the occurrence of a SSW.

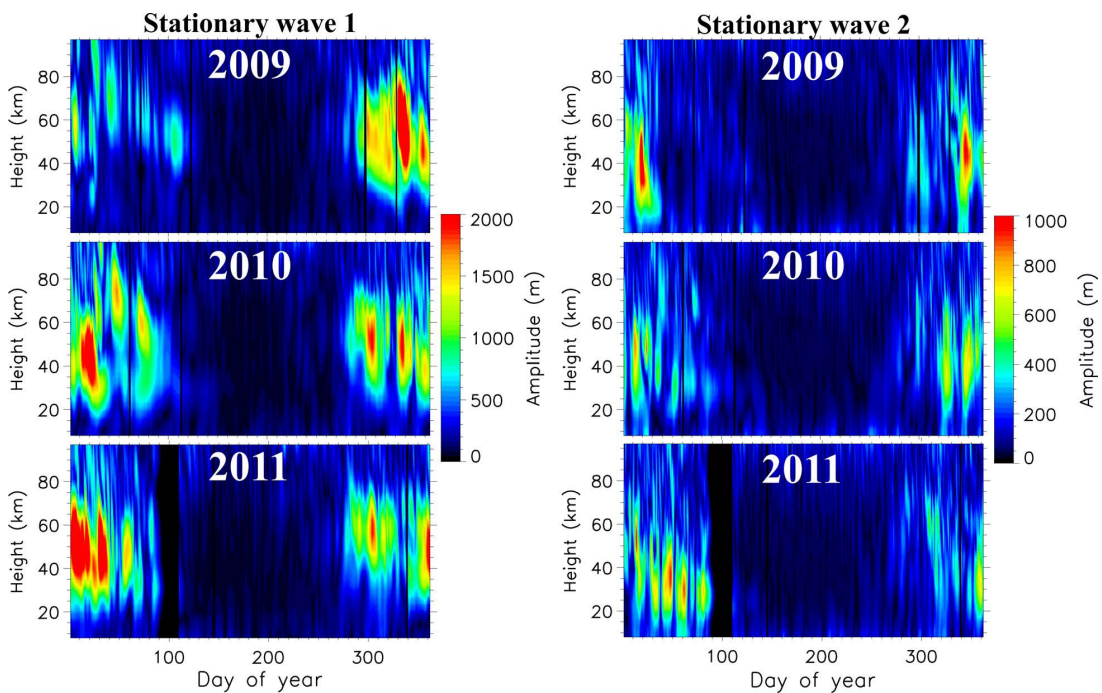


Figure 4.8 Seasonal variation of the amplitude of the stationary wave 1 (left) and stationary wave 2 (right) from MLS GPH data at 70°N for the years 2009, 2010 and 2011.

These results emphasize that the stationary and transient PW activity depends on SSW occurrence or is at least connected to SSWs during winter. The main topic of this thesis is the role of PWs during SSWs since this is the most prominent and impressive vertical coupling process observed in the middle atmosphere. Before we present a detailed study of PWs during major SSWs our current understanding of SSWs is shortly reviewed and our corresponding objectives are identified.

Chapter 5 SSWs: State of the art and objectives of this thesis

Sudden stratospheric warmings are the most impressive and prominent vertical coupling process in the middle atmosphere. They are caused by the interaction of upward propagating PWs with the mean flow (e.g., *Matsuno, 1971; Andrews et al., 1987*). The first comprehensive model of how a SSW is generated was presented by *Matsuno (1971)*. Since then a lot of theoretical and practical studies have improved this first model but there are still open questions.

This chapter presents the behavior of the middle atmosphere during SSWs by the example of the major warming in 2009 as well as an overview of the *Matsuno (1971)* theory on the generation of a SSW and its refinements during the last decades.

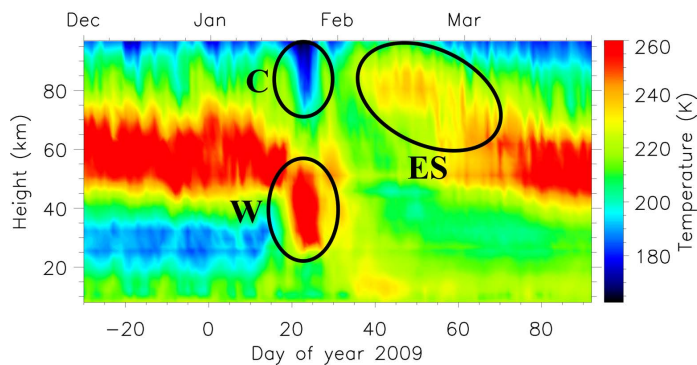


Figure 5.1 Seasonal variation of mean temperature around Andenes (0 – 30°E) in a 5° latitude band from December 1, 2008 until March 31, 2009 from MLS temperature data.

sphere. This event also shows an elevated stratopause (**ES**) up to 80 km after the warming which then moves down to normal stratopause heights with time. This effect is not observable during every SSW (e.g., *Manney et al., 2005; Limpasuvan et al., 2012*).

Besides this dramatic temperature change the zonal mean zonal wind weakens significantly or even reverses in the stratosphere and mesosphere during SSWs. Figure 5.2 shows the zonal wind from MERRA (10 – 72 km) and MR (82 – 94 km) data at Andenes as an example for the major warming in 2009. Here, the dominant eastward wind is reversed to a strong westward wind from the mesosphere to the stratosphere. This wind reversal is longer lasting in the stratosphere than in the mesosphere. After the SSW

The most noticeable property and name-giver of a SSW is the sudden increase of the stratospheric temperature as exemplarily shown in Figure 5.1 for the SSW of 2009. This figure shows the temporal development of the temperature derived from MLS at Andenes for winter 2008/09. During January 2009 a strong warming (**W**) of up to 80 K occurred in the stratosphere within a few days with a simultaneous cooling (**C**) in the meso-

the zonal wind reverses again to a dominant eastward wind (normal winter condition) but occurs stronger than before the warming in the mesosphere and upper stratosphere.

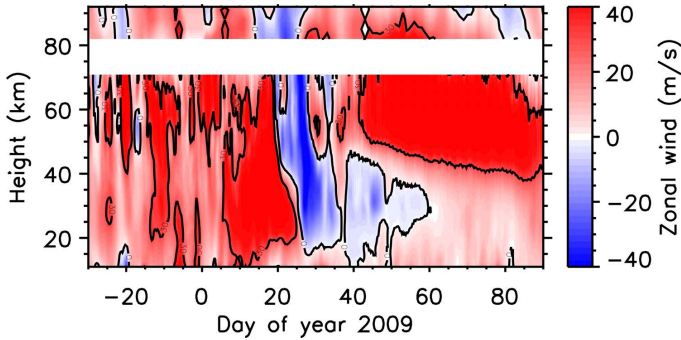


Figure 5.2 Zonal wind at Andenes for winter 2008/09 derived from MERRA (10 – 72 km) and MR (82 – 94 km) data.

There are different ways to classify SSWs. A classification with regard to their strength includes major and minor warmings (*Labitzke and Naujokat, 2000*). They differ in the significant reduction or even reversal of the zonal mean zonal wind. A detailed definition of major and minor warmings is given in chapter 6. Another classification scheme relies on the position of the polar

vortex (e.g., *Charlton and Polvani, 2007*). This scheme distinguishes between vortex displacements and splitting events. During vortex displacement events the polar vortex is displaced off the pole, during vortex splitting events it is split into two smaller vortices. The SSW of 2009 is a major warming accompanied by a vortex splitting (*Manney et al., 2009*).

As stated before, the reason for the generation of SSWs is the interaction of PWs with the mean flow. Especially the transient 10- and 16-day waves are related to the occurrence of a SSW (e.g., *Jacobi et al., 1998b; Pancheva et al., 2009c,b*). Therefore, Figure 5.3 shows the Wavelet spectrum of PWs with periods larger than six days. The data are derived from meridional MR winds at Andenes at 85 km for the winter 2008/09. While PWs are active throughout the winter a particularly strong 10-

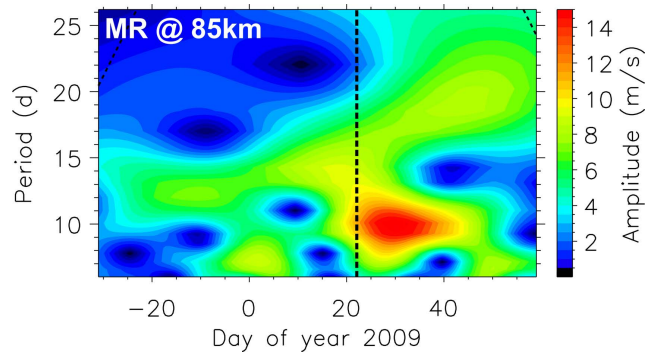


Figure 5.3 Wavelet spectrum of the meridional wind at Andenes at 85 km from MR for winter 2008/09. The dashed line marks the beginning of the wind reversal at 10 hPa during the SSW.

day wave occurs during the warming and a weaker 16-day wave occurs before and after the warming in the mesosphere. The propagation direction and wavenumber of these waves is then estimated by global temperature data from MLS. Figure 5.4 shows the period/wavenumber spectra of the 10- (left) and 16-day wave (right). Both waves have a wavenumber $-1/2$ which is evidence for a superposition of an oscillation and a westward propagating PW 1 (*Matthias et al., 2012a*). Note that this interpretation is supported by arguments presented in *Pancheva et al. (2009c)* and by using synthetic

data with realistic sampling which allows a reproduction of a wavenumber $-1/2$ (not shown). This result is also typical for other SSWs even though we note that wavenumbers between -1 and 1 also occur (see e.g., *Pancheva et al., 2009b,c*).

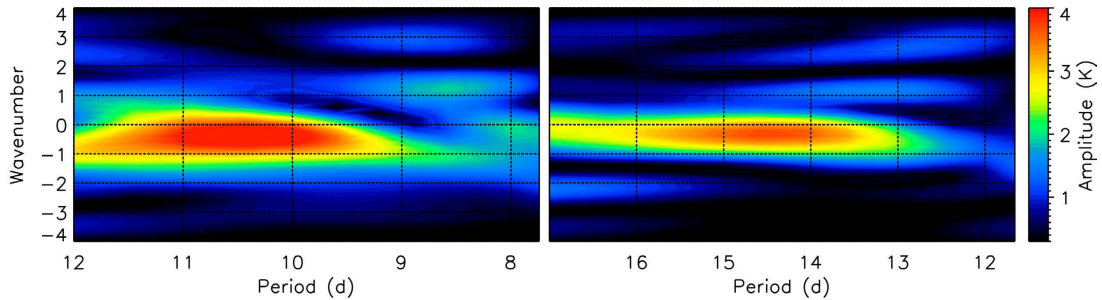


Figure 5.4 Period/wavenumber spectra from MLS temperature data at 69°N in a 5° latitude bin at 81 km for a 10-day wave (left) and a 16-day wave (right). Analyses were made between January 10 and February 19, 2009 for the 10-day wave and between December 21, 2008 and March 1, 2009 for the 16-day wave. For the study of the 10-day wave an interval of 40 days and for the 16-day wave an interval of 70 days is used, both centered at the time with the maximum amplitude of the PW detected from meteor radar wind observations.

These PWs are generated in the troposphere and propagate upward through the stratosphere into the mesosphere. Therefore, Figure 5.5 shows the amplitude of the 10-day wave with wavenumbers between -1 and 1 in the stratosphere and mesosphere for the winter 2008/09 based on MLS GPH data. There is a strong 10-day wave in the stratosphere in January and at the beginning of February. Around the stratospheric warming, there is an increased 10-day wave activity from the stratosphere up to the upper mesosphere. These features strongly indicate that PWs propagate from the lower atmosphere up to the mesosphere during this event.

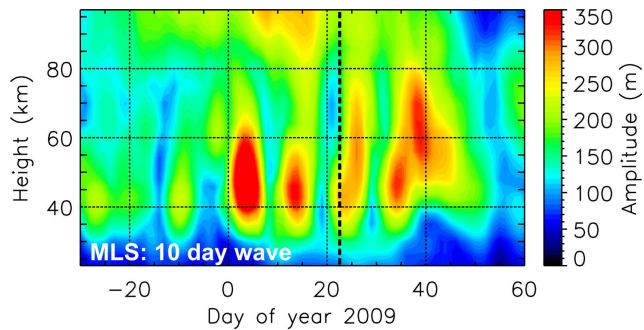


Figure 5.5 Amplitude of the 10-day wave with wavenumber -1 to 1 of MLS GPH data at 69°N in a 5° latitude band. The dashed line marks the beginning of the wind reversal at 10 hPa.

To understand the development of SSWs one has to consider the zonal mean circulation of the middle atmosphere during winter months. The middle atmosphere circulation is driven by the transfer of energy and momentum from the lower atmosphere. Vertically propagating PWs, as they occur in the winter hemisphere, transport energy and momentum upwards from the troposphere and equatorwards. This disturbs the equilibrium of the zonal flow and a compensatory circulation is needed – the resid-

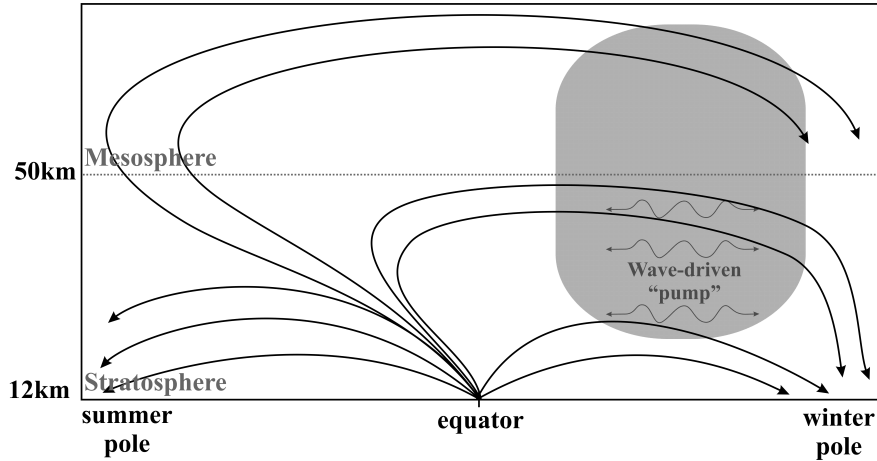


Figure 5.6 Schematic cross section of the wave driven residual circulation in the middle atmosphere and its role in transport with concentration on the winter hemisphere. The dotted line denotes the stratopause. Solid lines are contours of the TEM meridional circulation driven by wave-induced forcing (shaded region). Wavy double-headed arrows denote meridional transport and mixing by eddy motions. Based on *Brasseur and Solomon (1986)*, their section 3.6.2.

ual circulation. The residual circulation in the winter stratosphere and mesosphere is described by the Transformed Eulerian Mean equations (TEM). Based on this picture, Figure 5.6 schematically shows the residual circulation of the middle atmosphere. The residual circulation in the stratosphere is dominated by an upward transport of mass and trace chemicals in the tropics with a poleward transfer by a meridional drift in the lower stratosphere and a downward transport in the extra tropics. The mesospheric residual circulation is dominated by an upward motion from the equatorial troposphere into the summer pole mesosphere, a meridional drift from the summer to the winter hemisphere and a downward motion in the winter polar region. Note, that the residual circulation in the stratosphere is driven by dominating PWs while the mesospheric circulation is driven by dominating gravity waves (e.g., *Holton, 2004*). A detailed description of the atmospheric circulation pattern can be found for example in *Andrews et al. (1987)* and *Holton (2004)*. Note, that only the middle atmosphere is illustrated and therefore the streamlines are not closed.

As mentioned before, *Matsuno (1971)* was the first who modeled the development of a SSW. He noted that in application of the Charney-Drazin theorem (see section 2.5) a steady and non-dissipative PW with small amplitudes has no influence on the mean flow and therefore sought for conditions under which this theorem is violated. Among other points he found that PWs with growing amplitudes in time violate the Charney-Drazin theorem.

After Matsuno a SSW takes place in two phases as schematically shown in Figure 5.7. During the first phase of the SSW the upward and westward propagating PWs with growing amplitudes in time and height (due to the decreasing density) interact with the mean flow in the upper stratosphere. They lead to a westward acceleration of the flow and thus decelerate the eastward wind. Finally, the PWs reverse the zonal wind

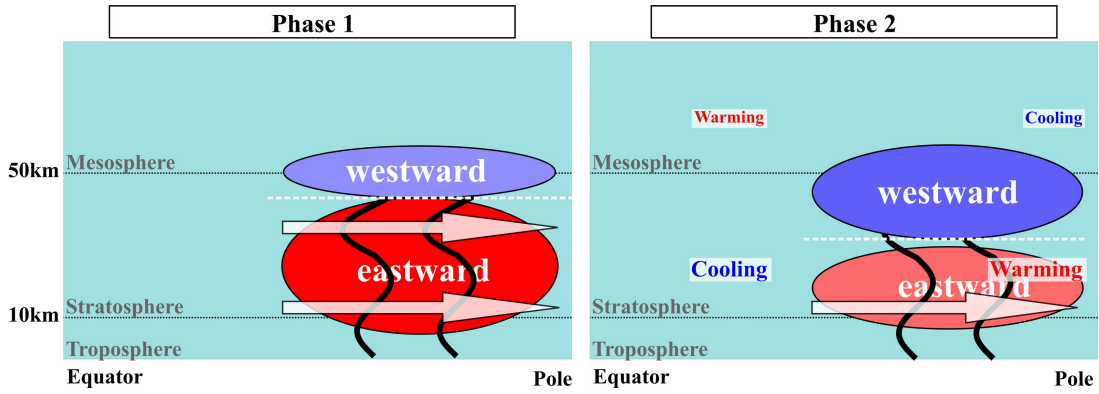


Figure 5.7 Schematic of the two-stage model of *Matsuno* (1971) of the generation of SSWs.

to a westward wind and a critical layer is generated (horizontal dashed line). The second phase includes the absorption of the PWs at the critical layer. The PWs are prevented from propagating further upward by the critical layer due to the Charney-Drazin criterion. This results in a westward acceleration of the mean flow at the bottom of the critical layer and hence the critical layer moves downward. Now the westward wind dominates above the critical layer while below the critical layer the eastward wind still dominates. This changes the PW pattern in the middle atmosphere and therefore the residual circulation.

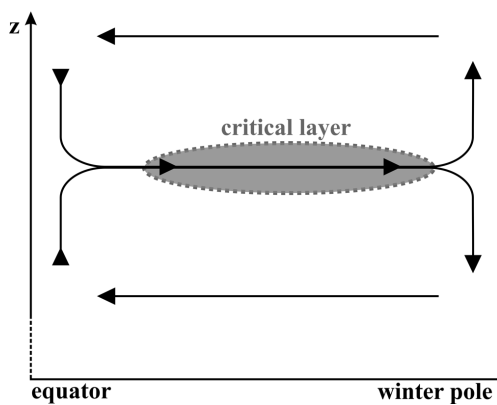


Figure 5.8 Scheme of the changed residual circulation during SSWs. Based on *Andrews et al.* (1987).

SSWs. This mechanism is generally accepted as the basic process underlying the development of a SSW.

Nevertheless, over the decades there have been a lot of studies with General Circulation Models (GCMs) which allows insights into the relevant processes beyond Matsuno's

model. Such studies used GCMs like for example the TIME–GCM¹ (*Liu and Roble*, 2002), WACCM² (*Beres et al.*, 2005) and KMCM³ (*Zülicke and Becker*, 2013) to name just a few. However, the models still fail to reproduce several of the salient features of SSWs as they are observed. For example, *Charlton et al.* (2007) show in a comparison of results from six GCMs with NCEP–NCAR⁴ reanalysis data that the number of SSW events and their frequency of occurrence in each month as well as the ratio between vortex splitting and vortex displacement events differs not only from model to model but differs also from the climatology of 40 years of reanalysis data.

Another open issue of modeling work concerns the influence of SSWs on the MLT region which has not at all been considered before the first successful simulation by *Liu and Roble* (2002). To illustrate the current abilities of models, *Pedatella et al.* (2014) compare the wind, temperature and PW behavior of four different nudged GCMs with each other and with MLS observations for the record warming 2009 up to the MLT region. This comparison shows that the stratospheric warming is well reproduced in all models compared to MLS observations. However, MLS observations reveal a mesospheric cooling associated with the SSW which is reproduced by only three of the four GCMs. *Pedatella et al.* (2014) found also differences in the altitudinal and latitudinal behavior of wind and PW behavior between the models itself but also compared with global MLS observations. Thus, current circulation models make significant steps beyond Matsuno’s model but they still fail to entirely reproduce and explain all salient features of SSWs.

Besides the model studies, the last decades have also produce a large number of observational studies. These studies confirm Matsuno’s model but also reveal other effects of SSWs which are not included in Matsuno’s model. For example, the mesospheric cooling was first observed by *Quiroz* (1969). Above this cooling, *Liu and Roble* (2002) additionally found a warming in the lower thermosphere of 20 – 30 K with simulations with the TIME–GCM/CCM3⁵ model. This result was confirmed with observations by e.g., *Siskind et al.* (2005), *Goncharenko and Zhang* (2008) and *Funke et al.* (2010). Following Matsuno, the zonal wind weakening or reversal during a SSW mostly takes place in the stratosphere. A few years later, *Gregory and Manson* (1975) observed a wind reversal or weakening also in the MLT region during major and minor SSWs. These observations have later been confirmed by many authors, e.g., *Cevolani* (1989, 1991), *Jacobi et al.* (1997), and *Hoffmann et al.* (2002, 2007) to name just a few. It is now generally accepted that SSW effects (temperature increase/decrease and wind weakening or reversal) can be observed from the stratosphere up to the lower thermosphere.

In the last decades, the 10- and 16-day wave have been determined as the major drivers of SSWs (e.g., *Jacobi et al.*, 1998a; *Krüger et al.*, 2004; *Palo et al.*, 2005; *Pancheva et al.*,

¹Thermosphere, Ionosphere, Mesosphere, and Electrodynamics General Circulation Model (TIME–GCM) from National Center for Atmospheric Research (NCAR)

²Whole Atmosphere Community Climate Model (WACCM) from NCAR

³Kühlungsborn Mechanistic Circulation Model (KMCM) from IAP

⁴National Centers for Environmental Prediction–National Center for Atmospheric Research (NCEP–NCAR)

⁵TIME–GCM/ Climate Community Model version 3

2008b) even though also other waves occur as well (e.g., *Azeem et al.*, 2005; *Chshyolkova et al.*, 2006, 2007; *Pancheva et al.*, 2009c).

A large number of case studies during the last ten years describe the individual response of SSWs in the stratosphere and MLT region, e.g., *Mukhtarov et al.* (2007), *Labitzke and Kunze* (2009), *Manney et al.* (2009), and *Kurihara et al.* (2010). They show that every SSW is connected with different effects, e.g., regarding the strength and temporal development of the temperature changes, the wind reversal and the wave structure. Thus, each SSW reveals its own particular properties even if some of the features are repeatable from event to event and hence, form a characteristic pattern. This characteristic pattern was investigated in the troposphere and stratosphere for example by *Charlton and Polvani* (2007). They constructed a mean climatology of vortex displacement and vortex splitting events from reanalysis data between 1958 and 2002. The comparison of the mean vortex displacement and splitting event shows differences in the seasonal distribution as well as in the tropospheric and stratospheric structure. A summary of the response of the mesospheric wind field to stratospheric circulation changes during the winter months between 1989 and 2000 was presented by *Hoffmann et al.* (2002). They showed a relation between the mesospheric wind variations and the changes of the meridional temperature gradient between 90°N and 60°N at 10 and 30 hPa. In addition, an indication for an enhanced long period wave activity (periods larger than 16 days) during SSWs was found.

The average behavior of waves in the troposphere and stratosphere was published by *Limpasuvan et al.* (2004). They studied the mean atmospheric flow and eddy fluxes of heat and momentum during the life cycle of a SSW from reanalysis data of 39 minor and major SSWs between 1958 and 2001. They found an anomalous wavenumber 1 forcing in the stratosphere and troposphere as well as a downward propagation of the anomalies during SSWs.

So far, only a few papers study the mesospheric wind behavior during SSW events (e.g., *Zülicke and Becker*, 2013). The majority of the SSW studies focus on the tropospheric and stratospheric behavior only. Thus, the question arises: **What is the average behavior of wind and especially of PWs in the middle atmosphere during SSWs?**

To answer this question, section 6.1 in the next chapter studies the composite behavior of wind and PWs from radar, satellite and assimilated model data of 6 major SSWs at the polar latitudes between 1998 and 2013.

Matsuno mentioned in his model temperature anomalies during SSWs also in the tropics which act vice versa to those at polar latitudes (cf. Figure 5.7). The first observations of temperature anomalies in the tropical stratosphere were done by *Fritz and Soules* (1970) with global satellite observation during the SSW in 1970. Later, a composite analysis of reanalysis data by *Kodera* (2006) confirmed these results and showed a clear effect of SSWs on the equatorial stratospheric temperature.

However, Matsuno did not consider the latitudinal expansion of SSW related polar effects and processes like the wind reversal or the PW activity in his model. Nevertheless, there are a lot of studies based on observations (e.g., *Manney et al.*, 2005,

Chapter 5 SSWs: State of the art and objectives of this thesis

2007; *Manson et al.*, 2006; *Hoffmann et al.*, 2007) and models (e.g., *Limpasuvan et al.*, 2004; *Liu et al.*, 2010) which show that SSW effects like the stratospheric warming, are strongest at polar latitudes, become weaker southward and vanish at mid-latitudes around 50°N.

During the DYANA⁶ campaign in 1990, *Cevolani* (1991) and *Singer et al.* (1994) observed a strong perturbation of the zonal wind between the upper stratosphere and lower thermosphere at mid-latitudes which was in some cases similarly strong compared to polar latitudes (*Singer et al.*, 1994). More recently *Stober et al.* (2012) observed a stronger westward wind at mid than at polar latitudes in the mesosphere during the SSW of 2010. This effect was also observed by *Chen et al.* (2012) over Langfang (39°N, 166°E) who additionally found a continuous westward wind band from the pole down to the tropics during the 2010 event from MLS gradient winds. This continuous westward wind band is an unusual phenomenon and even if *Chen et al.* (2012) studied the latitudinal and altitudinal structure of the wind reversal during the event in 2010 they gave no possible explanation for this phenomenon. Thus, the question arises: **Are there latitudinal and longitudinal variabilities of SSWs and if so, which process determines these variabilities?**

There are only a few studies considering the latitudinal extension of the circulation changes during SSWs. Most of them are based on model simulations. The composite analysis of *Charlton and Polvani* (2007) with the NCEP-NCAR model shows that SSW effects like the zonal wind reversal expand more southwards during splitting than during displacement events. *Limpasuvan et al.* (2012) showed an enhanced effect of SSWs on the circulation at latitudes south of 40°N in connection with splitting events using the WACCM model. These studies found a southward extension of the SSW only in splitting events but the SSW in 2010, where the continuous westward wind band occurred, is categorized as an displacement event (e.g., *Kuttippurath and Nikulin*, 2012). Thus, it is still unclear if this phenomenon was unique and how it developed. First initial studies of the latitudinal and altitudinal structure of the zonal wind during recent SSW events show that beside 2010 also the major warming in 2009 and the minor warming in 2012 show this continuous westward wind band too. Thus, the aim of section 6.2 in the next chapter is to compare the latitudinal and altitudinal structure of wind, temperature and PWs during normal and latitudinal displaced SSW events. For a latitudinal normal SSW, the event in 2006 was representatively chosen and compared to the three latitudinal displaced SSW events in 2009, 2010 and 2012.

Hence, to get a better process understanding of SSWs, the next chapter will consider at first the average behavior of wind and PWs during SSWs in polar latitudes which then is followed by a comparison of the latitudinal and altitudinal structure of wind, temperature and PWs of different SSW events.

⁶DYANA = DYnamics Adapted Network for the Atmosphere

Chapter 6 Characteristics of PWs during Sudden Stratospheric Warmings

Within this chapter the average characteristics of PWs during SSWs as well as their latitudinal variability are studied. In section 6.1, the average behavior of winds and PWs in the stratosphere and mesosphere during six major SSWs between 1998 and 2013 is investigated at polar latitudes with the help of a composite analysis. Normally, SSWs occur strongest at the pole, become weaker towards the south and vanish at mid latitudes. However, there are SSWs which indicate a zonal wind reversal at lower latitudes as well. Section 6.2 therefore compares the latitudinal and altitudinal structure of wind, temperature and PWs of the latitudinally normal SSW 2006 with the latitudinally displaced SSWs in 2009, 2010 and 2012. Longitudinal variabilities which also occur are briefly discussed in section 6.3.

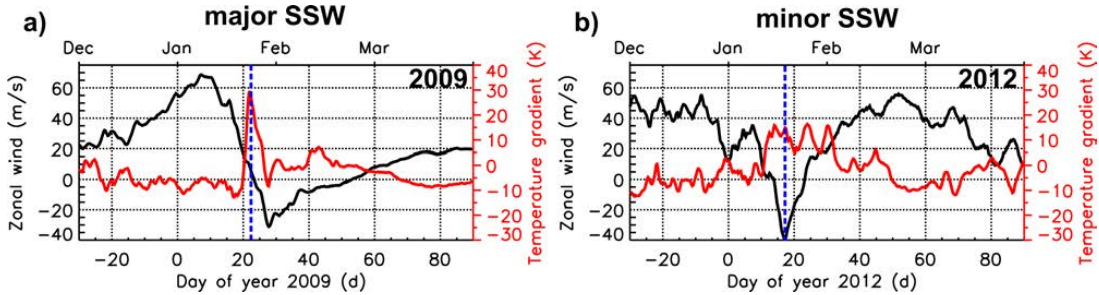


Figure 6.1 Zonal mean zonal wind (black) at 60°N at a) 10 hPa and b) at 1 hPa and zonal mean temperature gradient (red) between 90°N and 60°N at 10 hPa for the winters of a) 2008/09 and b) 2011/12 from MERRA data. The blue dashed line marks the central day d_c of the corresponding SSW.

To analyze different SSWs by means of a composite analysis, a reference day, the so called central day d_c , is needed. For major SSWs the central day is defined, following *Labitzke and Naujokat* (2000), as the day where at 60°N at 10 hPa the zonal mean zonal wind reverses and the temperature gradient between 60°N and 90°N at 10 hPa has a maximum. As an example, Figure 6.1(a) shows the temporal development of the zonal mean zonal wind (black) at 60°N and the temperature gradient (red) between 60°N and 90°N both at 10 hPa for the winter 2008/09 from MERRA data. At mid January the zonal mean zonal wind begins to decrease and reverses on January 22 where at the same time the temperature gradient has a maximum. This day is the central day for

the major warming in 2009.

The central day of a minor warming is defined as the day where the zonal mean zonal wind at 10 hPa has its minimum (e.g., *Hoffmann et al.*, 2002). Only in some cases like in 2012 this criterion is not clear enough, because the wind changes do not extend low enough into the stratosphere. In such cases the zonal mean zonal wind is considered at 1 hPa instead of 10 hPa. Figure 6.1(b) shows the temporal development of the zonal mean zonal wind in the winter of 2011/12 from MERRA data at 1 hPa. The minimum occurs on January 17 2012.

The central days of all SSWs considered in this study are listed in Table 6.1.

major warmings		minor warmings	
year	central day	year	central day
1998	15 December	2005	27 February
2004	10 January	2007	7 February
2006	22 January	2011	3 February
2009	21 January	2012	17 January
2010	28 January		
2013	5 January		

Table 6.1 Central days of the major (left) and minor (right) SSWs considered in this study.

6.1 Composite analysis of the temporal development of PWs during SSWs¹

The superimposed epoch analysis is applied to local wind measurements at Andenes (69°N) and global satellite data (MLS) to investigate the average behavior of wind and PWs in the stratosphere and mesosphere. This study is focused on those major SSWs which have a reinstated regular winterly circulation after the warming. This is valid for six events in the available data set of 16 years: 1998/99, 2004, 2006, 2009, 2010 and 2013. Note that the major warming in late February 2008 is not included due to the unfulfilled condition of the reinstated winterly circulation after the warming (see e.g., *Wang and Alexander*, 2009). Additionally, a comparison of the composite of the major events and the weak minor warming in 2011 is shown in order to distinguish between normal winter and special major SSW structures.

A composite of the zonal wind at Andenes during major SSWs is shown in Figure 6.2 (left) from MERRA (10 – 70 km) and MR (82 – 96 km) data of the years 1999, 2004, 2006, 2009, 2010 and 2013. There is a rapid wind reversal from eastward to westward wind which extends from the stratosphere up to the upper mesosphere with an earlier

¹This section was published in a similar form in the *Journal of Atmospheric and Solar-Terrestrial Physics* (*Matthias et al.*, 2012a). It was co-authored by Peter Hoffmann, Markus Rapp and Gerd Baumgarten at the Leibniz Institute of Atmospheric Physics.

6.1 Composite analysis of the temporal development of PWs during SSWs

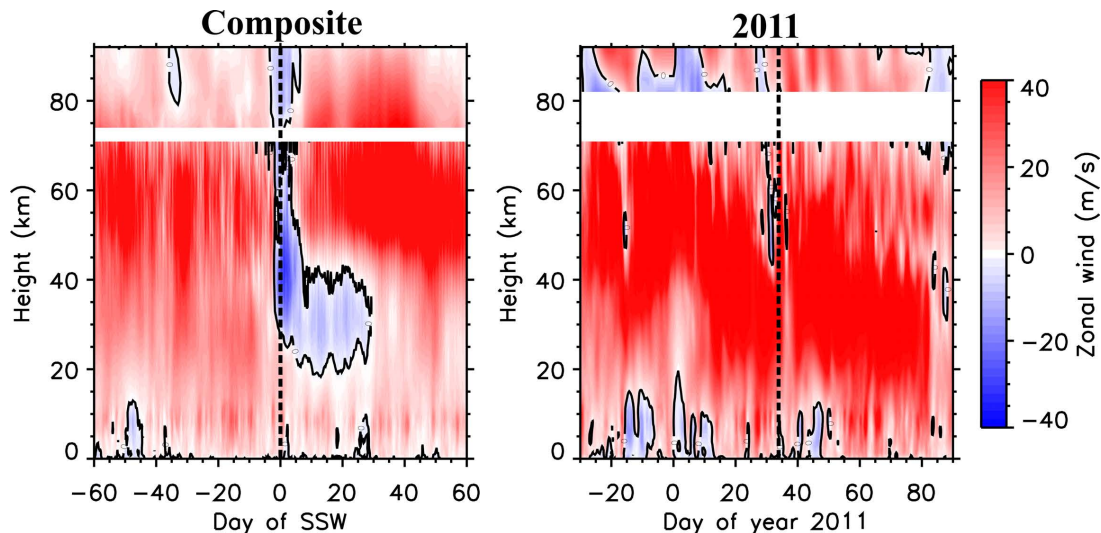


Figure 6.2 **Left:** Composite of zonal wind centered on central day d_c ($d = 0$) at Andenes for the years 1999, 2004, 2006, 2009, 2010 and 2013 (0 – 72 km: MERRA; 74 – 92 km: MF radar). **Right:** Zonal wind at Andenes for the winter 2010/11 from MERRA (0 – 72 km) and MR (82 – 96 km) data. The dashed lines show the central days of the SSWs respectively.

onset of the wind reversal in the mesosphere of around 4 days. This is confirmed by a cross-correlation between the wind in 84 and 32 km (not shown). Similar observations were made by *Kurihara et al.* (2010) during the record warming in 2009. They found this downward propagation of the wind reversal from the mesosphere down to the stratosphere within a few days, too.

The composite shows also a longer lasting summerly westward wind in the stratosphere than in the mesosphere. This was also observed by *Manney et al.* (2009) during the SSW in 2009. Additionally, the eastward winds in the mesosphere occur much stronger after the warming than before. Note that the wind reversal differs in strength, duration time, altitude and onset time from event to event. Nevertheless, the composite shows clear structures that occur in most of the major warmings.

By the way of comparison, Figure 6.2 (right) shows the zonal wind development during the winter of 2010/11 at Andenes, from MERRA and MR data, with a small minor warming (dashed line) at the beginning of February. While a wind reversal occurs in the upper mesosphere, no significant wind reversal is observable in the stratosphere compared to the composite. This missing stratospheric wind reversal is the most distinctive difference between the composite of the major warmings and the minor warming in 2011. Another difference is the very stable stratosphere and lower mesosphere in 2011 compared to the composite of the major warmings. However, both show a high variability in the upper mesosphere. This variability is caused by an increased PW activity which generally occurs winter months (see e.g., *Day et al.*, 2011).

As discussed in chapter 4, the transient 10- and 16-day waves are the most important PWs for SSWs besides the stationary waves. The composite of the amplitude of the 10- (top) and 16-day wave (bottom) of meridional mesospheric winds from MR at

Amplitudes of the major SSWs in 2004, 2006, 2009, 2010 and 2013 is shown in Figure 6.3.

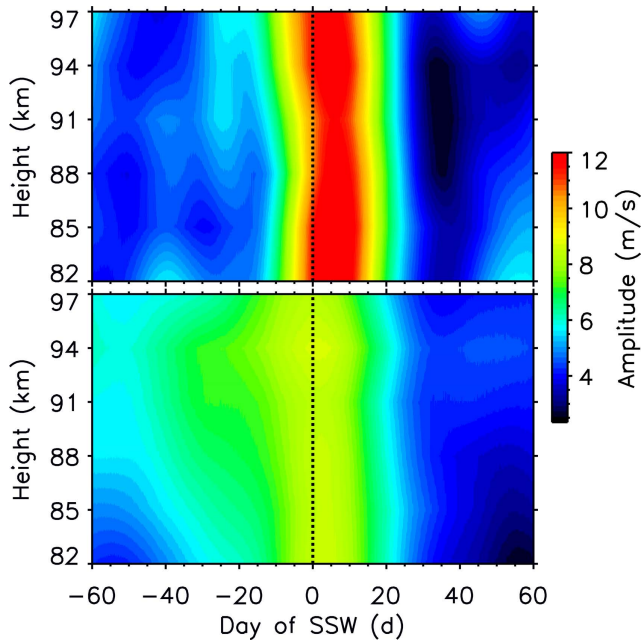


Figure 6.3 Composite of the amplitude of the 10-day (top) and 16-day wave (bottom) of meridional wind centered on the central day d_c ($d = 0$, dashed line) at Andenes for the years 2004, 2006, 2009, 2010 and 2013 from MR data.

A strong 10-day wave occurs around the central day as well as a weaker 16-day wave. The weak 16-day wave is also observable before the warming in the mesosphere. Comparisons of these results with Figure 8 from *Matthias et al.* (2012a), where the same analysis was conducted but without the major warming of 2013, show that the results are robust for the 10-day wave but shifted toward the central day in the current analysis due to a strong 16-day wave around the central day in 2013 (not shown).

From local radar data alone, only the amplitudes of the PWs and their temporal development can be derived in the mesosphere but no further characteristics.

As discussed in chapter 5 and

shown in Figure 5.4 on page 35, most of the PWs considered in this study have wavenumbers between -1 and 1 . Hence, in the following wave analysis with global MLS data only 10- and 16-day waves with wavenumbers between -1 and 1 are considered.

The composite of the 10- and 16-day wave with wavenumbers between -1 and 1 in the middle atmosphere is shown in Figure 6.4 (left) from MLS GPH data at 69°N in a 5° latitude band of the SSWs in 2006, 2009, 2010 and 2013. The 10-day wave shows strong amplitudes 20 days around the central day extending from the stratosphere up to the upper mesosphere. The 16-day wave occurs strongly in the stratosphere and lower mesosphere and has a small minimum at the same time where the 10-day wave occurs. Note that single SSWs could have different PW patterns. In 2010 for example, the 16-day wave is much stronger in the mesosphere than the 10-day wave (not shown). Studies of the major warming in the winter of 2003/04 published by *Pancheva et al.* (2009b) using global SABER² satellite data show a strong 16-day wave before the warming in the stratosphere and mesosphere at 50°N . Other studies of *Palo et al.* (2005) show a strong 10-day wave during the record warming of 2002 in the southern hemisphere from the stratosphere up to the lower thermosphere as well. These observations of the PW activity around a single major SSW fit well to the composite analysis

²SABER = Sounding of the Atmosphere using Broadband Emission Radiometry

6.1 Composite analysis of the temporal development of PWs during SSWs

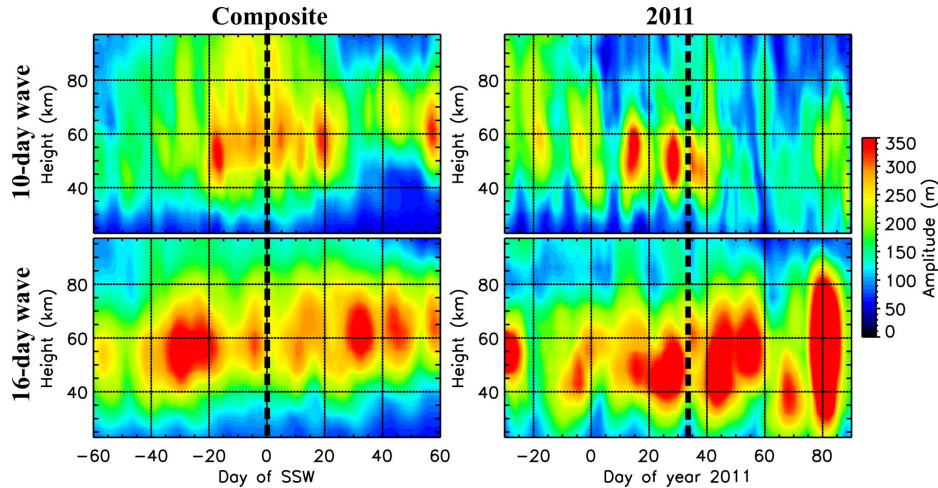


Figure 6.4 Left: Composite of the amplitude of the 10-day (top) and 16-day wave (bottom) with wavenumber -1 to 1 of GPH data from MLS centered around the central day d_c ($d = 0$, dashed line) at 69°N in a 5° latitude band for the years 2006, 2009, 2010 and 2013. Right: Same as left just for the winter of 2010/11. The dashed line marks the central day of the minor warming in 2011.

although one must consider that each SSW has its own characteristics. Comparisons of these results with the quiet winter of 2010/11 (see Figure 6.4 right) also show a strong 10-day wave around the central day in 2011 but only in the stratosphere and not in the upper mesosphere like during the major events. In 2011 the 16-day wave occurs strongly in the stratosphere and lower mesosphere like in the composite analysis but does not have a minimum where the 10-day wave occurs.

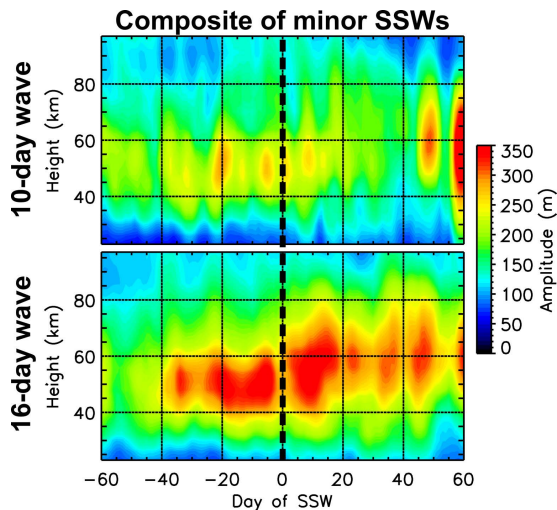


Figure 6.5 Same as Figure 6.4 left but for the minor warmings in 2005, 2007, 2011 and 2012.

This comparison suggests that the height range in which a strong PW activity is observable is crucial to the occurrence of a major or minor warming. Hence, Figure 6.5 similarly to Figure 6.4 shows the composite of the 10- and 16-day wave from MLS GPH data for the minor warmings in 2005, 2007, 2011 and 2012. Note that the minor warmings in 2008 are not included in this study since they are merged into each other too strong. The figure shows a strong 10-day wave around the central day in the stratosphere and lower mesosphere but, unlike during the major warmings, not in the upper mesosphere. Similarly to 2011, the 16-day wave occurs strongly

in the stratosphere and lower mesosphere without a minimum around the central day. These results strengthen the assumption that if PWs can propagate upward into the upper mesosphere a major SSW occurs, otherwise a minor warming develops. Minor warmings are not in the main focus of the community. Only *Cevolani* (1989) studied long period waves during minor SSWs at mid latitudes in the mesosphere and thermosphere. Below 100 km he also found a 10- and 16-day oscillation but he considered it not to be in connection with the stratospheric behavior of PWs. It would be interesting to compare the wind, temperature and the PW activity before minor and major warmings to find indications for the upward propagating ability of PW during major SSWs. Nevertheless, it is beyond the scope of this thesis, but it would be a reasonable project for the future.

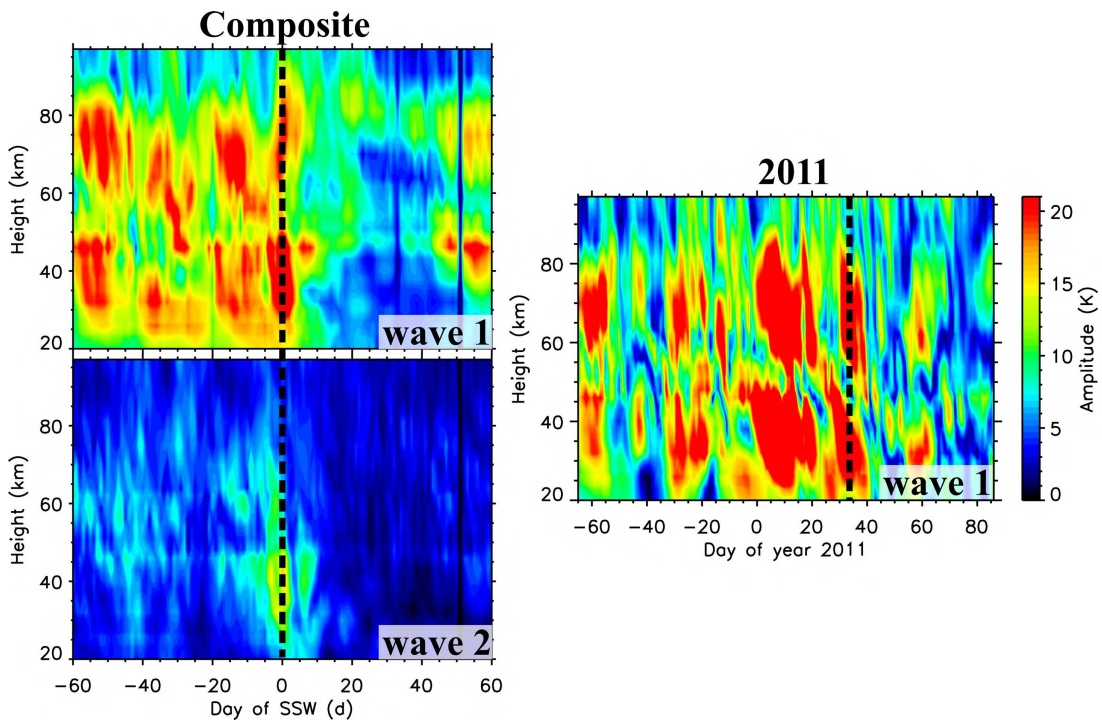


Figure 6.6 **Left:** Composite of the amplitude of the stationary wave 1 (top) and 2 (bottom) centered around the central day d_c ($d = 0$, dashed line) at 69°N in a 5° latitude bin for the SSWs in 2006, 2009, 2010 and 2013 from MLS temperature data. **Right:** Same as left but for the amplitude of the stationary wave 1 during winter 2010/11.

Another type of PWs which are important for the development of a SSW are stationary waves. The composite of the stationary wave 1 and 2 for the major warmings in 2006, 2009, 2010 and 2013 from MLS temperature data is shown in Figure 6.6. The stationary wave 1 is strongly active in the stratosphere and mesosphere throughout the winter until the onset of the SSW. A rapid decrease of the stationary wave activity follows. It takes approximately 30 days to reestablish the stationary wave 1 and therefore the polar vortex. The stationary wave 2 is much weaker and has a maximum at the

6.1 Composite analysis of the temporal development of PWs during SSWs

central day in the stratosphere. These results agree with a study of *Pancheva et al.* (2009b) of the altitudinal and temporal structure of PWs in the winter of 2003/04 and of *Palo et al.* (2005) during the southern hemispheric SSW event in 2002. The low stationary PW activity after the central day is in good agreement with the Charney-Drazin criterion (see section 2.3). Since the zonal wind is still reversed in the stratosphere (cf. Figure 6.2) an upward propagation of waves from the troposphere is not possible.

The quiet winter of 2010/11 (see Figure 6.6 right) shows a strong stationary wave 1 throughout the winter with only a small and short minimum after the central day of the minor warming in 2011 with respect to the major event results. The decrease in the amplitude after day 65 is caused by the transition from winter to summer.

These composite analyses of wind and PWs include the record warming of 2009. To exclude a dominating effect of this event in the composite analyses, the analyses were repeated without the event in 2009 and show very similar results (not shown). One exception is the amplitude of the stationary wave 2. Since the record warming of 2009 was a vortex splitting event (e.g., *Manney et al.*, 2009) the composite of the stationary wave 2 is dominated by this event.

Summarizing, the composite analyses of effects during major SSWs at polar latitudes show the onset of the wind reversal in the mesosphere around 4 days earlier than in the stratosphere at Andenes (69°N). A strong 10-day wave occurs around the central day from the stratosphere up to the upper mesosphere while the 16-day wave strongly occurs in the stratosphere only. The stationary wave 1 is strong until the central day and decreases rapidly afterwards while the stationary wave 2 is much weaker and occurs strongest around the central day. The comparison of the major event results with the composite of minor SSWs allow the assumption: If a PW can propagate up to the upper mesosphere then a major warming occurs, otherwise it is a minor event.

This study shows average characteristics of SSWs at polar latitudes where the SSW effects occur strongest in general. One might ask whether these results also hold for mid latitudes – the edge of the polar vortex? Comparisons of the zonal wind and PW activity at mid and high latitudes by *Stober et al.* (2012) show a stronger westward wind during the SSW in 2010 at Collm and Juliusruh (mid-latitudes) than at Andenes (polar latitudes). This southward shift of the SSW effects and PW activity was also observed in initial studies during two further events: during the major warming in 2009 and during the minor warming in 2012. The next section shows a comparison of these three latitudinal displaced events with a normal occurring SSW by an investigation of latitudinal differences of the zonal wind, temperature and PW activity and tries to find reasons for the latitudinal displacement.

6.2 Latitudinal variabilities of SSWs³

In general, SSWs are strongest at the pole, become weaker towards the south and vanish around 50°N (e.g., *Limpasuvan et al.*, 2004; *Liu et al.*, 2010). However, recently there were three events (the major SSWs in 2009 and 2010 and the minor SSW in 2012) where the westward wind occurred similar strong or even stronger at mid than at polar latitudes either in the mesosphere or in the stratosphere. In this section a comparison is shown of the differences in the latitudinal structure of the zonal wind, temperature and PW activity between a “normal” polar dominated event, where the SSW in 2006 was representatively chosen, and the latitudinal displaced events in 2009, 2010 and 2012.

6.2.1 Zonal wind characteristics

Figure 6.7 shows the zonal wind at Andenes (black) and Juliusruh (red), representatively for polar and mid latitudes, at 85 km (MR data) and at 49 km (MERRA data) centered on the central day of the SSWs in 2006, 2009, 2010 and 2012. Note that since the MR in Juliusruh started operating later in 2006 this data was substituted by MF radar data also located at Juliusruh.

Starting with the SSW in 2006, the mesospheric wind reversal from eastward to westward wind occurs before the central day at Andenes and at the central day at Juliusruh. The maximum of the westward wind is stronger at polar than at mid latitudes which is also true for the stratosphere. Different from the mesosphere, the wind reversal starts before the central day in the stratosphere at both locations but first at Juliusruh and after that at Andenes. After the central day the zonal wind at Andenes shows a rapid increase of the eastward wind in the mesosphere with no significant wave activity while the eastward wind at Juliusruh is weaker and shows strong wave activity. In the stratosphere at 49 km, Juliusruh again shows a wave-like structure after the central day while the zonal wind at Andenes remains quiet. In contrast to the mesosphere the eastward winds occur more strongly after the central day at Juliusruh than at Andenes. This behavior is referred to as a “normal” SSW with a typical latitudinal behavior. Thus, the SSW of 2006 is representative for all normal SSWs and will therefore in the following be used for comparison with the other three events considered here.

In contrast to the normal event in 2006, the events in 2009, 2010 and 2012 show a simultaneous or even earlier wind reversal in the mesosphere at Juliusruh than at Andenes and a temporal variation in time of the onset of the wind reversal in the stratosphere. During the events in 2010 and 2012 the westward wind is even stronger at Juliusruh than at Andenes in the mesosphere and vice versa in the stratosphere. However, the vortex splitting event in 2009 shows a stronger westward wind at Juliusruh than at Andenes in the stratosphere but not in the mesosphere. Nevertheless, the westward wind is stronger at Juliusruh than at Andenes either in the mesosphere or in the strato-

³This section was published in a similar form in *Annales Geophysicae* (*Matthias et al.*, 2013). It was co-authored by Peter Hoffmann and Gunter Stober at the Leibniz Institute of Atmospheric Physics, Markus Rapp at the Deutsches Zentrum für Luft und Raumfahrt in Oberpfaffenhofen, Alan Manson and Chris Meek at the University of Saskatchewan and Peter Brown at the University of Western Ontario.

6.2 Latitudinal variabilities of SSWs

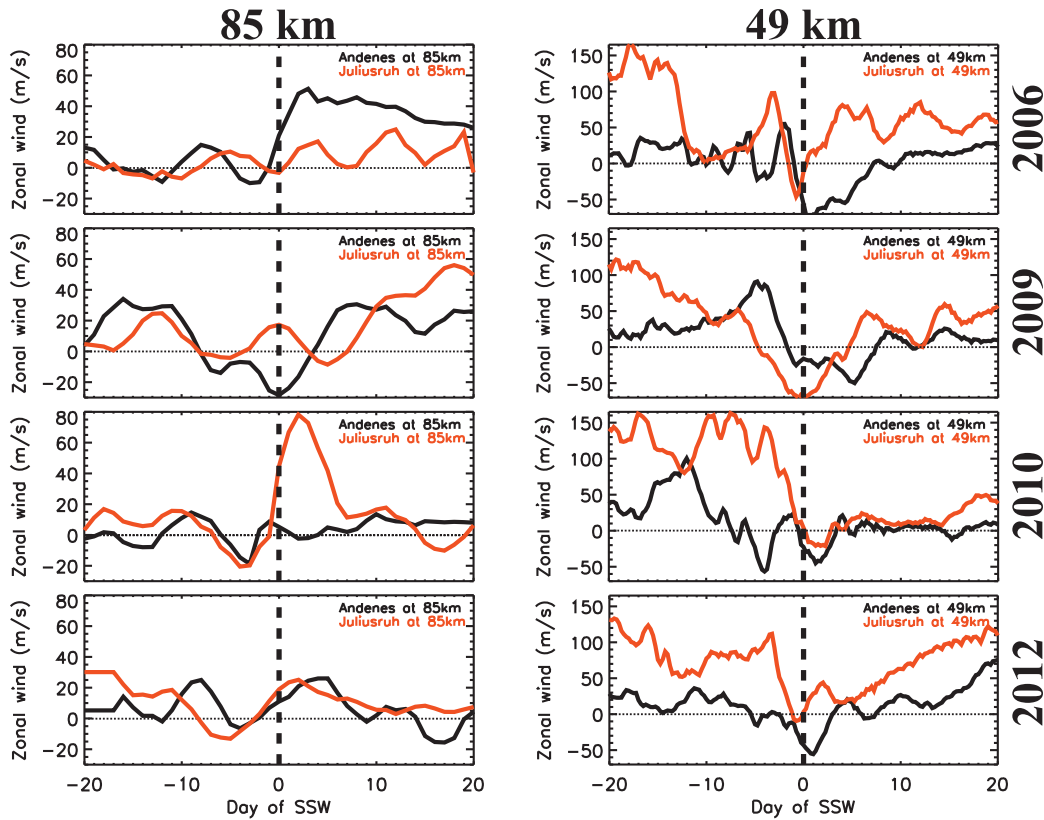


Figure 6.7 Zonal wind at Andenes (black) and Juliusruh (red) at 85 km (left) from MR and 49 km (right) from MERRA data centered around the central day (black dashed line) of the respective SSW of 2006, 2009, 2010 and 2012. Terdiurnal, semidiurnal and diurnal tides were removed for the MR data. This figure is taken from *Matthias et al.* (2013).

sphere during the latitudinal displaced events. Additionally, these three events show an increased wave activity in the mesosphere before and after the central day compared to 2006. One exception is Juliusruh after the central day in 2012 where no wave-like behavior is observed. In the stratosphere the wave activity after the central day varies. While in 2009 Andenes and Juliusruh show a strong wave activity after the central day, the event in 2010 has no significant wave-like behavior at both locations. The minor warming in 2012 shows a wave-like behavior only at Andenes after the central day. As in 2006, the eastward wind after the central day is stronger at Juliusruh than at Andenes during the three latitudinal displaced events but occurs weaker in Juliusruh compared to 2006. These results indicate an unusual latitudinal behavior of the events in 2009, 2010 and 2012 with stronger SSW effects at mid- than at polar latitudes.

For a global view of the zonal wind behavior of the four SSWs, Figure 6.8 shows the zonal mean zonal wind from MERRA as a function of latitude and altitude 5 days before, at the central day and 5 days after the central day. Five days before the central day of each warming except for 2009 a weak wind reversal occurs at the pole in

Chapter 6 Characteristics of PWs during Sudden Stratospheric Warmings

the stratosphere and mesosphere whereas these reversals are separated by an eastward wind around 50 to 60 km. In contrast to this a strong eastward wind appears at high and mid-latitudes 5 days before the central day of the record warming in 2009.

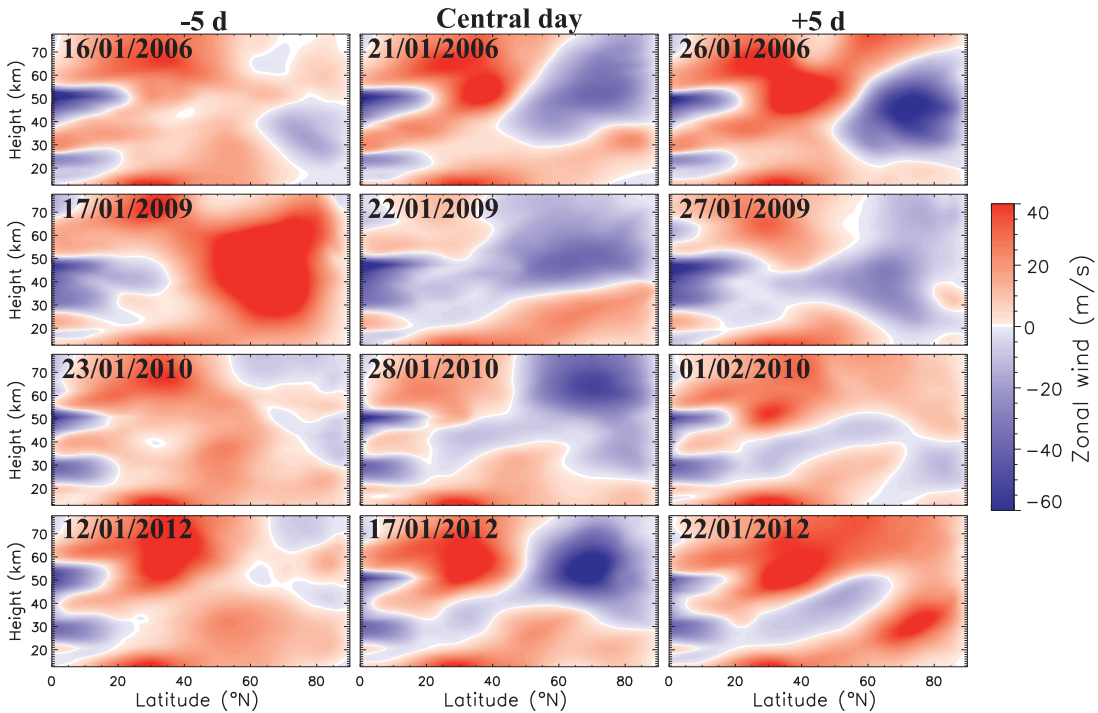


Figure 6.8 Zonal mean zonal wind 5 days before, at and 5 days after the central day of the years 2006, 2009, 2010 and 2012 as a function of latitude and height from MERRA data. This figure is taken from *Matthias et al.* (2013).

On the central day, the zonal wind behavior of the three latitudinal displaced events differs strongly from the one in 2006. While in 2006 the wind reversal occurs from polar mesosphere and upper stratosphere to stratospheric mid-latitudes, the other events in 2009, 2010 and 2012 show a continuous westward wind band between the pole and 20°N. Hence, the most remarkable difference between the latitudinal displaced events and the normal event in 2006 is the continuous westward wind band between the pole and the tropics.

Five days after the central day the wind reversal pattern of each SSW looks very similar to the one on the central day, but it has moved downward. However, in 2012, the polar latitudes show a strong eastward wind from stratosphere to mesosphere, i.e., the wind reverses back from westward to eastward. The westward wind still dominates at mid and lower latitudes in the stratosphere. It seems that the wind reversal breaks down from the polar mesosphere to the lower latitude stratosphere in 2012. Note that there is a dependence from the selected central day. For example, in 2010 a second longer lasting wind reversal occurs after a short one around January 28, which was chosen as the central day in this thesis. *Chen et al.* (2012) discussed the definition of the central day for 2010 and rescheduled the central day on February 2, 2010 in his study.

6.2 Latitudinal variabilities of SSWs

These results are corroborated by case studies of the SSW in 2010 by *Chen et al.* (2012) using MLS gradient winds and by *Stober et al.* (2012) using local radar measurements at 54°N. However, the continuous westward wind band between the pole and 20°N could not be observed by the composite analysis of 39 major and minor warmings of *Limpasuvan et al.* (2004) with NCEP–NCAR reanalysis data. Only the distinguished composite analysis of vortex displacement and splitting events of *Charlton and Polvani* (2007) with NCEP–NCAR and ECMWF reanalysis data showed a wind reversal from the pole down to 30°N during splitting events, but without a continuous westward wind band from the pole to the tropics. A possible explanation for the continuous westward wind band is discussed later in this section.

This study shows three exceptional SSW events with respect to their latitudinal structure within a short period of time (2009 – 2012). Thus the question arises whether those events really are exceptions or not. The composite analysis of 39 major and minor warmings between 1958 and 2001 from NCEP–NCAR reanalysis data of *Limpasuvan et al.* (2004) shows no evidence for a continuous westward wind band during the warmings. Only the composite analysis of *Charlton and Polvani* (2007) shows a lightly southward extended westward wind during vortex splitting events but again no continuous wind band between the pole and lower latitudes. Also case studies for individual events as were published for example in *Hoffmann et al.* (2007) and especially in *Mukhtarov et al.* (2007) show no evidence for a latitudinal displaced SSW other than the one considered in this study. Therefore, the latitudinal displaced events studied here are exceptional even if they occur in a temporally short interval.

6.2.2 Temperature characteristics

Once the zonal mean zonal wind shows a continuous westward wind band during the latitudinal displaced SSW, one can assume that similar structures are observable in the latitudinal and altitudinal pattern of the zonal mean temperature. Therefore, Figure 6.9 shows the daily mean zonal mean MLS temperature at 20, 40, 59 and 81 km as a function of time and latitude for 2006, 2009, 2010 and 2012. The white dashed line marks the central day of the corresponding SSW. In the following, each altitude from bottom to top will be described separately for all years.

At 20 km a long lasting warming occurs after the central day of each SSW. In 2006 this warming is observable from the pole down to 60°N while in 2009 and 2010 it occurs from the pole down to 50°N. An exception is the event in 2012 where this warming occurs between 50°N and 70°N, i.e., not at the pole. Thus, a continuous band of high temperatures between the pole and 20°N as observed in the zonal wind reversal is not observable in the latitudinal temperature structure at 20 km. Note that in 2010 the warming has a time delay of around ~ 15 days after the central day. The cause for this time shift might be the temporal development of the zonal wind in 2010 as discussed above. The rescheduled central day by *Chen et al.* (2012) on February 2, 2010 is in good agreement with the warming at 20 km observed here. The extraordinary behavior of the temperature changes during the warming of 2012 will be further investigated later in this section.

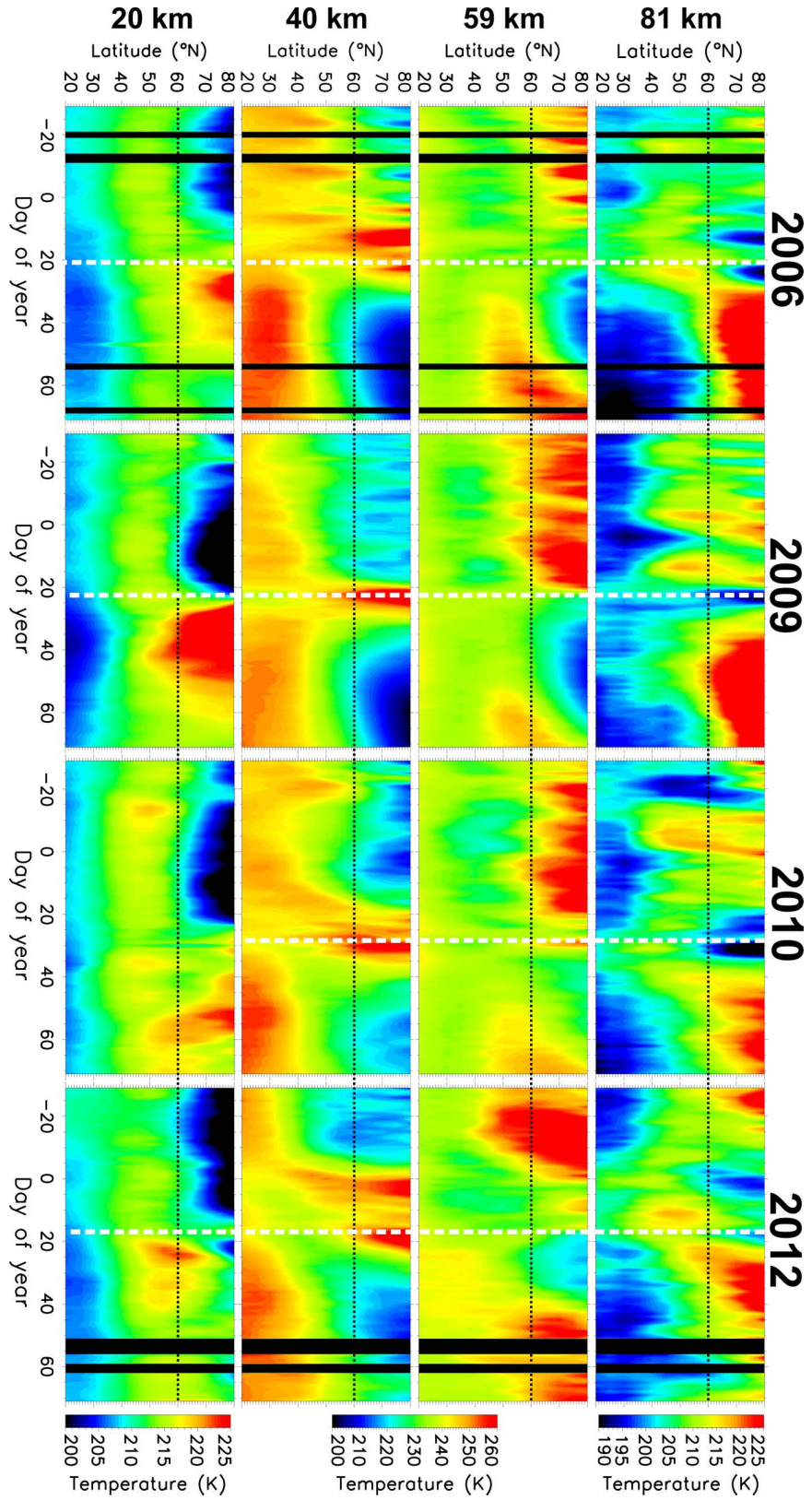


Figure 6.9 Zonal mean temperature at 20, 40, 59 and 81 km from MLS for the winters of 2005/06, 2008/09, 2009/10 and 2011/12. The vertical white dashed line marks the central day of the respective SSW and the horizontal black dashed line at 60°N is inserted to guide the eye.

6.2 Latitudinal variabilities of SSWs

At 40 km all SSWs show a warming from pole down to $\sim 60^\circ\text{N}$ at the central day, but again no continuous band to the tropics. After these warmings a temperature increase occurs in the subtropics between 20°N and 40°N . This indicates an equatorward progression of the warming in the stratosphere around 40 km which can be influenced by the mean meridional residual circulation. However, there is no latitudinal difference in the temperature changes during the warmings between the normal event in 2006 and latitudinal displaced events in 2009, 2010 and 2012. Only the behavior of the temperatures at mid-latitudes around 50°N before the central day shows significant differences. While in 2006 the low polar temperatures before the warming reach down to 60°N , they are also observed down to 40°N and 50°N during the SSWs of 2009, 2010 and 2012. Thus, the stratospheric mid-latitudinal temperature is much lower before the latitudinal displaced events than before the normal event 2006.

The mesospheric temperature at 59 km shows a cooling from the pole down to $\sim 60^\circ\text{N}$ after the corresponding central days which varies in length of time and strength from event to event. During this polar cooling a warming, which starts around 50°N , occurs and spreads out to the pole with time. The polar and mid-latitudinal mesospheric temperature before all events is very variable due to increased PW activity and more stable afterwards due to the decreased PW activity after SSWs (see section 6.1).

At 81 km the mesospheric cooling is narrower during all events than at 59 km and occurs around the central day. This cooling occurs from pole down to $\sim 60^\circ\text{N}$ during all events except in 2009, where the low temperatures are observable from the pole to the tropics. Nevertheless, the minimum of these low temperatures is located between the pole and $\sim 60^\circ\text{N}$. After the central day a strong warming occurs at polar latitudes whereas this warming appears weaker in 2010 and 2012 than in 2006 and 2009. Again, the polar mesosphere is very variable in all cases before the SSW. This can be also attributed to the increased PW activity.

Besides the latitudinal variations of the temperature a downward progression from mesosphere to stratosphere is observable during all events. This downward progression could also be observed in the temporal development of the zonal wind reversal as mentioned above. Here, the mesospheric cooling first occurs in the upper mesosphere at the central day and then moves downward to the lower mesosphere around 59 km where it also lasts much longer. This downward movement can also be continued to stratospheric altitudes where after the stratospheric polar warming the temperature decreases again to a typical polar stratospheric level. Thus, there is a downward movement of the mesospheric cooling to stratospheric heights. A similar behavior can be observed in the stratosphere. At 40 km the stratospheric warming occurs around the central day while the warming at 20 km in the lower stratosphere appears afterwards and lasts much longer. Note that this downward movement of the cooling/warming during SSWs is consistent with the downward progression of the wind reversal as discussed by *Hoffmann et al.* (2007) and found in the composite analysis of *Matthias et al.* (2012a).

Summarizing, in general there is no continuous band of high/low temperatures in the stratosphere/mesosphere between the pole and lower latitudes during the latitudinal displaced SSWs as it was found in the zonal wind reversal. Nevertheless, some temperature changes reach further south during the latitudinal displaced events than during the SSW in 2006. Additionally, the exceptional SSWs in 2009, 2010 and 2012 (with a con-

Chapter 6 Characteristics of PWs during Sudden Stratospheric Warmings

tinuous westward wind band between pole and lower latitudes) show low temperatures between 35°N and 60°N in the upper stratosphere before the central day compared to the polar dominated event in 2006. Besides the stratospheric equatorward movement of the warming a downward progression of the stratospheric warming and mesospheric cooling is also observed during all events.

6.2.3 PW characteristics

As mentioned before, SSWs are caused by the interaction of PWs with the mean flow. Thus, it is assumed that the reason for the continuous westward wind band from the pole to lower latitudes and the temperature changes at mid and lower latitudes during the latitudinal displaced SSWs is the increased PW activity at the same latitudes.

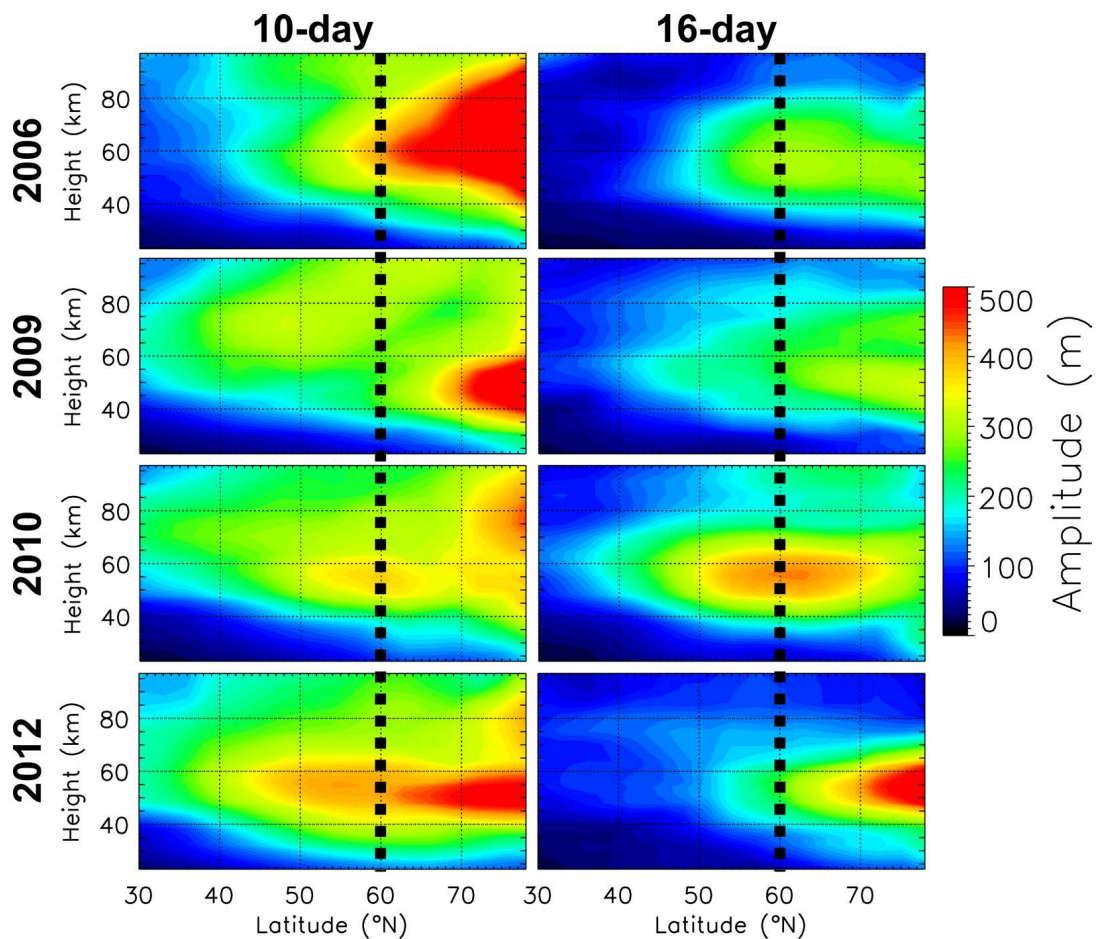


Figure 6.10 Amplitude of the 10-day (period: 8 – 12 d) and 16-day (period: 12 – 20 d) wave from MLS GPH. Amplitude is calculated by the maximum of a sliding window of 40/70 days shifted by one day between day 335 of the previous year and day 60 of the actual year. The dashed line at 60°N is used for the help of orientation.

6.2 Latitudinal variabilities of SSWs

Since the two most dominant transient PWs during SSWs are the 10- and 16-day wave, Figure 6.10 shows the amplitude of the 10- and 16-day wave with wavenumbers between -1 and 1 as a function of latitude and height for the four considered winters from MLS GPH data. The amplitude is calculated as the maximum amplitude of a sliding window of 40 days for the 10-day wave and of 70 days for the 16-day wave at each latitude and height between day 335 of the previous year and day 60 of the actual year. In 2006, the 10- and 16-day wave show an increased activity between the pole and 50°N in the mesosphere and upper stratosphere which is in a good agreement with the latitudinal expansion of the wind reversal during this event. The maximum amplitudes occur at polar latitudes during all winters considered in this study except for the 16-day wave in 2010 where the maximum amplitude occurs at 60°N , i.e., shifted towards the south. However, in 2009 there is a second smaller maximum of the 10-day wave activity at 50°N which reaches down to 30°N . The latitudinally displaced events in 2009, 2010 and 2012 show an increased PW activity between the pole and 30°N . Thus, their PW activity reaches further south than during the normal polar dominated event in 2006.

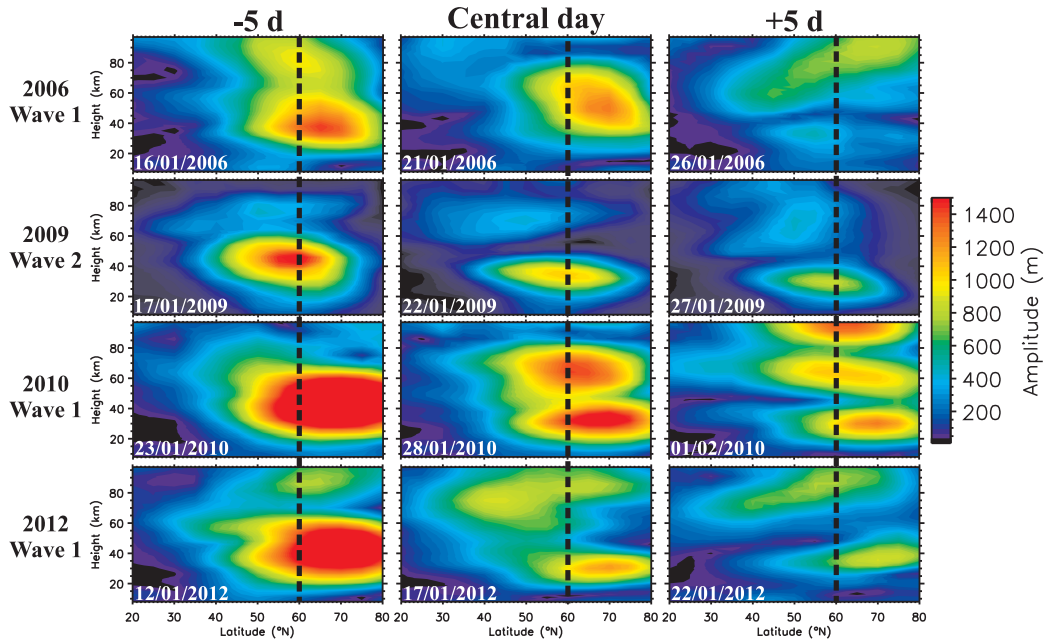


Figure 6.11 Amplitude of the respective dominating stationary wave of SSW events of 2006, 2009, 2010 and 2012 as a function of latitude and height 5 days before, at the central day and 5 days afterwards. GPH data are obtained from MLS. The vertical dashed line at 60°N is used for the help of orientation. This figure is taken from *Matthias et al. (2013)*.

Besides the transient PWs the stationary waves are also important (e.g., *Charlton and Polvani, 2007*). These waves are the PWs with the largest amplitudes. Figure 6.11 shows the latitudinal structure of the amplitude of the stationary wave 1 of the SSWs in 2006, 2010 and 2012 and of the stationary wave 2 for the event in 2009. The

Chapter 6 Characteristics of PWs during Sudden Stratospheric Warmings

selection of the wavenumbers shown here is a result of the type of the corresponding SSW. Thus, for the splitting event in 2009 (e.g., *Manney et al.*, 2009) the dominating stationary wave 2 is shown. The left column of the figure displays the amplitude 5 days before the central day, the middle one at the central day and the right column 5 days after the corresponding central day.

Five days before the central day an increased stationary wave 1 activity occurs from the pole to around 50°N (2006) to 45°N (2010, 2012). However, the stationary wave 2 shows an increased activity between 35°N and 75°N 5 days before the central day in 2009 and not at the pole like in the other events. At the central day, the normal polar dominated SSW in 2006 shows an increased wave activity from pole to mid-latitudes as before. The other three events show a clearly increased activity from the pole down to 30°N , whereas the event in 2009 is not active at the pole. Five days after the central day the amplitudes decrease in every event. All events show an increased wave activity down to 30°N . Nevertheless, the increased activity in the mesosphere at lower latitudes in 2006 is much weaker than at the central day. While in 2009 and 2012 the latitudinal and altitudinal structure of the stationary wave is very similar to the one at the central day, a third maximum occurs above the other two maxima in the upper mesosphere/lower thermosphere in 2010. Summarizing these results, the stationary waves also show a southward extended latitudinal structure during the events in 2009, 2010 and 2012 in comparison to the polar dominated event in 2006. Thus, the continuous westward wind band and the southward extended warmings in the stratosphere are directly connected to an increased transient and stationary PW activity between 30°N and 50°N .

To find an indication about why the zonal wind and temperature changes as well as the PW activity is shifted or extended southward during the latitudinal displaced events, a comparison of the three-dimensional Plumb flux (see section 3.4.4) is conducted between the four SSWs. Thus, Figure 6.12 shows the wave flux activity vectors from MERRA as a function of longitude and latitude averaged between 25 km and 50 km for a 5 day mean after the corresponding central day of each SSW considered in this study. The chosen height range is the area in which the continuous westward wind band occurs during the latitudinal displaced events. The colored background represents the flux divergence, i.e., red colored regions are sources of stationary PW flux and blue colored regions are sinks.

In 2006, the flux vectors indicate a wave 1 structure between the pole and 60°N . South of 60°N the flux vectors are directed equatorward and symmetric around the zero meridian but decrease rapidly below 30°N . The flux divergence shows a strong source of wave flux around the zero meridian between 60°N and 80°N with 2 smaller features between 40°N and 60°N . The sources and sinks alternate between the pole and 20°N with a light eastward shift below 60°N .

The vortex splitting event 2009 shows a wave 2 structure symmetric around 60°N with an equatorward flux around 100°E and 100°W . The sources and sinks of stationary wave flux alternate around 60°N between 180°W and 180°E . At 100°E and 100°W there are additional features of eastward and equatorward alternating sources and sinks.

The stationary flux vector structures of the events in 2010 and 2012 are very similar

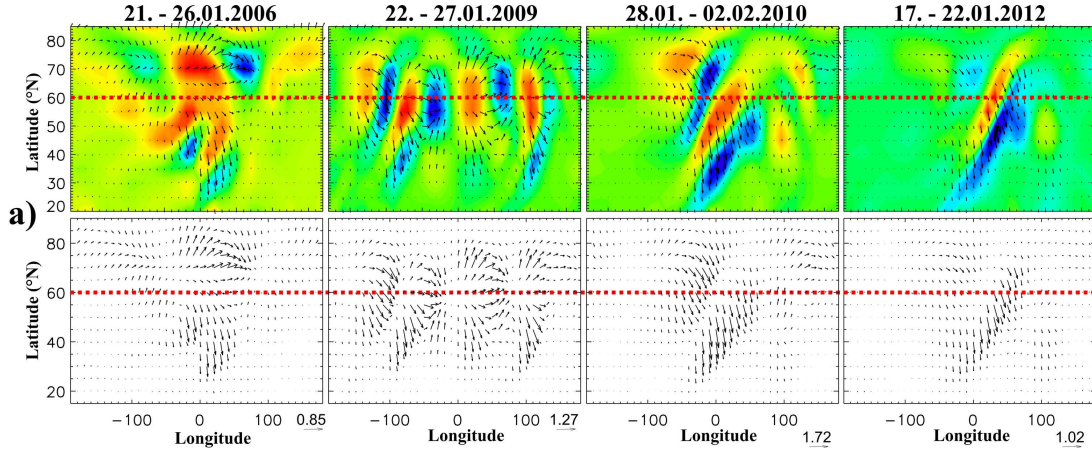


Figure 6.12 Stationary wave activity flux vectors following *Plumb* (1985) of each SSW considered in this study of a five day mean after the central day averaged over the height range between 25 and 50 km, where the colored background represents the flux divergence (red: source, blue: sink); top with flux divergence, bottom without (for a better representation of the arrows). The fluxes were calculated using MERRA data provided by NASA GMAO. This figure is taken from *Matthias et al.* (2013).

whereas the intensity is stronger in 2010 than in 2012. Both events show a two-stripe pattern of equatorward movement between the pole and 20°N. The weaker stripe occurs between 40°N and 80°N and between 100°W and the zero meridian in each case. The stronger one is shifted parallel to the first one and occurs between 70°N and 30°N and between 50°W and 90°E. The sources and sinks of the stationary wave flux alternate within these stripe patterns equatorward with a slight eastward shift. In contrast to the flux pattern of 2006 these fluxes reach from the pole down to 20°N and not only from 60°N to 20°N as in 2006.

This changed wave flux indicates that the reversed westward wind in 2009, 2010 and 2012 is carried south by the stationary wave flux from polar latitudes to 20°N and a continuous westward wind band arises. The equatorward movement of the stationary wave flux during the latitudinal displaced events can also be held responsible for the southward spread of the warming at 20 km and 40 km in 2009, 2010 and 2012 in Figure 6.9. In other words, the changed stationary wave flux during the latitudinal displaced events in 2009, 2010 and 2012 is connected to the southward extended SSW effects. Nevertheless, the reason for this changed wave flux is still unclear.

To find an explanation for the distinctive low temperatures at mid latitudes in the stratosphere before the latitudinal displaced events, the stationary wave flux is considered averaged in the 30 days before the central day. Thus, Figure 6.13 shows the zonally averaged wave flux vectors as a function of latitude and height for a 30 day mean before the corresponding central day of 2006, 2009, 2010 and 2012. Qualitatively there is no visible difference between the stationary wave flux of the polar dominated event in 2006 and the two latitudinal displaced events in 2010 and 2012. They show a strictly poleward flux between 20°N and 40°N which passes into a strictly upward flux

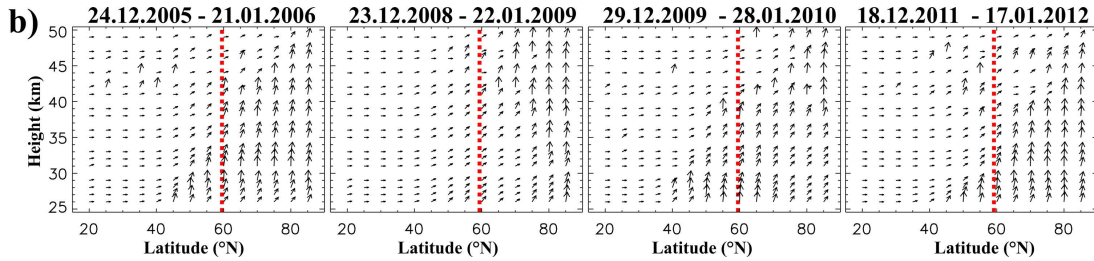


Figure 6.13 Stationary wave activity flux vectors of each SSW considered in this study of a 30 day mean before each corresponding central day zonally averaged and scaled by $(F_\varphi, F_z) \rightarrow (p/p_0)^{(-1/2)}(F_\varphi, 100 \cdot F_z)$, following *Plumb* (1985). The fluxes were calculated using MERRA data provided by NASA GMAO. This figure is taken from *Matthias et al.* (2013).

around the pole. However, the vortex splitting event in 2009 shows differences in the flux pattern compared to the other events. Here, the poleward flux reaches from 20°N to 80°N and therefore passes much later into the upward flux than during the other three events. Thus, the differences between these flux patterns might arise from the different SSW types but not from their latitudinal variabilities. However, the cause of the low stratospheric temperatures before the latitudinally displaced events between 60°N and 30°N is still unclear.

These low temperatures were also observed by *Orsolini et al.* (2010). The aim of their paper was to show that mesospheric H₂O and temperature measurements by the Odin satellite allow to distinguish between the formation of an elevated stratopause and the descent of dry mesospheric air into the polar stratosphere. Among other things, *Orsolini et al.* (2010) show the temperature profile at 1 hPa as a function of latitude and time between July 2001 and July 2009. During the winter months the low polar and mid-latitudinal stratospheric temperatures vary from year to year with respect to their latitudinal extension. In 2009 for example the low temperatures reach as far south as 30°N, but during other years, for example in 2006, low temperatures are present only up to 50°N. Note that there is an altitudinal difference between our study and *Orsolini et al.* (2010) which explains the latitudinal differences in the low temperatures.

From Figure 6.10 and 6.11 it is known that besides the southward extended wind and temperature changes an increased PW activity also occurs between 30°N and 50°N during the latitudinal displaced SSWs. Thus, the question arises: Do the low stratospheric temperatures at mid-low latitudes occur due to the southward extended PW activity or is the PW activity increased at lower latitudes due to the lower temperatures at mid-low latitudes? Since the PWs extend between the pole and lower latitudes, they are influenced by tropical phenomena like the QBO⁴ which was discussed for example by *Chen and Huang* (1999). *Labitzke* (2004) even shows a statistical relation of SSWs

⁴The quasi-biennial oscillation (QBO) is an equatorial variability in the stratosphere which is characterized by downward propagating eastward and westward wind regimes, with a variable period of approximately 28 months.

on the QBO and on the solar cycle. Unfortunately the record warming of 2009 did not fit to this statistical relation (*Labitzke and Kunze, 2009*) which produces new open questions.

Thus it is a good idea to consider in which phase of the QBO each event occurs. The normal polar dominated SSW in 2006 occurs on the westerly phase of the QBO while the other latitudinal displaced events occur on the easterly phase in the high region between 25 and 50 km where the continuous westward wind band occurs (see <http://www.geo.fu-berlin.de/en/met/ag/strat/produkte/qbo>). There is a study of *Naito and Yoden (2006)* which investigates the behavior of the PW activity before and after SSWs in connection with the dominating QBO phase. They found that the dominant zone of the upward and equatorward Eliassen-Palm flux in the lower stratosphere was shifted southward during the eastward phase and poleward during the westward phase of the QBO during a SSW. This result agrees with the above mentioned observation of an equatorward stationary wave flux from the pole down to 20°N between 25 and 50 km during the latitudinal displaced events (see Fig. 6.12). So there might be a connection between the QBO phase and the latitudinal displacement of SSWs. Nevertheless, this requires further investigations which are beyond the scope of this thesis.

6.2.4 Extended discussion

The study of the latitudinal structure of the zonal mean temperature (see Figure 6.9) reveals an unusual latitudinal effect during the SSW of 2012. The stratospheric warming of this event occurs at 20 km between 45°N and 75°N but not at the pole like during the other events considered in this study. To investigate a possible cause of the southward shifted warming in 2012, Figure 6.14 shows the projection of the temperature from MERRA at 20 km in the northern hemisphere five days after the central day of the respective SSWs in 2006, 2009, 2010 and 2012.

The cold part of the global temperature pattern of the events in 2006, 2009 and 2010 is located between 45°W and 90°E but not on the pole. In contrast to this, the cold part of the temperature pattern in 2012 also lies between 45°W and 90°E but is rotated by 90° about the longitudinal axis and is located partly on the pole. This rotation explains the southward shifted warming at 20 km in 2012. The rotation is only observable in the lower stratosphere and not at upper altitudes. The cause of this unusual rotation of the low temperature pattern after the SSW in the lower stratosphere in 2012 is unclear and should be further investigated which is beyond the scope of this thesis.

Figure 6.9 is a firework of information and contains more information than already discussed. Independent from the SSW an equatorward movement of the warming at 40 km is observed, as mentioned before. This agrees with a study of *Shepherd et al. (2007)*. Besides a warming at tropical stratospheric altitudes they found mesospheric variabilities in the tropics which are correlative in time with the SSW. They explain the mesospheric variabilities with an increased PW activity in the mesosphere. Thus, one can assume that the stratospheric tropical warming after each SSW observed here occurs due to the enhanced PW activity not only in the mesosphere but also in the

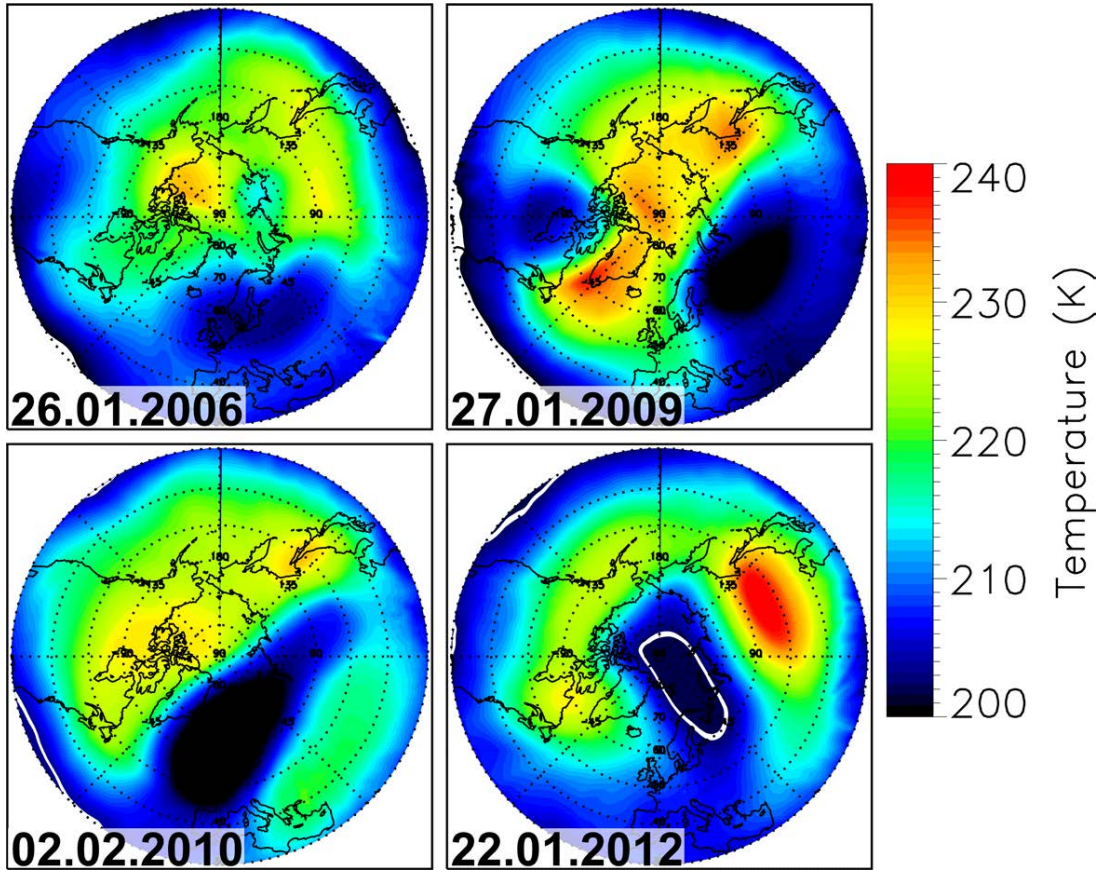


Figure 6.14 Projection of the MERRA temperature data at 20 km over the northern hemisphere 5 days after the central day of the respective SSW. This figure is taken from *Matthias et al.* (2013).

stratosphere at lower latitudes.

Additionally, the zonal mean temperatures in Figure 6.9 show a mid-latitude warming between 40°N and 55°N in the mesosphere at 80 km simultaneous to the polar cooling during the events in 2006, 2010 and 2012. This warming occurs strongly in 2006 and 2012 but much weaker in 2010. It seems that this phenomenon occurs only during vortex displacement events and not during splitting events like in 2009 where the mesosphere shows low temperatures at all latitudes during the SSW. Since this mid-latitude mesospheric warming is unexpected, the mesospheric temperature variation is validated at different locations with MR data in Figure 6.15. The figure shows the day-to-day variability of the relative temperatures in 2009, 2010 and 2012 from MR at Andenes and Juliusruh representative for the eastern hemisphere and at Tavistock (CMOR, (43°N, 81°W)) for the western hemisphere. Note that the year 2006 is missing because the MR at Juliusruh was installed later in 2006. The temperatures are derived from the MR by the combination of the altitude variations in the meteor decay time around the peak of the meteor layer at around 90 km and an empirical

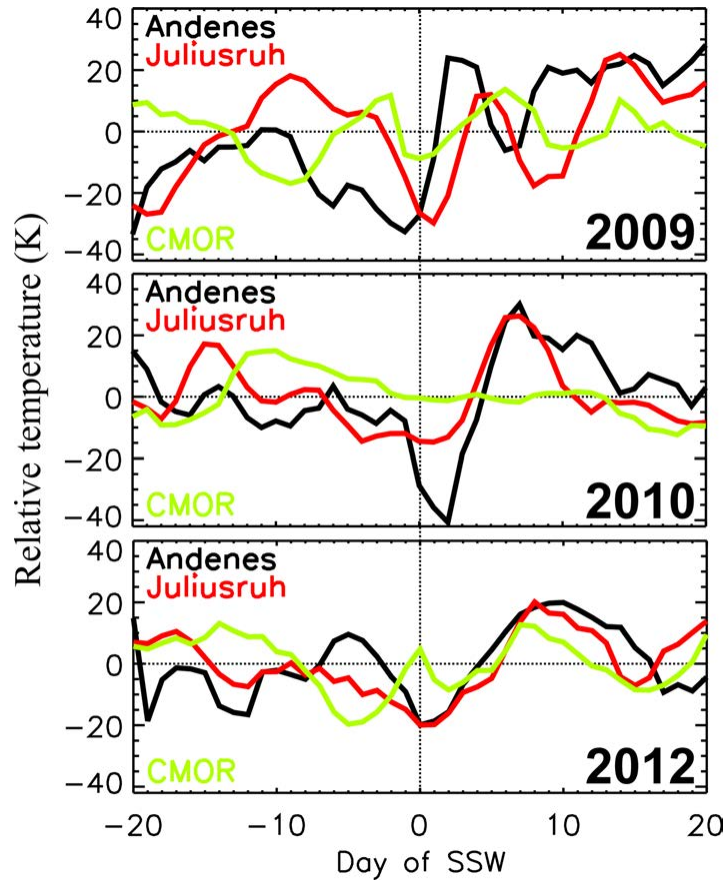


Figure 6.15 Relative temperature from MR at ~ 90 km at Andenes and Juliusruh for the eastern hemisphere and at Tavistock ($(43^{\circ}\text{N}, 81^{\circ}\text{W})$, CMOR) for the western hemisphere centered around the central day of the respective SSW. The black dotted line marks the central day. This figure is taken from *Matthias et al.* (2013).

model of the mean temperature gradient at 90 km (for details see e.g., *Singer et al.*, 2003; *Hocking et al.*, 2004; *Stober et al.*, 2012). Note that MR temperatures depend on the assumption of an empirical temperature gradient model and are therefore not suitable as total values. Thus, the mean temperature is subtracted from the observation period of each temperature profile and only the day-to-day variability is investigated. During the record warming of 2009 all three locations show a temperature decrease around the central day as it was observed in the zonal mean temperatures from MLS in Figure 6.9. The other two events show a cooling in the eastern hemisphere while the western hemisphere shows no significant cooling in connection with the SSW in 2010 and even a warming during the SSW of 2012. Thus, from the local measurements it seems that the mid-latitude warming occurs mainly in the western hemisphere and depends strongly on the longitudinal location.

A more global view of this mid-latitude mesospheric warming is given in Figure 6.16. The figure shows the projection of MLS temperatures at 81 km at the central day for each SSW considered in this study. The white points mark the location of the

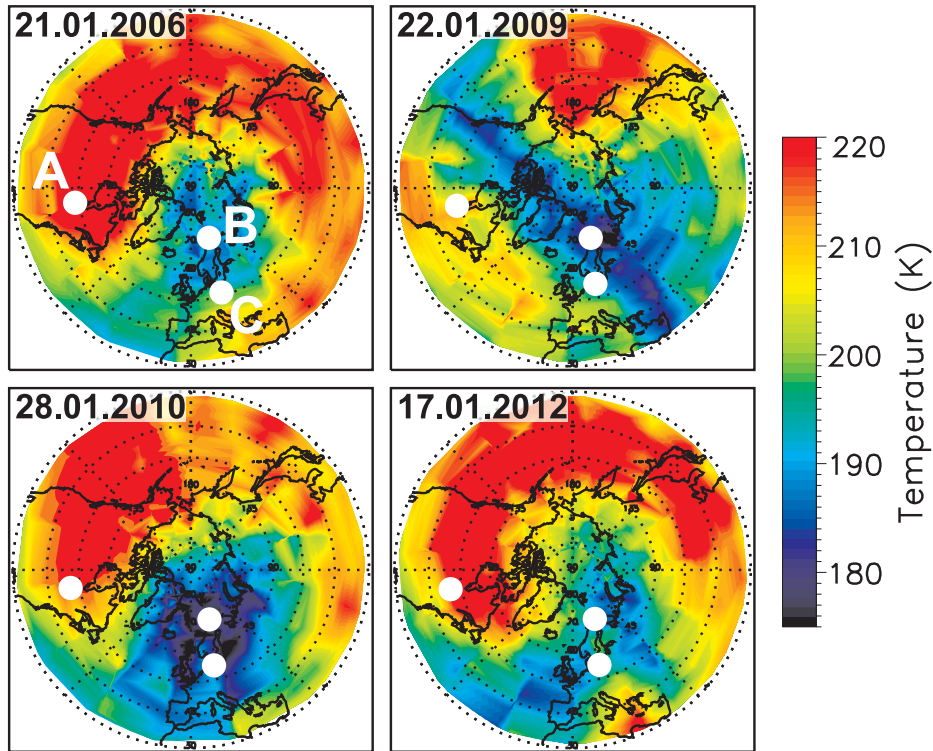


Figure 6.16 Projection of the MLS temperature data at 81 km over the northern hemisphere of the central day of the corresponding SSW. The white points mark the local meteor temperature measurements for A) Tavistock, B) Andenes and C) Juliusruh. This figure is taken from *Matthias et al.* (2013).

MR measurements in Fig. 6.15. Note that the MR temperatures are observed around 90 km while the MLS temperatures are measured at 81 km with a vertical resolution of 10 km. Thus, there is an altitudinal discrepancy that should be considered.

During all SSWs Andenes and Juliusruh are located on the cold part of the global temperature pattern and thus the SSW effects are strongest there. In contrast, the CMOR radar is located at the much warmer part of the temperature pattern during the events in 2006, 2010 and 2012. Only during the vortex splitting event in 2009, CMOR lies between the warm and the cold part of the temperature pattern. These longitudinal differences explain, why the local measurements at Andenes and Juliusruh do not show the mid-latitude warming in the mesosphere. Thus, there is a longitudinal variability of SSW effects that should be considered in the comparison of local measurements among each other and among zonal mean values.

The cause of this mid-latitude mesospheric warming could be the increased stationary wave 1 activity (cf. Figure 6.11) in the mesosphere around the central day of the SSWs 2006 and 2012 and after the central day in 2010.

These last two figures show how important it is to classify local measurements into the global context. For local measurements it is important to know the phases of the PWs especially if one wants to compare observations from different hemispheres dur-

6.3 Longitudinal variability of SSWs

ing winter months. The next section will intensify the discussion on the longitudinal variability of SSWs to raise the awareness for the differences of local measurements and zonal mean values.

Summarizing the results of this section, a comparison was conducted between the normal polar dominated SSW in 2006 and the latitudinal displaced events in 2009, 2010 and 2012. These displaced events show a continuous westward wind band from the pole down to lower latitudes as well as a southward extended stratospheric warming. These changes occur due to the changed equatorward stationary wave flux from the pole down to 30°N compared to the normal event in 2006.

The low mid-latitude stratospheric temperatures before the latitudinally displaced warmings are not in connection with a changed stationary wave flux even though an increased transient and stationary PW activity is observed between 30°N and 50°N around these SSWs compared to the one in 2006. Therefore, an indication was found for a connection of the occurrence of latitudinal displaced SSWs and the QBO phase. Other effects which occur besides these latitudinal differences are an equatorward movement of the stratospheric warming and a downward progression of the zonal wind and temperature changes. The investigation of a mid-latitude mesospheric warming even reveals a longitudinal variability of SSW effects which should be considered by classifying local measurements into the global context and which is discussed in the following section.

6.3 Longitudinal variability of SSWs

Besides latitudinal variabilities the previous section also indicated longitudinal variations of wind and temperature changes during SSWs. It is clear that the strong stationary wave activity during winter months (see chapter 4) divides the northern hemisphere, for example, into cold and warm parts. Thus, for the comparison of different local measurements the position of each location with respect to the global pattern needs to be considered. This section is intended to motivate the investigation of the longitudinal variability of SSW effects and its connection to PWs. The longitudinal variability during SSWs is shown using the example of the major SSW in 2010 with local radar measurements from four different locations and global assimilated model data from MERRA concentrating on the zonal wind variations.

To demonstrate how diverse local measurements during winter months can be, Figure 6.17 shows the zonal wind at mid- and polar latitudes. Juliusruh and Andenes are representative for the eastern hemisphere and Eureka and Saskatoon are representative for the western hemisphere. The data are derived from the respective radar in the mesosphere at 85 km and from MERRA together with the zonal mean in the stratosphere at 32 km.

Before the central day, Saskatoon and Juliusruh show a similar zonal wind behavior in the mesosphere. When there is a maximum of the zonal wind at Juliusruh, there is a maximum at Saskatoon at almost the same time. After the central day the minima

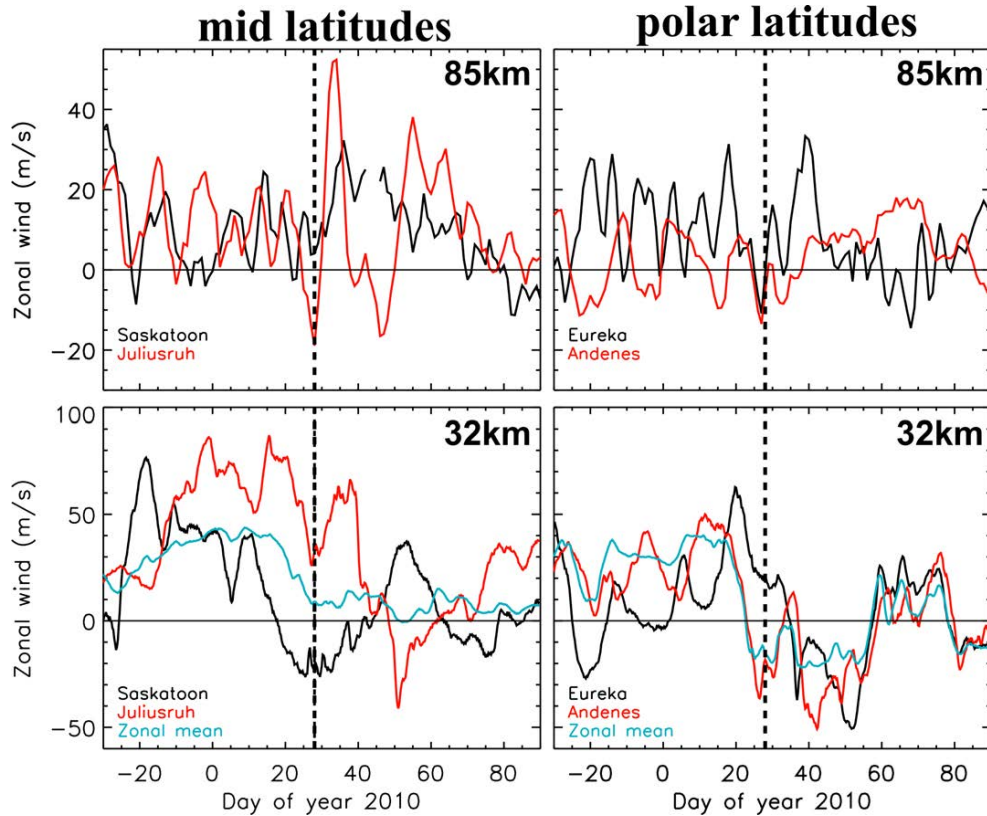


Figure 6.17 Zonal wind at Saskatoon and Juliusruh (left) and at Eureka and Andenes (right) during the winter of 2009/10. The dashed line marks the central day of the major SSW in 2010. Top: The zonal wind at 85 km is derived from the respective radar measurements. The diurnal, semidiurnal and terdiurnal tides are removed. Bottom: The zonal wind and the zonal mean zonal wind, averaged between 50°N and 60°N for the mid-latitudes and between 70°N and 80°N for the polar latitudes, are derived from MERRA at 32 km.

and maxima of the zonal wind at Juliusruh are much more pronounced than those at Saskatoon and their behavior is sometimes the opposite. In the stratosphere Juliusruh and Saskatoon differ strongly. The zonal wind at Juliusruh is much stronger and shows a different behavior than that in Saskatoon. Additionally, the zonal mean zonal wind lies mostly between Saskatoon and Juliusruh but from time to time also shows a different behavior at both locations. The zonal winds at polar latitudes in the eastern and western hemisphere differ strongly from each other in the mesosphere and stratosphere. The zonal wind behavior of Eureka is the opposite of Andenes. When Eureka has a maximum in the zonal wind, Andenes has a minimum. Even the zonal mean zonal wind in the stratosphere shows large differences to both Andenes and Saskatoon. Only after the central day, where normal winter conditions dominate, the zonal wind at both locations and the zonal mean zonal wind show a very similar behavior. The longitudinal variability of the mesospheric wind behavior was also studied by *Hoffmann et al.* (2007). They compared the wind at Andenes (69°N, 16°E) with Resolute

Bay (75°N, 95°W) during the winter of 2005/06 and with Poker Flat (65°N, 147°W) during the winter of 1998/99. They found distinctive differences in the meridional wind behavior during both winters but a similar zonal wind behavior of both stations around the major warmings. *Manson et al.* (2011) also showed distinctive longitudinal differences in the monthly mean zonal wind behavior between Eureka (80°N, 85°W) and Svalbard (78°N, 16°E) between 2006 and 2009.

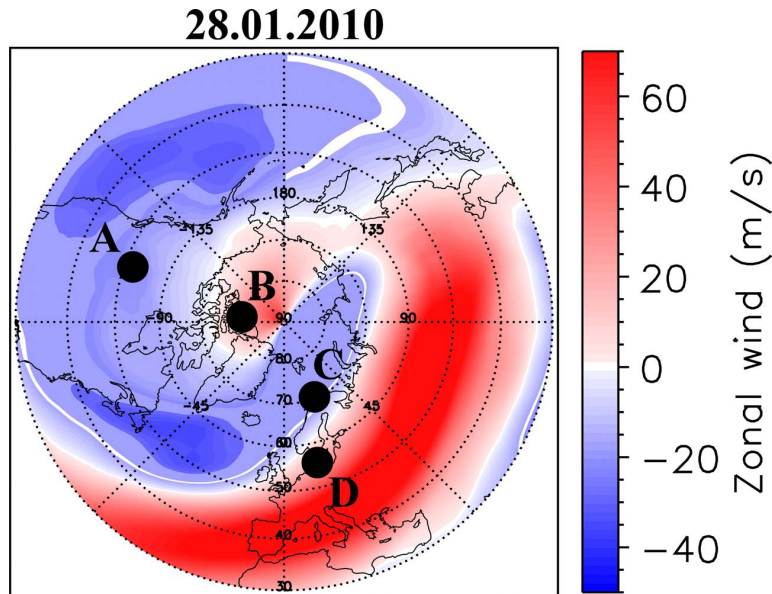


Figure 6.18 Projection of the zonal wind at 32 km from MERRA on the northern hemisphere for January 28, 2010. The black dots mark the location of the radar stations: A) Saskatoon, B) Eureka, C) Andenes and D) Juliusruh.

The longitudinal differences in the zonal wind occur due to the PW activity and the position of the polar vortex. To have a more global view of the zonal wind, Figure 6.18 shows the projection of the zonal wind on the northern hemisphere from MERRA at 32 km on January 28, 2010, the central day of the major warming. The dots shown in Figure 6.17 mark the location of each radar. The zonal wind curls around the north pole like a helix with an eastward and westward wind arm. Thus, Saskatoon and Andenes are located within the westward arm while Eureka and Juliusruh are located still within the eastward part of the helix. Between 70°N and 80°N the westward wind dominates which was also shown in Figure 6.17. Between 50°N and 60°N the eastward and westward winds are uniformly distributed. However, we note that the eastward wind is stronger.

This helix structure was also observed by *Charlton and Polvani* (2007) in GPH data from NCEP–NCAR during the vortex displacement event in 1984 and in the zonal wind by *Manson et al.* (2011) for January 2008 from the CMAM–DAS⁵ data in combination with longitudinal differences in the zonal wind between Eureka and Svalbard, as

⁵CMAM – Data Assimilation System (CMAM–DAS): The first data assimilated version of the Canadian Middle Atmosphere Model (for details see *Polavarapu et al.*, 2005)

mentioned before. *Manson et al.* (2011) explain the longitudinal differences with the occurrence of a SSW but they do not go into detail why they occur.

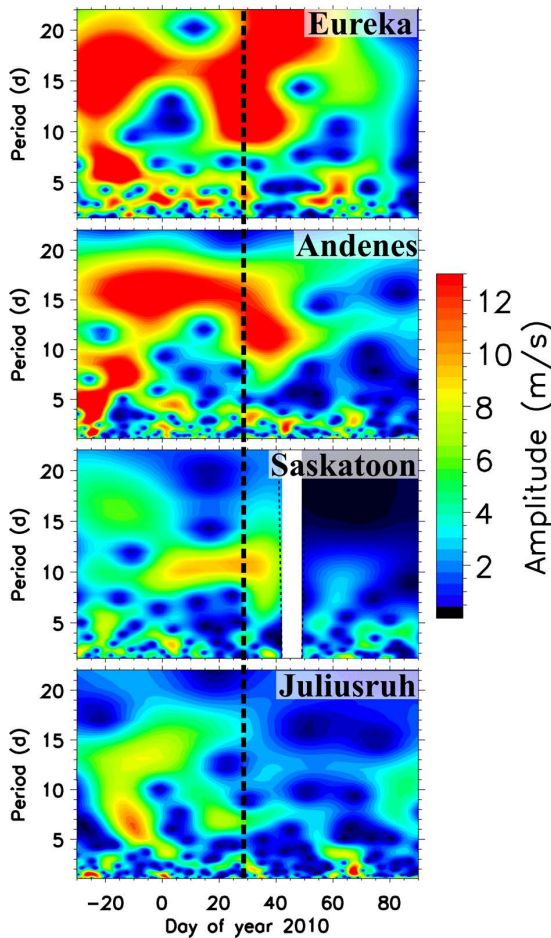


Figure 6.19 Wavelet spectrum for the winter of 2009/10 from December to March at 85 km from Eureka, Andenes, Saskatoon and Juliusruh. Data are derived from meridional winds from the respective radar. The dashed line marks the central day of the SSW in 2010.

Figure 6.17 indicated a distinctively different zonal wind behavior between the eastern and western hemisphere especially in the polar latitudes. In what way these differences also occur in the PW spectrum is shown in Figure 6.19. This figure shows the Wavelet spectrum of the meridional wind from Eureka, Andenes, Saskatoon and Juliusruh at 85 km of the winter of 2009/10. At polar latitudes a strong 16-day wave dominates before the central day and passes over to a 10-day wave around the central day. A detailed investigation shows a slightly temporally shifted activity at Andenes compared to Eureka. Especially the smaller waves with periods between two and eight days do not occur at the same time at both locations.

Before the central day, the 16-day wave reveals a much smaller amplitude at mid latitudes as compared to polar latitudes. However, the amplitude at Juliusruh is larger than at Saskatoon. The 10-day wave behaves in the opposite way. It is stronger at Saskatoon than at Juliusruh. It occurs at Saskatoon from the beginning of December until the SSW starts, whereas the temporal occurrence at Juliusruh is much shorter and even shows an interruption.

Manson et al. (2006) compared the occurrence of the 16-day wave during the winter of 2001/02 at 5 different locations (Saskatoon (52°N, 107°E), Wakkanai (45°N, 141°E), London (43°N, 81°W), Plattville (40°N, 105°W) and Yamagawa (31°N, 130°E)). They found a longitudinal variability especially between Wakkanai and Plattville, which are on the opposite site of the northern hemisphere to each other.

Even though one would assume that the PW activity is approximately the same all

around a latitude band, Figure 6.19 also indicates differences within one band. Therefore, Figure 6.20 shows the fitted zonal wind from Eureka and Andenes for the 16-day wave and from Saskatoon and Juliusruh for the 10-day wave of the winter of 2009/10. It is striking that the amplitude of the 10- and 16-day wave is larger in the eastern hemisphere than in the western hemisphere. This was also shown to be an example for a PW depending on longitude in Figure 2.2 on page 5 from MLS temperature data. At mid and polar latitudes a phase shift of the 10- and 16-day wave occurs which is not surprising due to the longitudinal separation of the locations.

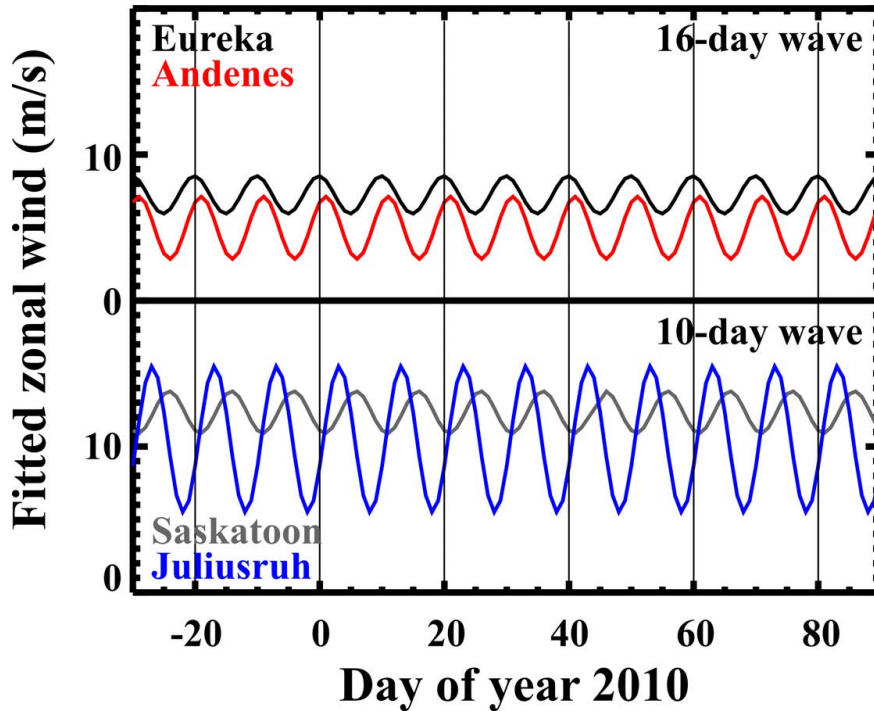


Figure 6.20 Fitted zonal wind for the 16-day wave at Andenes and Eureka and for the 10-day wave for Juliusruh and Saskatoon at 85 km in winter of 2009/10. Data are derived from the MR or MF radar, respectively.

This brief discussion of the longitudinal variability of SSWs shows that there are local differences not only during SSWs but also during the whole winter. These differences occur due to the PW activity and the different PW phase relative to the wave. Thus, comparisons of winds and temperatures at different locations should always take the PW activity as well as the phases of these waves into account. Additionally, local phenomena like gravity waves influence the local measurement. To avoid those local effects, one can also use the sectoral mean as hinted by *Matthias et al.* (2012a). In the previous section (sec. 6.2) a continuous westward wind band was found in the zonal mean zonal wind. Figure 6.18 on page 65 shows that this wind band did not occur at all latitudes and longitudes in 2010, hence also the comparison of local measurements with zonal mean values should be done carefully.

Chapter 6 Characteristics of PWs during Sudden Stratospheric Warmings

This chapter showed the characteristics of winds, temperatures and PWs during the most prominent and impressive vertical coupling process in the middle atmosphere, the SSW. Other examples for coupling processes are the spring and fall transition where the wind reverses from winterly eastward to summerly westward winds in the middle atmosphere. During some fall transitions a small warming occurs in the stratosphere with a simultaneous cooling in the mesosphere. Additionally, the zonal wind weakens at the same time in the middle atmosphere. This coupling process, which acts like a mini SSW, is called the "Hiccup". In the next chapter the characteristics of the Hiccup as well as the role of PWs during the Hiccup is investigated. Additionally, a comparison of Hiccups with the SSWs is conducted to illustrate the differences in the generation processes.

Chapter 7 Characteristics of the “Hiccup” of the fall transition¹

The spring and fall transitions are expected to reveal changes in the middle atmosphere dynamics since the mean flow has to reverse from winterly eastward to summerly westward wind or vice versa. For a long time the transitions have been considered as a smooth process between summer and winter or respectively vice versa. *Shepherd et al.* (1999) were the first to observe large perturbations of a few days during the springtime transition of 1992 and 1993. These perturbations last for only a few days in the local measurements of temperature and airglow emissions. However, in WINDII² observations on the UARS³ satellite, the perturbations are seen for about two weeks in wind and airglow emission rates. In a personal discussion, Theodore G. Shepherd⁴ named this phenomenon the “Hiccup”, which will be used in the following. The Hiccup occurs during spring and fall transitions but appears more clearly during the fall transition due to a more stable atmosphere during summer. Therefore, this chapter describes the wind and temperature characteristics of a Hiccup taking the example of the fall 2006. A composite analysis of winds, temperatures and PW activity during the Hiccup is following. Finally, the characteristics of the Hiccup are compared with that of the SSW where the similarities and differences are worked out for both coupling processes.

7.1 The Hiccup during fall 2006

The Hiccup during fall 2006 is a particularly strong and nice event, why it was exemplarily chosen to show how Hiccups behave temporally, altitudinally and globally. To start, Figure 7.1 shows the seasonal variation of the zonal mean temperature derived from MLS in the stratosphere at 32 km (red) and in the mesosphere at 86 km (black) at 70°N during 2006. During the fall transition a large perturbation of about 10 K occurs with a warming in the stratosphere and a cooling in the mesosphere

¹This section was accepted for publication in the Proceedings of the 13th International Workshop on Technical and Scientific Aspects of MST Radar (MST 13), (*Matthias et al.*, 2012b). It has been co-authored by Theodore G. Shepherd at the University of Reading, Peter Hoffmann at the Leibniz Institute of Atmospheric Physics and Markus Rapp at Deutsches Zentrum für Luft und Raumfahrt in Oberpfaffenhofen.

²WIND Imaging Interferometer (WINDII); for details see *Shepherd et al.* (1993)

³Upper Atmosphere Research Satellite (UARS)

⁴formerly at the Department of Physics at the University of Toronto, CA; now at the Department of Meteorology at the University of Reading, UK

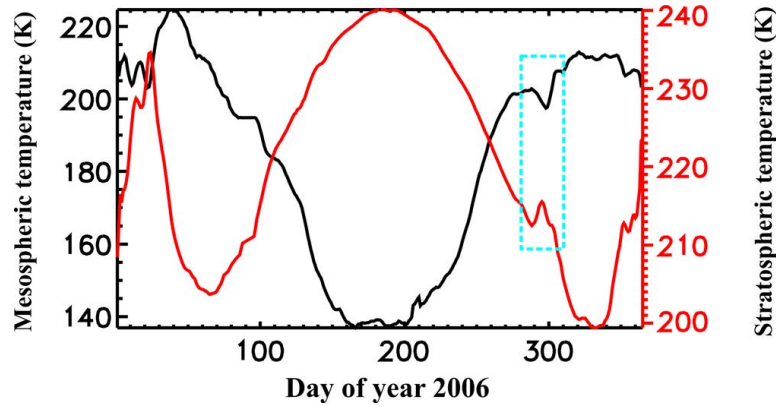


Figure 7.1 Seasonal variation of the zonal mean temperature at 86 km (black) and 32 km (red) at 70°N from MLS for 2006. This Figure is taken from *Matthias et al. (2012b)*.

(dashed rectangle), called the Hiccup. This behavior is similar to that during SSWs but with a distinctively smaller magnitude.

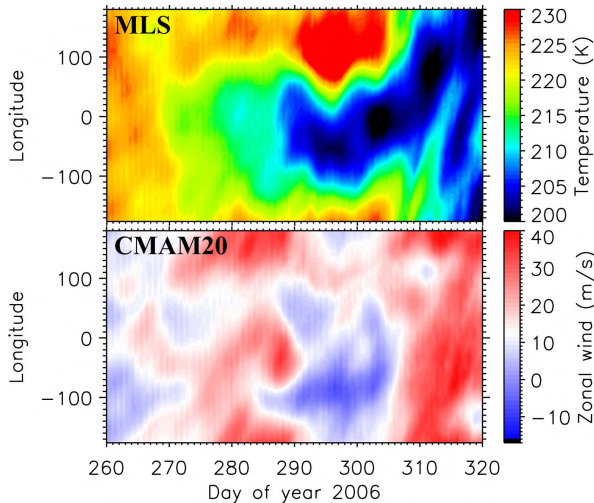


Figure 7.2 Longitude-time cross-section of the temperature from MLS (top) and the zonal wind from CMAM20 (bottom) averaged between 65°N and 75°N at 32 km during the fall transition of 2006.

The longitudinal behavior of the Hiccup in the temperature and zonal wind at 32 km in a 10° latitude band centered around 70°N is shown in Figure 7.2. The data are respectively derived from MLS and CMAM20⁵. The longitude-time cross-section of the temperature from MLS measurements shows a temporal development of a cooling during the fall transition which is interrupted by a warming in the eastern hemisphere (0 – 180°) between day 290 and 310. Note, that the longitudinal structure around the Hiccup indicates a wave 1 structure similar to the SSW which will be discussed later. A similar behavior is shown in the zonal wind from CMAM20 data. At the beginning of the fall, between day 260 and 270,

the wind reverses from westward to eastward and becomes stronger with time. This increase of the eastward wind is interrupted by a weakening of the zonal wind in the eastern and western hemisphere between day 287 and 310 and thus a little earlier than the temperature changes.

⁵The CMAM20 data are used due to the collaboration with Theodore Shepherd, formerly at the University of Toronto.

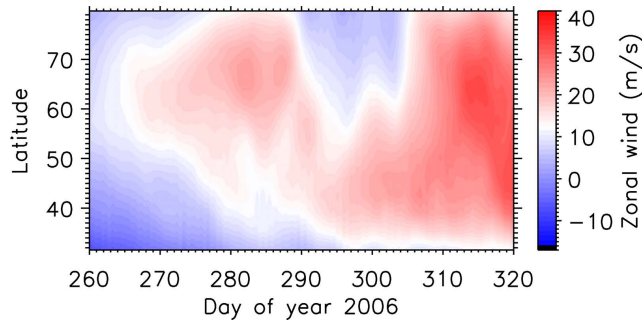


Figure 7.3 Latitude-time cross-section of the zonal mean zonal wind from CMAM20 at 32 km of the fall 2006. This Figure is taken from *Matthias et al.* (2012b).

former observations of *Shepherd et al.* (1999) and *Taylor et al.* (2001) in the MLT region show perturbations of the fall transition at mid-latitudes while TIME-GCM⁶ model data of *Liu et al.* (2001) indicate also a perturbation in the mesosphere and thermosphere at polar latitudes. These results agree with the here observed latitudinal behavior.

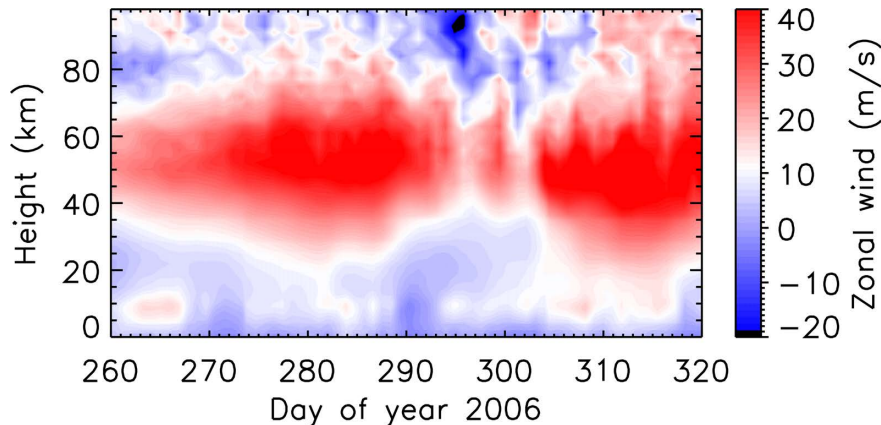


Figure 7.4 Altitude-time cross-section of the zonal mean zonal wind from CMAM20 averaged between 65°N and 75°N during the fall 2006.

The height variation of the Hiccup is finally shown in Figure 7.4 for the zonal mean zonal wind from CMAM20 averaged again between 65°N and 75°N. It seems that the wind weakening starts around day 287 in the troposphere and propagates upward into the mesosphere within a few days whereas the weakening is small between 40 and 60 km compared to the troposphere and mesosphere. Earlier studies of *Shepherd et al.* (1999),

⁶TIME-GCM = Thermosphere-Ionosphere-Mesosphere-Electrodynamics General Circulation Model

Taylor et al. (2001) and *Liu et al.* (2001) described the fall transition perturbation only as a mesospheric and thermospheric phenomenon induced by the altitude range of their measurement or model types.

7.2 Composite analysis of the temporal development of the Hiccup

To study the average behavior of Hiccups, the events are categorized into minor and major ones, similar to SSWs. A major Hiccup can be imagined like the event in the fall 2006 where the temperature in the stratosphere and mesosphere shows a small maximum and minimum during the fall transition in form of a peak (cf. Figure 7.1). Minor Hiccups are shaped like a small step (not shown), i.e., the temperature decrease in the stratosphere pauses for a few days on a certain level before decreasing further. For the composite analysis of the Hiccup only the major events are chosen due to the larger effects compared to the minor ones. Similar to the composite analysis of SSWs in section 6.1 a reference day is needed. Here the reference day is called the Hiccup onset day and is defined as follows: The Hiccup onset day is the first day where at 10 hPa and around 70°N

- i. the zonal mean zonal wind is larger than 15 m/s,
- ii. $du/dt < 0$ for at least three days and
- iii. the mean zonal wind increases after the Hiccup again.

As an example, Figure 7.5 shows the zonal mean zonal wind averaged between 65°N and 75°N and its temporal deviation from CMAM20 during the fall transition of 2006. The black dashed line marks the Hiccup onset day. After day 287 (Hiccup onset day) the zonal wind decreases for ~ 10 days before it increases again. Note that the first condition is chosen due to the established requirement that a stationary wave may form if the zonal wind is larger than 15 m/s (*Nash et al.*, 1996).

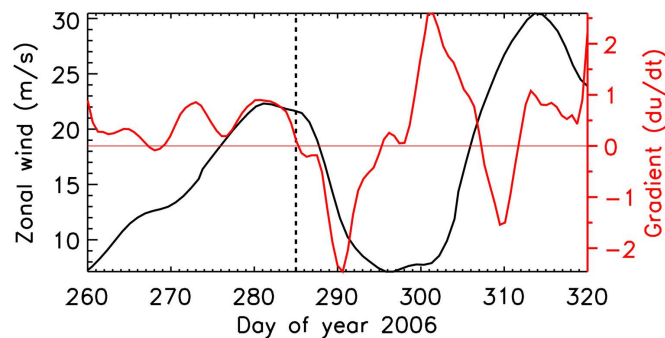


Figure 7.5 Zonal mean zonal wind from CMAM20 averaged between 65°N and 75°N (black) and its deviation du/dt (red) during the fall transition of 2006.

7.2 Composite analysis of the temporal development of the Hiccup

From the 20 years of CMAM20 data (1989 – 2009), nine events are categorized as major Hiccups: 1991, 1994, 1996, 1998, 2003, 2004, 2005, 2006, and 2009. These events have a Hiccup onset day on day 301, 305, 295, 295, 275, 286, 286, 287 and 278 of the respective year whereby the Hiccup starts between the end of September and the beginning of October. These events are in the following used for a composite analysis of the zonal wind, temperature and stationary wave activity.

Figure 7.6 shows the composite of the zonal mean zonal wind (left) and temperature anomaly (right) relative to the Hiccup. The zonal wind weakening seems to start in the troposphere and propagates upward with time into the mesosphere. Additionally the composite of the zonal wind deviation shows an increase of the zonal wind before the Hiccup and a vertical wave structure around the Hiccup onset day. The temperature changes seem to lag the wind changes by a few days in the stratosphere. Similar to the zonal wind, the temperature deviation shows a cooling before the Hiccup onset day in the stratosphere and a warming in the troposphere simultaneous to the wind weakening right after the Hiccup onset day. The temperature anomalies show similar to the zonal wind a vertical wave structure around the Hiccup onset day and an upward propagating wave with time afterwards in the stratosphere and mesosphere.

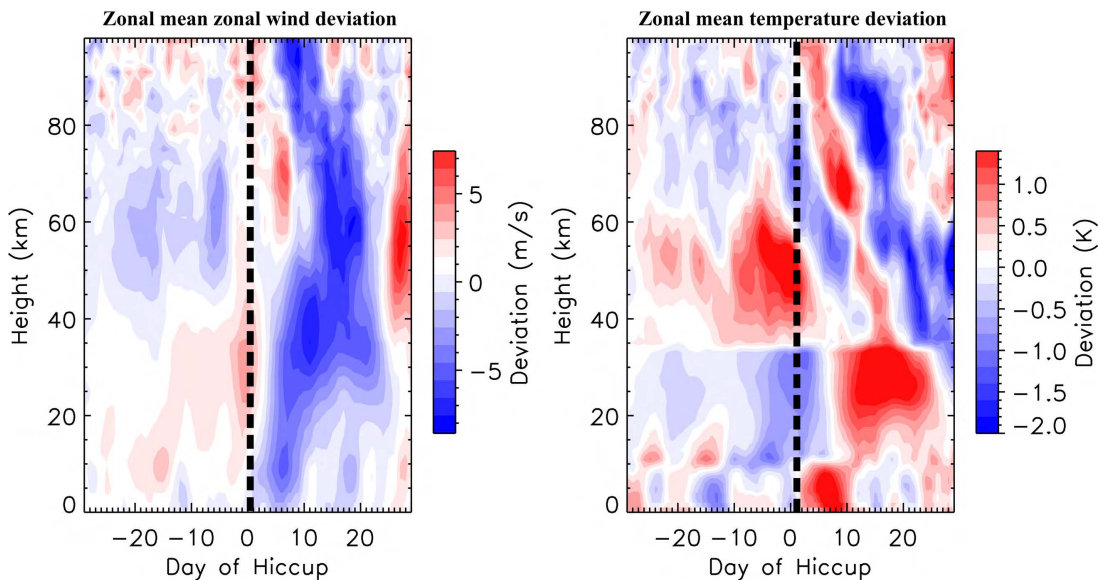


Figure 7.6 Composite of the zonal mean zonal wind (left) and temperature anomaly (right) averaged between 65°N and 75°N from CMAM20.

The zonal wind and temperature changes are assumed to be induced by the sudden turn-on of the PW propagation into the stratosphere during the fall transition which can then be communicated up to the MLT region through filtering of gravity wave propagation, as in the case of SSWs (*Holton, 1983*). This assumption is in agreement with *Liu et al. (2001)* who assumed, that the large temperature variabilities in the mesosphere and thermosphere are caused by fast changes of phase and amplitude of PWs due to the interaction of wave transience and the transition of the mean flow. An

Chapter 7 Characteristics of the “Hiccup” of the fall transition

indication of a wave 1 structure was already found in Figure 7.2. Therefore, Figure 7.7 shows the composite of the stationary wave 1 activity obtained from the zonal wind at 70°N from CMAM20 data. The stationary wave starts its activity shortly before the Hiccup onset day between 50 and 60 km, has a small minimum right after the Hiccup onset day, and increases afterwards with time. This result confirms the assumption that the sudden turn-on of the PW activity is responsible for the Hiccup of the fall transition and is in a good agreement with model results of *Liu et al.* (2001) who observed a rapid increase of the PW 1 in the mesosphere around the fall equinox.

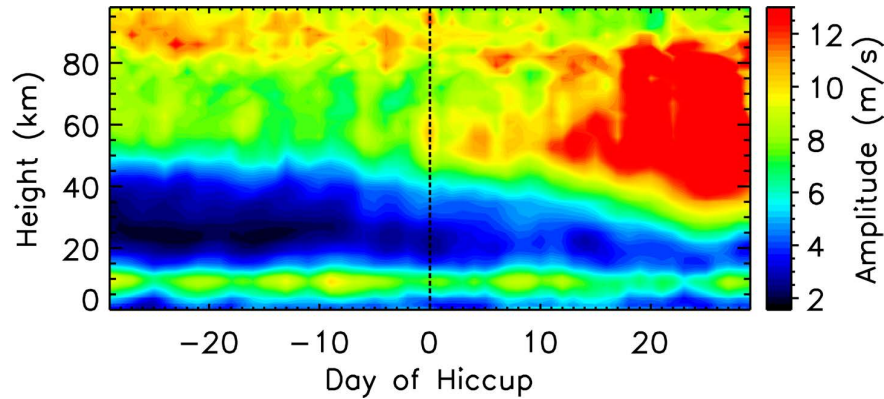


Figure 7.7 Composite of the stationary wave 1 activity at 70°N of the zonal wind from CMAM20. This Figure is taken from *Matthias et al.* (2012b).

During the study of the Hiccup the idea came up to use the free-running version of CMAM for the composite analysis instead of CMAM20 data to have a larger number of events. Unfortunately, this data set only barely shows the Hiccup during the fall transition (not shown). The only difference between the free-running model CMAM and the nudged version CMAM20 is the data assimilation in the troposphere and stratosphere. This confirms the assumption that the Hiccup is excited in the troposphere and then propagates upwards into the mesosphere.

Summarizing, the Hiccup appears like a small SSW with a warming in the stratosphere and a cooling in the mesosphere at polar and mid latitudes. The zonal wind weakening seems to propagate upward from the troposphere into the mesosphere whereas a zonal wind increase is observed before the Hiccup. The temperature changes seem to lag the wind changes by a few days in the stratosphere whereas an increase of the temperature occurs in the troposphere simultaneously with the wind weakening. The assumption that the Hiccups occur due to sudden start of the PW activity is confirmed by sudden turn-on of starting stationary wave 1 activity shortly before the Hiccup onset day.

The Hiccup as well as the SSW are coupling processes which occur due to the interaction of PWs with the mean flow. As mentioned before the Hiccup shows similarities with the SSW albeit the Hiccup seems to propagate upward while the pattern of the

SSW seems to propagate downward. To identify the similarities and differences of these two coupling processes the next section 7.3 compares the SSW with the Hiccup regarding their corresponding morphologies of winds, temperatures and PW behavior.

7.3 Hiccup vs. SSW

In this thesis two coupling processes were considered where PWs play an important role in the generation process. First of all, the most impressive coupling process, the SSW, occurs during winter and is known for its effects on the temperature and wind regime in the middle atmosphere. The second one, the Hiccup, occurs during the transition periods and shows very similar effects as the SSW, but with a distinctively smaller magnitude. This section compares the characteristics of SSWs with that of the Hiccup and highlights the similarities and differences between these two coupling processes.

Both coupling processes are characterized by a warming in the stratosphere and a simultaneous cooling in the mesosphere. Similar as during SSWs the zonal mean zonal wind weakens during the Hiccup. However, this effect occurs simultaneously with the temperature changes during the SSW while the temperature changes seem to lag the wind changes by a few days during the Hiccup. Additionally, the wind weakening occurs during the SSW mostly in the middle atmosphere while it appears also in the troposphere during the Hiccup (cf. Figure 7.4 and 6.2 page 43). Before the Hiccup, a zonal mean zonal wind increase and a temperature decrease occurs in the stratosphere (see Figure 7.6) which is not observed before the SSW (see Figure 6.2 page 43). Considering the propagation direction of both processes another difference occurs. While the effects of a SSW propagate downward, they seem to propagate upward from the troposphere into the mesosphere during the Hiccup. The latitudinal extension of both, the SSW (polar dominated) and the Hiccup, is from the pole down to mid latitudes (cf. Figure 7.3 and 6.8 (top) page 50). Thus, while the effects and their extension of a SSW and a Hiccup are very similar, the background processes seem to be different. The reason for the occurrence of both coupling processes is very similar at first sight. They occur due to the interaction of PWs with the mean flow. Nevertheless, while during a SSW the PW activity is very high (cf. Figure 6.4 page 45 and 6.6 page 46), it is low and only starts around the Hiccup (see Figure 7.7 and 4.2 page 28) compared to the SSW. Therefore, the generation processes are also different. While for SSWs it is assumed and generally accepted that a high transient PW activity is responsible for the SSW, the Hiccup is assumed to occur due to the sudden turn-on of the PW activity.

All these similarities and differences between the SSW and the Hiccup are summarized in Table 7.1 (page 76). The last column of the table shows that the SSW and the Hiccup have far more differences than similarities. Even if they are very similar regarding the occurring effects in the middle atmosphere their generation processes seem to be different although both are generated by the interaction of PWs with the mean flow.

	SSW	Hiccup	similarities ✓ differences ✗
warming/cooling in stratos-/mesosphere	✓	✓	✓
temperature vs. wind changes	simultaneously	temperature later than wind in stratosphere	✗
... before process in stratosphere	no abnormality	temperature decrease, wind increase	✗
altitudinal extension	middle atmosphere	troposphere to mesosphere	✗
propagation direction	downward	upward	✗
latitudinal extension	polar to mid	polar to mid	✓
PW activity	high	low (starting)	✗
(assumed) occurring reason	high transient PW activity	sudden turning on of PW activity	✗

Table 7.1 Comparison of the characteristics of SSWs with the Hiccup.

7.3 Hiccup vs. SSW

Summarizing, the Hiccup of the fall transition is a vertical coupling process with effects similar to that of a SSW but with smaller magnitudes. A comparison of the wind, temperature and PW behavior between SSWs and the Hiccup indicates that different dynamical processes underlie both coupling processes. The assumption that the Hiccup is induced by the sudden turn-on of the PW activity was confirmed in this study. However, the generation mechanism of the Hiccup is still not completely understood. To design a model for the Hiccup, like *Matsuno* (1971) did for the SSWs, further investigations especially of the transient and stationary wave activity in the troposphere and middle atmosphere are necessary.

Chapter 8 Summary and Outlook

To understand the role of PWs in vertical coupling processes, the main aim of this thesis was to study the altitudinal and latitudinal behavior of PWs during SSWs as well as to study the dynamics during the Hiccup of the fall transition in the middle atmosphere. This was done by combining local high-resolution radar measurements with global satellite observations and assimilated model data.

By composite analysis of the zonal wind at Andenes (69°N, 16°E) and of the PW activity at 69°N, the average behavior of wind and waves during major SSWs between 1998 and 2013 were considered. The zonal wind shows an earlier onset of the wind reversal in the mesosphere than in the stratosphere by four days which was confirmed by a cross-correlation between 84 and 32 km. The two dominating transient PWs during SSWs show a strong 10-day wave in the stratosphere and mesosphere around the central day where at the same time the elsewhere strong 16-day wave has a minimum in the stratosphere. A comparison with the composite of minor warmings indicates that major SSWs develop only if the 10-day wave is strong in the stratosphere **and** in the mesosphere. The stationary wave 1 is highly active in the stratosphere and mesosphere until the central day and decreases rapidly afterwards while the stationary wave 2 is much weaker and has a maximum at the central day in the stratosphere.

Normally, SSWs are strongest at the pole, become weaker towards the south and typically vanish at mid-latitudes. However, within this study, three southward extended or shifted SSWs were found in 2009, 2010 and 2012. These latitudinally displaced SSWs were compared with the normal polar dominated SSW in 2006, which was chosen as a representative case, with respect to the global zonal wind, temperature and PW behavior. The latitudinally displaced events show a continuous westward wind band from the pole down to the lower latitudes and a southward extended or shifted warming in the stratosphere in contrast to the normal event. These southward extended effects were linked to a changed equatorward stationary wave flux (Plumb flux) from the pole down to 30°N around the central day which is not present during the normal polar dominated event. Additionally, a southward extended or shifted transient and stationary PW activity was observed in the latitudinally displaced events compared to the normal event in 2006 which was indicatively connected to the QBO phase.

How do these results contribute to a refinement of our conceptual understanding of SSWs? This is illustrated in Figure 8.1 which extends a schematic originally going back to *Matsuno* (1971). Matsuno divided the generation of a SSW in two phases. The first

phase covers the interaction of transient PWs with the mean flow and the second phase is characterized by the warming/cooling in the stratosphere/mesosphere as well as the downward propagation of the wind reversal from the stratosphere. For the first phase of Matsuno’s model our composite analysis indicates a difference in the height range of the occurrence of PWs between minor and major warmings. We find that the properties of minor SSWs are well described by Matsuno’s model (see Figure 8.1a). However, for the major SSWs mainly considered here, we find significant deviations from his original work (see Figure 8.1b) especially in the mesosphere. The latitudinally displaced SSWs show an increased PW activity from the pole down to 30°N and thus a southward extended wind reversal (see Figure 8.1c). These results require additional model studies in the future in order to identify the mechanism leading to this morphology.

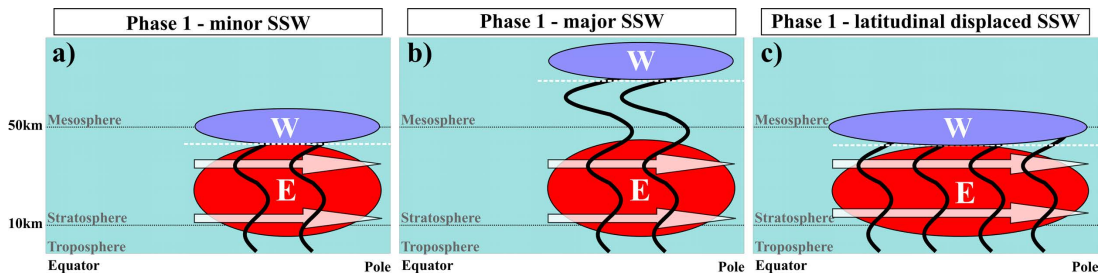


Figure 8.1 Enhancement proposal of Matsuno’s model divided into three different SSW types: a) minor warming (original version of Matsuno’s model) b) major warming and c) latitudinal displaced warming.

The Hiccup of the fall transition shows effects similar to that of a SSW, i.e., temperature increase/decrease in the stratosphere/mesosphere and zonal wind weakening, but with a distinctively smaller magnitude. The composite analysis of the zonal wind variation during the fall transition shows an increase of the zonal wind before the Hiccup and an upward propagation of the zonal wind weakening after the Hiccup onset day. The temperature changes lag the wind changes by a few days in the stratosphere but show a warming in the troposphere at the same time as to the wind decreases. The assumption that the Hiccup is induced by the sudden turn-on of the PW activity is confirmed.

While the Hiccup and the SSW show very similar effects in the middle atmosphere, the underlying processes seem to be different. In the case of a SSW the zonal wind changes seem to propagate downward, however they propagate upward during the Hiccup. Additionally, the PW activity is generally high around the SSW, in contrast it is generally low and only starts around the Hiccup. Thus, both coupling process have similar effects on the middle atmosphere but the processes causing these effects are not the same. For the SSW, the general process was described by *Matsuno* (1971). The process behind the Hiccup is still unclear but the above mentioned assumption about the role of PWs was confirmed.

One of the future plans concerning the study of SSWs includes a further comparison

Chapter 8 Summary and Outlook

of the wind and temperature variations, as well as the PW activity of minor and major SSWs to get a better understanding of the preconditioning phase up to the MLT region of SSWs. The differences in the wind and temperature behavior before and during these two types of SSW could possibly be identified with a composite analysis of the corresponding variations. The longitudinal variation of SSWs, briefly discussed in section 6.3, is planned to be studied with global satellite and reanalysis data in the stratosphere and mesosphere as well as with a chain of radars in a longitude band in the mesosphere covering Europe, North America and Japan. This will allow us to put the local measurements into a global context and to check in how far the local observations are representative for the zonal mean.

To improve our understanding of the dynamics of the Hiccup a further analysis of the PW activity (stationary and transient) as well as of the stationary wave flux is planned. In addition, the tropospheric and mesospheric wind morphology should be studied in more detail using both reanalysis data and local MF radar data.

Appendix A The quasi-geostrophic potential vorticity equation

In the following the derivation of the quasi-geostrophic potential vorticity equation, describing the behavior of PWs in the middle atmosphere, is shown from the primitive equations on a beta plane for quasi-geostrophic flow. The derivation is adapted from *Andrews et al.* (1987).

As mentioned in chapter 2, the primitive equations on a beta plane for quasi-geostrophic flow result from the primitive equations, describing approximately the Earth's atmosphere, due to a geometrical simplification and dynamical approximation. The geometrical simplification includes the change from spherical to cartesian coordinates (projection on a plane). The Coriolis parameter is then presented by $f = f_0 + \beta y$ where $f_0 \equiv 2\Omega \sin(\phi)$ and $\beta \equiv 2\Omega a^{-1} \cos(\phi)$.

The dynamical approximation restricts the resulting equations to large-scale flow, i.e., the Coriolis effect is roughly balanced by the vertical component of the geopotential. Thus, the horizontal wind is a composition of the geostrophic and ageostrophic wind velocities:

$$u = u_g + u_a, \quad v = v_g + v_a, \quad w = w_a \quad (\text{A.1})$$

whereas the vertical wind equals the vertical component of the ageostrophic wind and the horizontal geostrophic wind is defined by the geostrophic stream function

$$u_g = -\frac{\partial\psi}{\partial y}, \quad v_g = \frac{\partial\psi}{\partial x}. \quad (\text{A.2})$$

The thermal wind $\frac{\partial u_g}{\partial z}$ is then described by:

$$\frac{\partial u_g}{\partial z} = -\frac{R}{Hf_0} e^{(-\kappa z/H)} \frac{\partial\theta}{\partial y}, \quad \frac{\partial v_g}{\partial z} = \frac{R}{Hf_0} e^{-\kappa z/H} \frac{\partial\theta}{\partial x} \quad (\text{A.3})$$

with $\theta_e \equiv \theta - \theta_0(z) = \frac{Hf_0}{R} e^{-\kappa z/H} \frac{\partial\psi}{\partial z}$.

With this simplification and approximation as well as a further scaling analysis the

Appendix A The quasi-geostrophic potential vorticity equation

primitive equations on a beta-plane for quasi-geostrophic flow follows:

$$\frac{Du_g}{Dt} - f_0 v_a - \beta y v_g = X \quad (\text{A.4a})$$

$$\frac{Dv_g}{Dt} + f_0 u_a + \beta y u_g = Y \quad (\text{A.4b})$$

$$\frac{\partial u_a}{\partial x} + \frac{\partial v_a}{\partial y} + \frac{1}{\rho} \frac{\partial}{\partial z} (\rho w_a) = 0 \quad (\text{A.4c})$$

$$\frac{D\theta_e}{Dt} + w_a \frac{\partial \theta_0}{\partial z} = Q \quad (\text{A.4d})$$

where

$$\frac{D}{Dt} = \frac{\partial}{\partial t} + u_g \frac{\partial}{\partial x} + v_g \frac{\partial}{\partial y}.$$

This is the basis from which the quasi-geostrophic potential vorticity equation is derived.

This set of equations is still unhandy. The goal is to get a single useful equation. This is done in two steps. First of all, the derivations of the first two equations are subtracted from each other ($\partial/\partial x(\text{A.4b}) - \partial/\partial y(\text{A.4a})$) as follows:

$$\frac{\partial}{\partial x} \left(\frac{Dv_g}{Dt} + f_0 u_a + \beta y u_g \right) - \frac{\partial}{\partial y} \left(\frac{Du_g}{Dt} + f_0 v_a - \beta y v_g \right) = \frac{\partial Y}{\partial x} - \frac{\partial X}{\partial y} \quad (\text{A.5})$$

$$\Leftrightarrow \frac{\partial}{\partial x} \frac{Dv_g}{Dt} + f_0 \frac{\partial u_a}{\partial x} + \beta y \frac{\partial u_g}{\partial x} - \frac{\partial}{\partial y} \frac{Du_g}{Dt} - f_0 \frac{\partial v_a}{\partial y} + \beta v_g + \beta y \frac{\partial v_g}{\partial y} = \frac{\partial Y}{\partial x} - \frac{\partial X}{\partial y}. \quad (\text{A.6})$$

Consider first:

$$\begin{aligned} \frac{\partial}{\partial x} \frac{Dv_g}{Dt} &= \frac{\partial^2 v_g}{\partial x \partial t} + \frac{\partial u_g}{\partial x} \cdot \frac{\partial v_g}{\partial x} + u_g \frac{\partial^2 v_g}{\partial x^2} + \frac{\partial v_g}{\partial x} \cdot \frac{\partial u_g}{\partial x} + v_g \frac{\partial^2 v_g}{\partial x \partial y} \\ &= \frac{D}{Dt} \frac{\partial v_g}{\partial x} + \frac{\partial v_g}{\partial x} \underbrace{\left(\frac{\partial u_g}{\partial x} + \frac{\partial u_g}{\partial x} \right)}_{=0, \text{ since (A.2)}} \\ &= \frac{D}{Dt} \frac{\partial v_g}{\partial x}. \end{aligned}$$

Analog follows:

$$\frac{\partial}{\partial y} \frac{Du_g}{Dt} = \frac{D}{Dt} \frac{\partial u_g}{\partial y}.$$

Consider now

$$\frac{D(f_0 + \beta y)}{Dt} = \underbrace{\frac{\partial(f_0 + \beta y)}{\partial t}}_{=0} + u_g \underbrace{\frac{\partial(f_0 + \beta y)}{\partial x}}_{=0} + v_g \underbrace{\frac{\partial(f_0 + \beta y)}{\partial y}}_{=\beta} = v_g \beta.$$

Thus, for equation (A.6) follows:

$$\frac{D}{Dt} \underbrace{\left(f_0 + \beta y + \frac{\partial v_g}{\partial x} - \frac{\partial u_g}{\partial y} \right)}_{=:\xi} + f_0 \underbrace{\left(\frac{\partial u_a}{\partial x} + \frac{\partial v_a}{\partial y} \right)}_{=-\frac{1}{\rho} \frac{\partial \rho w_a}{\partial z}} + \beta y \underbrace{\left(\frac{\partial v_g}{\partial y} + \frac{\partial u_g}{\partial x} \right)}_{=0, \text{ with (A.2)}} = \frac{\partial Y}{\partial x} - \frac{\partial X}{\partial y} \quad (\text{A.7})$$

$$\Leftrightarrow \frac{D\xi}{Dt} = \frac{f_0}{\rho} \frac{\partial \rho w_a}{\partial z} + \frac{\partial Y}{\partial x} - \frac{\partial X}{\partial y}, \quad (\text{A.8})$$

where ξ is the geostrophic approximation of the beta-plane form of the vertical component of the absolute vorticity.

The goal of the second step is to eliminate the vertical ageostrophic wind w_a . This is done by multiplying (A.4d) with $\rho/(\partial\theta_0/\partial z)$ and inserting the result into (A.8). Thus,

$$\frac{D\xi}{Dt} = \frac{f_0}{\rho} \frac{\partial}{\partial z} \left(\frac{\rho Q}{\partial\theta_0/\partial z} - \frac{D}{Dt} \frac{\rho\theta_e}{\partial\theta_0/\partial z} \right) + \frac{\partial Y}{\partial x} - \frac{\partial X}{\partial y}. \quad (\text{A.9})$$

Consider closely the term:

$$\begin{aligned} \frac{f_0}{\rho} \frac{\partial}{\partial z} \frac{D}{Dt} \frac{\rho\theta_e}{\partial\theta_0/\partial z} &= \frac{f_0}{\rho} \left[\frac{\partial}{\partial t} \frac{\partial}{\partial z} \frac{\rho\theta_e}{\partial\theta_0/\partial z} + \frac{\partial u_g}{\partial z} \frac{\partial}{\partial x} \frac{\rho\theta_e}{\partial\theta_0/\partial z} + u_g \frac{\partial}{\partial x} \frac{\partial}{\partial z} \frac{\rho\theta_e}{\partial\theta_0/\partial z} \right. \\ &\quad \left. + \frac{\partial v_g}{\partial z} \frac{\partial}{\partial x} \frac{\rho\theta_e}{\partial\theta_0/\partial z} + v_g \frac{\partial}{\partial x} \frac{\partial}{\partial z} \frac{\rho\theta_e}{\partial\theta_0/\partial z} \right] \\ &= \frac{f_0}{\rho} \frac{D}{Dt} \frac{\partial}{\partial z} \left(\frac{\rho\theta_e}{\partial\theta_0/\partial z} \right) + \underbrace{\frac{\partial u_g}{\partial z} \frac{\partial}{\partial x} \frac{\rho\theta_e}{\partial\theta_0/\partial z} + \frac{\partial v_g}{\partial z} \frac{\partial}{\partial x} \frac{\rho\theta_e}{\partial\theta_0/\partial z}}_{=0 \text{ with (A.3)}} \\ &= \frac{D}{Dt} \frac{f_0}{\rho} \frac{\partial}{\partial z} \left(\frac{\rho\theta_e}{\partial\theta_0/\partial z} \right). \end{aligned}$$

Inserting this result into equation (A.9) yields:

$$\frac{D}{Dt} \left(\xi + \frac{f_0}{\rho} \frac{\partial}{\partial z} \left(\frac{\rho\theta_e}{\partial\theta_0/\partial z} \right) \right) = \frac{f_0}{\rho} \frac{\partial}{\partial z} \frac{\rho Q}{\partial\theta_0/\partial z} + \frac{\partial Y}{\partial x} - \frac{\partial X}{\partial y}. \quad (\text{A.10})$$

The term on the left hand side is the quasi-geostrophic potential vorticity q :

$$q = \xi + \frac{f_0}{\rho} \frac{\partial}{\partial z} \left(\frac{\rho\theta_e}{\partial\theta_0/\partial z} \right) = f_0 + \beta y + \frac{\partial v_g}{\partial x} - \frac{\partial u_g}{\partial y} + \frac{f_0}{\rho} \frac{\partial}{\partial z} \left(\frac{\rho\theta_e}{\partial\theta_0/\partial z} \right). \quad (\text{A.11})$$

Thus, equation (A.10) can be rewritten as

$$\frac{Dq}{Dt} = \frac{f_0}{\rho} \frac{\partial}{\partial z} \frac{\rho Q}{\partial\theta_0/\partial z} + \frac{\partial Y}{\partial x} - \frac{\partial X}{\partial y} \quad (\text{A.12})$$

and presents the quasi-geostrophic potential vorticity equation.

Appendix B The three-dimensional Plumb flux

The following derivation of the three-dimensional Plumb flux was originally presented in *Plumb* (1985). The initial point of this derivation is the quasi-geostrophic potential vorticity equation (A.12) which is derived in Appendix A.

In addition, the vertical gradient of the streamfunction ψ is needed. It is related to the potential temperature θ by the hydrostatic relation for a perfect gas by

$$\frac{\partial\psi}{\partial z} = \frac{Rp^\kappa\theta}{fH} \quad (\text{B.1})$$

where R is the gas constant, f the Coriolis parameter, p the pressure divided by 1000 hPa, $z = -H \ln p$ with scale height H and $\kappa \equiv \frac{R}{c_p} \approx \frac{2}{7}$ where c_p is the specific heat at constant pressure.

The terms on the right hand side of the quasi-geostrophic potential vorticity equation are summarized to a term S which represents the sources and sinks of potential vorticity. Equation (A.12) can be rewritten as:

$$\frac{Dq}{Dt} \equiv \frac{\partial q}{\partial t} + u \frac{\partial q}{\partial x} + v \frac{\partial q}{\partial y} = S. \quad (\text{B.2})$$

Just for recollection, the quasi-geostrophic potential vorticity q is given by :

$$q = f + \beta y + \frac{\partial v_g}{\partial x} - \frac{\partial u_g}{\partial y} + \frac{f}{\rho} \frac{\partial}{\partial z} \left(\frac{\rho \theta_e}{\partial \theta_0 / \partial z} \right). \quad (\text{B.3})$$

However, *Plumb* (1985) uses the pressure p instead of the density ρ . Thus, by inserting $\rho = p/RT$ and using $\frac{\theta_e}{\partial \theta_0 / \partial z} = \frac{f}{N^2} \frac{\partial \psi}{\partial z}$ follows for the potential vorticity

$$q = f + \beta y + \frac{\partial^2 \psi}{\partial x^2} + \frac{\partial^2 \psi}{\partial y^2} + \frac{f^2}{p} \frac{\partial}{\partial z} \left(\frac{p}{N^2} \frac{\partial \psi}{\partial z} \right). \quad (\text{B.4})$$

To linearize equation (B.2) the perturbation ansatz ($a = \bar{a} + a'$) is applied. For the single parameters holds:

$$\begin{aligned} u &= U(y, z), & v_g &= v'_g, & \psi &= \Psi(y, z) + \psi', \\ q &= Q(y, z) + q', & \theta &= \Theta(y, z) + \theta'. \end{aligned}$$

and hence for the potential vorticity and the geostrophic meridional wind

$$q' = \frac{\partial^2 \psi'}{\partial x^2} + \frac{\partial^2 \psi'}{\partial y^2} + \frac{f^2}{p} \frac{\partial}{\partial z} \left(\frac{p}{N^2} \frac{\partial \psi'}{\partial z} \right) \quad (\text{B.5})$$

$$v'_g = \frac{\partial \Psi(y, z)}{\partial x} + \frac{\partial \psi'}{\partial x} = \frac{\partial \psi'}{\partial x}. \quad (\text{B.6})$$

Inserting this into the potential vorticity equation yields:

$$\begin{aligned} S' &= \frac{\partial(Q(y, z) + q')}{\partial t} + U(y, z) \frac{\partial(Q(y, z) + q')}{\partial x} + v'_g \frac{\partial(Q(y, z) + q')}{\partial y} \\ &= \cancel{\frac{\partial Q(y, z)}{\partial t}} + \frac{\partial q'}{\partial t} + U(y, z) \left(\cancel{\frac{\partial Q(y, z)}{\partial x}} + \frac{\partial q'}{\partial x} \right) + v'_g \left(\frac{\partial Q(y, z)}{\partial y} + \cancel{\frac{\partial q'}{\partial y}} \right) \\ &= \frac{dq'}{dt} + v' \frac{\partial Q(y, z)}{\partial y} \quad \text{where} \quad \frac{d}{dt} = \frac{\partial}{\partial t} + U(y, z) \frac{\partial}{\partial x}. \end{aligned} \quad (\text{B.7})$$

Note, that the term $v'_g \frac{\partial q'}{\partial y}$ vanishes due to the linearization.

The next step is to multiply equation (B.7) with q' , which gives:

$$\begin{aligned} S'q' &= q' \frac{dq'}{dt} + v'q' \frac{\partial Q(y, z)}{\partial y} \\ &= q' \frac{\partial q'}{\partial t} + q'U(y, z) \frac{\partial q'}{\partial x} + v'_g q' \frac{\partial Q(y, z)}{\partial y} \\ &= \frac{1}{2} \frac{\partial q'^2}{\partial t} + \frac{1}{2} U(y, z) \frac{\partial q'}{\partial x} + v'_g q' \frac{\partial Q(y, z)}{\partial y} \quad (\text{chain rule}) \\ &= \frac{1}{2} \frac{dq'^2}{dt} + v'_g q' \frac{\partial Q(y, z)}{\partial y}. \end{aligned} \quad (\text{B.8})$$

Consider now the term $v'_g q'$ more closely:

$$v'_g q' = \frac{1}{p} \frac{\partial \psi'}{\partial x} \left[p \frac{\partial^2 \psi'}{\partial x^2} + p \frac{\partial^2 \psi'}{\partial y^2} + f^2 \frac{\partial}{\partial z} \left(\frac{p}{N^2} \frac{\partial \psi'}{\partial z} \right) \right]. \quad (\text{B.9})$$

The deviations of the streamfunction can also be written as:

$$\begin{aligned} \frac{\partial}{\partial x} \left(\frac{\partial \psi'}{\partial x} \right)^2 &= 2 \frac{\partial \psi'}{\partial x} \frac{\partial^2 \psi'}{\partial x^2}, \\ \frac{\partial}{\partial y} \left(\frac{\partial \psi'}{\partial x} \frac{\partial \psi'}{\partial y} \right) &= \frac{\partial^2 \psi'}{\partial y \partial x} \frac{\partial \psi'}{\partial y} + \frac{\partial \psi'}{\partial x} \frac{\partial^2 \psi'}{\partial y^2}, \\ \frac{\partial}{\partial x} \left(\frac{\partial \psi'}{\partial y} \right)^2 &= 2 \frac{\partial \psi'}{\partial y} \frac{\partial^2 \psi'}{\partial x \partial y}. \end{aligned}$$

Inserting these translations into equation (B.9) gives:

$$\begin{aligned} v'_g q' &= \frac{1}{p} \left[\frac{p}{2} \frac{\partial}{\partial x} \left(\frac{\partial \psi'}{\partial x} \right)^2 - \frac{p}{2} \frac{\partial}{\partial x} \left(\frac{\partial \psi'}{\partial y} \right)^2 + p \frac{\partial}{\partial y} \left(\frac{\partial \psi'}{\partial x} \frac{\partial \psi'}{\partial y} \right) \right. \\ &\quad \left. + f^2 \left(\frac{\partial}{\partial z} \left(\frac{p}{N^2} \right) \frac{\partial \psi'}{\partial x} \frac{\partial \psi'}{\partial z} + \frac{p}{N^2} \frac{\partial}{\partial z} \frac{\partial \psi'}{\partial x} \frac{\partial \psi'}{\partial z} - \frac{p}{2N^2} \frac{\partial}{\partial x} \left(\frac{\partial \psi'}{\partial z} \right)^2 \right) \right]. \end{aligned} \quad (\text{B.10})$$

Appendix B The three-dimensional Plumb flux

Combining the deviations with respect to z results in:

$$v'_g q' = \frac{1}{p} \left[\frac{p}{2} \frac{\partial}{\partial x} \left(\frac{\partial \psi'}{\partial x} \right)^2 - \frac{p}{2} \frac{\partial}{\partial x} \left(\frac{\partial \psi'}{\partial y} \right)^2 + p \frac{\partial}{\partial y} \left(\frac{\partial \psi'}{\partial x} \frac{\partial \psi'}{\partial y} \right) - \frac{f^2 p}{2N^2} \frac{\partial}{\partial x} \left(\frac{\partial \psi'}{\partial z} \right)^2 + \frac{\partial}{\partial z} \left(\frac{f^2 p}{N^2} \left(\frac{\partial \psi'}{\partial x} \frac{\partial \psi'}{\partial z} \right) \right) \right]. \quad (\text{B.11})$$

Hence,

$$\begin{aligned} v'_g q' &= \frac{1}{p} \left[p \frac{\partial}{\partial x} \left(\frac{1}{2} \left(\frac{\partial \psi'}{\partial x} \right)^2 - \frac{1}{2} \left(\frac{\partial \psi'}{\partial y} \right)^2 - \frac{f^2}{2N^2} \left(\frac{\partial \psi'}{\partial z} \right)^2 \right) \right. \\ &\quad \left. + p \frac{\partial}{\partial y} \left(\frac{\partial \psi'}{\partial x} \frac{\partial \psi'}{\partial y} \right) + p \frac{\partial}{\partial z} \left(\frac{f^2}{N^2} \left(\frac{\partial \psi'}{\partial x} \frac{\partial \psi'}{\partial z} \right) \right) \right] \\ &= \frac{1}{p} \nabla \cdot \vec{B} \end{aligned} \quad (\text{B.12})$$

where $N^2 = \left(\frac{R p^\kappa}{H} \frac{\partial \Theta}{\partial z} \right)$ and

$$\vec{B} = p \begin{pmatrix} \frac{1}{2} \left(\frac{\partial \psi'}{\partial x} \right)^2 - \frac{1}{2} \left(\frac{\partial \psi'}{\partial y} \right)^2 - \frac{f^2}{2N^2} \left(\frac{\partial \psi'}{\partial z} \right)^2 \\ \frac{\partial \psi'}{\partial x} \frac{\partial \psi'}{\partial y} \\ \frac{f^2}{N^2} \frac{\partial \psi'}{\partial x} \frac{\partial \psi'}{\partial z} \end{pmatrix}. \quad (\text{B.13})$$

By using the geostrophic wind definition (see eq. (A.2)) the vector can be rewritten as:

$$\vec{B} = p \begin{pmatrix} v_g'^2 - E \\ -u_g' v_g' \\ f v_g' \theta' / (\partial \Theta / \partial z) \end{pmatrix} \quad (\text{B.14})$$

where

$$E = \frac{1}{2} \left(u_g'^2 + v_g'^2 + \frac{R p^\kappa \theta'^2}{H (\partial \Theta / \partial z)} \right). \quad (\text{B.15})$$

Inserting now equation (B.12) into equation (B.8) follows:

$$S' q' = \frac{1}{2} \frac{dq'^2}{dt} + \frac{1}{p} \frac{\partial Q(y, z)}{\partial y} \nabla \cdot \vec{B} \quad \left| \div \frac{\partial Q(y, z)}{\partial y}, \cdot p \right. \quad (\text{B.16})$$

$$\Leftrightarrow \underbrace{\frac{p S' q'}{\partial Q / \partial y}}_{=C} = \underbrace{\frac{p}{2} \frac{dq'^2}{dt} \frac{1}{\partial Q / \partial y}}_{=\frac{dA}{dt}} + \nabla \cdot \vec{B} \quad (\text{B.17})$$

$$\Rightarrow C = \frac{dA}{dt} + \nabla \cdot \vec{B} \quad (\text{B.18})$$

where $A = \frac{p}{2} \frac{q'^2}{\partial Q / \partial y}$.

This equation represents the conservation relation for wave activity where C is the source and sinks of the waves, $\frac{DA}{Dt}$ is the rate of change following the mean flow of density A of the wave activity to the divergence of the radiative flux \vec{B} . Note, that the flux B differs from the Eliassen-Palm flux only in a zonal component.

Most applications will be with time-averaged data. Thus, the time-averaged term $\frac{\partial A}{\partial t} = 0$. Hence, it is useful to rewrite equation (B.18) as

$$C = \frac{\partial A}{\partial t} + U \frac{\partial A}{\partial x} + \nabla \cdot \vec{B} \quad (\text{B.19})$$

$$= \frac{\partial A}{\partial t} + \nabla \cdot \underbrace{(\vec{B} + \vec{U}A)}_{=\vec{B}^T} \quad (\text{B.20})$$

$$= \frac{\partial A}{\partial t} + \nabla \cdot \vec{B}^T \quad (\text{B.21})$$

with $\vec{U} = (U, 0, 0)$ whereas the term \vec{B}^T is the total flux (radiative and advective) of wave activity.

To study only stationary waves the phase dependence has to be removed from \vec{B}^T . This is done by time-averaging for transient waves and by adding the nonconservative quantity $\nabla \cdot \vec{G}$ to equation (B.21):

$$C = \frac{\partial A}{\partial t} + \nabla \cdot \vec{B}^T + \nabla \cdot \vec{G} \quad (\text{B.22})$$

$$\Leftrightarrow C_s = C + \nabla \cdot \vec{G} = \frac{\partial A}{\partial t} + \nabla \cdot \vec{B}^T + \nabla \cdot \vec{G} \quad (\text{B.23})$$

$$= \frac{\partial A}{\partial t} + \nabla \cdot \underbrace{(\vec{B}^T + \vec{G})}_{=\vec{F}_p} \quad (\text{B.24})$$

$$= \frac{\partial A}{\partial t} + \nabla \cdot \vec{F}_p \quad (\text{B.25})$$

For Plumb, a suitable choice for \vec{G} for stationary waves is

$$\vec{G} = \frac{p}{4} \begin{pmatrix} \frac{\partial^2(\psi'^2)}{\partial y^2} + \frac{f^2}{p} \frac{\partial}{\partial z} \left(\frac{p}{N^2} \frac{\partial(\psi'^2)}{\partial z} \right) - \frac{2r'q'}{\partial Q / \partial y} \\ -\frac{\partial^2(\psi'^2)}{\partial x \partial y} \\ -\frac{f^2}{N^2} \frac{\partial^2(\psi'^2)}{\partial x \partial z} \end{pmatrix} \quad (\text{B.26})$$

where r' is a nonconservative perturbation quantity defined by

$$\frac{\partial r'}{\partial x} = S'. \quad (\text{B.27})$$

Appendix B The three-dimensional Plumb flux

Thus, the vector \vec{F}_p is given by

$$\vec{F}_p = \vec{B} + \vec{U}A + \vec{G} \quad (\text{B.28})$$

$$= \frac{p}{2} \begin{pmatrix} \left(\frac{\partial \psi'}{\partial x} \right)^2 - \left(\frac{\partial \psi'}{\partial y} \right)^2 - \frac{f^2}{N^2} \left(\frac{\partial \psi'}{\partial z} \right)^2 + \frac{Uq'^2}{\partial Q / \partial y} \\ + \frac{1}{2} \left(\frac{\partial^2(\psi'^2)}{\partial y^2} + \frac{f^2}{p} \frac{\partial}{\partial z} \left(\frac{p}{N^2} \frac{\partial(\psi'^2)}{\partial z} \right) - \frac{2r'q'}{\partial Q / \partial y} \right) \\ 2 \frac{\partial \psi'}{\partial x} \frac{\partial \psi'}{\partial y} - \frac{1}{2} \frac{\partial^2(\psi'^2)}{\partial x \partial y} \\ \frac{2f^2}{N^2} \frac{\partial \psi'}{\partial x} \frac{\partial \psi'}{\partial z} - \frac{f^2}{2N^2} \frac{\partial^2(\psi'^2)}{\partial x \partial z} \end{pmatrix} \quad (\text{B.29})$$

$$= \frac{p}{2} \begin{pmatrix} \left(\frac{\partial \psi'}{\partial x} \right)^2 + (Uq'^2 - r'q') / \frac{\partial Q}{\partial y} - \left(\frac{\partial \psi'}{\partial y} \right)^2 + \left(\frac{\partial \psi'}{\partial y} \right)^2 + \psi' \frac{\partial^2 \psi'}{\partial y^2} \\ + \frac{f^2}{N^2} \frac{\partial \psi'}{\partial z} + \frac{f^2}{2p} \left(\frac{\partial}{\partial z} \left(\frac{p}{N^2} \right) \frac{\partial \psi'}{\partial z} + \frac{p}{N^2} \left(\frac{\partial \psi'}{\partial z} \right)^2 + 2\psi' \frac{\partial^2 \psi'}{\partial z^2} \right) \\ 2 \frac{\partial \psi'}{\partial x} \frac{\partial \psi'}{\partial y} - \frac{\partial \psi'}{\partial x} \frac{\psi'}{\partial y} - \psi' \frac{\partial^2 \psi'}{\partial x \partial y} \\ \frac{f^2}{N^2} \left(2 \frac{\partial \psi'}{\partial x} \frac{\partial \psi'}{\partial z} - \frac{\partial \psi'}{\partial x} \frac{\psi'}{\partial z} - \psi' \frac{\partial^2 \psi'}{\partial x \partial z} \right) \end{pmatrix} \quad (\text{B.30})$$

$$= \frac{p}{2} \begin{pmatrix} \left(\frac{\partial \psi'}{\partial x} \right)^2 - \psi' \frac{\partial^2 \psi'}{\partial x^2} + \psi' q' + (Uq'^2 - r'q') / \frac{\partial Q}{\partial y} \\ \frac{\partial \psi'}{\partial x} \frac{\partial \psi'}{\partial y} - \psi' \frac{\partial^2 \psi'}{\partial x \partial y} \\ \frac{f^2}{N^2} \left(\frac{\partial \psi'}{\partial x} \frac{\partial \psi'}{\partial z} - \psi' \frac{\partial^2 \psi'}{\partial x \partial z} \right) \end{pmatrix}. \quad (\text{B.31})$$

Further, inserting equation (B.27) into equation (B.7) gives for stationary waves (time-averaged) together with the geostrophic wind

$$U \frac{\partial q'}{\partial x} + \frac{\partial \psi'}{\partial x} \frac{\partial Q}{\partial y} = \frac{\partial r'}{\partial x}. \quad (\text{B.32})$$

Integrating and multiplying this equation with q' gives

$$\psi' q' \frac{\partial Q}{\partial y} + Uq'^2 + r'q' = 0 \quad (\text{B.33})$$

whereas r' , q' and ψ' are perturbation quantities whose integral over x vanishes. Thus, the vector \vec{F}_p can be rewritten as

$$\vec{F}_p = \frac{p}{2} \begin{pmatrix} \left(\frac{\partial \psi'}{\partial x} \right)^2 - \psi' \frac{\partial^2 \psi'}{\partial x^2} \\ \frac{\partial \psi'}{\partial x} \frac{\partial \psi'}{\partial y} - \psi' \frac{\partial^2 \psi'}{\partial x \partial y} \\ \frac{f^2}{N^2} \left(\frac{\partial \psi'}{\partial x} \frac{\partial \psi'}{\partial z} - \psi' \frac{\partial^2 \psi'}{\partial x \partial z} \right) \end{pmatrix} \quad (\text{B.34})$$

This vector is called the Plumb flux vector in cartesian coordinates.

The Plumb flux in spherical coordinates

To apply the 3-D Plumb flux on observations, an extension to spherical coordinates is needed. The derivation of the Plumb flux vector in spherical coordinates is analog to that shown above for the cartesian coordinates and can also be find in *Plumb* (1985). The geostrophic wind in spherical coordinates is defined by

$$u_g = -\frac{1}{a} \frac{\partial \psi}{\partial \phi}, \quad v_g = \frac{1}{a \cos(\phi)} \frac{\partial \psi}{\partial \lambda} \quad (\text{B.35})$$

where the streamfunction ψ is defined by $\psi = \frac{\Psi}{2\Omega \sin(\phi)}$ with Ψ is the geopotential, Ω the Earth's rotation rate, a the Earth's radius, ϕ the latitude and λ the longitude. The derivation of the Plumb flux is now analog to above shown derivation in cartesian coordinates. The three-dimensional Plumb flux vector in spherical coordinates is given by

$$\vec{F}_{\text{plumb}} = p \cos(\phi) \begin{pmatrix} \frac{1}{2a^2 \cos^2(\phi)} \left[\left(\frac{\partial \psi'}{\partial \lambda} \right)^2 - \psi' \frac{\partial^2 \psi'}{\partial \lambda^2} \right] \\ \frac{1}{2a^2 \cos(\phi)} \left(\frac{\partial \psi'}{\partial \lambda} \frac{\partial \psi'}{\partial \phi} - \psi' \frac{\partial^2 \psi'}{\partial \lambda \partial \phi} \right) \\ \frac{2\Omega^2 \sin^2(\phi)}{N^2 a \cos(\phi)} \left(\frac{\partial \psi'}{\partial \lambda} \frac{\partial \psi'}{\partial z} - \psi' \frac{\partial^2 \psi'}{\partial \lambda \partial z} \right) \end{pmatrix}. \quad (\text{B.36})$$

The application of the Plumb flux to real data requires a rewriting of equation (B.36) by using the geostrophic and thermal wind relation:

$$\vec{F}_{\text{plumb}} = p \cos(\phi) \begin{pmatrix} v'^2 - \frac{1}{2\Omega a \sin 2\phi} \frac{\delta(v'\Phi')}{\partial \lambda} \\ -u'v' + \frac{1}{2\Omega a \sin 2\phi} \frac{\delta(u'\Phi')}{\partial \lambda} \\ \frac{2\Omega \sin \phi}{J} \left[v'T' - \frac{1}{2\Omega a \sin 2\phi} \frac{\partial}{\partial \lambda} (T'\Phi') \right] \end{pmatrix} \quad (\text{B.37})$$

where

$$J = \frac{\partial \bar{T}}{\partial z} + \frac{\kappa \bar{T}}{H}. \quad (\text{B.38})$$

Appendix C Tables

	Tavistock (CMOR) (43°N, 81°W)	Juliusruh (55°N, 13°E)	Andenes (69°N, 16°E)	Eureka (80°N, 86°W)
Frequency	17.45, 29.85, 38.15 MHz	32.55 MHz	32.55 MHz	32.55 MHz
Power	6 kW	12 kW	18 kW	12 kW
PRF	532	2114	2094	2094
Coherent integ.	1	4	4	4
Height range	70 – 120 km	80 – 100 km	80 – 100 km	80 – 100 km
Sampling resol.	3 km	2 km	2 km	2 km
Wind analysis	DBS	DBS	DBS	DBS
Observation since	1999 – today	2007 – today	2001 – today	2007 – today

Table C.1 Technical details of MR systems at Tavistock (CMOR), Juliusruh, Andenes and Eureka.

	Saskatoon (52°N, 107°W)	Juliusruh (55°N, 13°E)	Andenes (69°N, 16°E)
Radar	MF	MF	MF
Frequency	2.22 MHz	3.17 MHz	1.98 MHz
Peak power	20 kW	128 kW	40 kW
Beam width	~ 15°	~ 15°	~ 60°
Height range	60 – 110 km	70 – 94 km	70 – 94 km
Sampling resolutuion	2 km	2 km	2 km
Wind analysis	FCA	FCA	FCA
Observation since	1978 – today	1990 – today	1998 – today

Table C.2 Technical details of MF-radar systems at Saskatoon, Juliusruh and Andenes.

Bibliography

- Andrews, D. G., J. R. Holton, and C. B. Leovy, *Middle atmosphere dynamics*, Academic Press, 1987.
- Azeem, S. M. I., E. R. Talaat, G. G. Sivjee, H.-L. Liu, and R. G. Roble, Observational study of the 4-day wave in the mesosphere preceding the sudden stratospheric warming events during 1995 and 2002, *Geophys. Res. Lett.*, *20*, L15804, doi:10.1029/2005GL023393, 2005.
- Baldwin, M. P., and T. J. Dunkerton, Stratospheric Harbingers of Anomalous Weather Regimes, *Science*, *294* (5542), 581 – 584, doi:10.1126/science.1063315, 2001.
- Beres, J. H., R. R. Garcia, B. A. Boville, and F. Sassi, Implementation of a gravity wave source spectrum parameterization dependent on the properties of convection in the Whole Atmosphere Community Climate Model (WACCM), *J. Geophys. Res.*, *110*(D10), doi:10.1029/2004JD005504, 2005.
- Berrisford, P., D. Dee, K. Fielding, M. Fuentes, P. Kallberg, S. Kobayashi, and S. Uppala, The ERA-Interim Archive, *Technical report*, ECMWF, Shinfield Park, Reading, 2009.
- Brasseur, G., and S. Solomon, *Aeronomy of the Middle Atmosphere*, second ed., D. Reidel Publishing Company, Dordrecht, Holland, 1986.
- Briggs, B., The Analysis of spaced sensor records by correlation techniques, *Middle Atmosphere Program Handbook*, *13*, 166–186, 1984.
- Cevolani, G., Long period waves in the middle atmosphere: Response of mesospheric and thermospheric winds to recent minor stratospheric warmings at mid-latitudes, *Ann. Geophys.*, *7*, 451 – 458, 1989.
- Cevolani, G., Strato-meso-thermospheric coupling at mid-latitudes in the course of mid-winter stratwarmings during DYANA, *Geophys. Res. Lett.*, *18*, 1987–1990, 1991.
- Charlton, A. J., and L. M. Polvani, A New look at stratospheric sudden warmings, Part I: Climatology and modeling Benchmarks, *J. Climate*, *20* (0894-8755), 470 – 488, doi:10.1175/JCLI3994.1, 2007.
- Charlton, A. J., L. M. Polvani, J. Perlwitz, F. Sassi, E. Manzini, K. Shibata, S. Pawson, J. E. Nielsen, and D. Rind, A New Look at Stratospheric Sudden Warmings. Part II:

Bibliography

- Evaluation of Numerical Model Simulations, *J. Climate*, *20*, 470 – 488, doi:10.1175/JCLI3994.1, 2007.
- Charney, J. G., and P. G. Drazin, Propagation of planetary-scale disturbances from the lower into the upper atmosphere, *J. Geophys. Res.*, *66*(1), 83–109, doi:10.1029/JZ066i001p00083, 1961.
- Chen, W., and R.-H. Huang, The modulation of planetary wave propagation by the tropical QBO zonal winds and the associated effects in the residual meridional circulation, *Contrib. Atmos. Phys.*, *72*(6), 187–204, 1999.
- Chen, X., X. Hu, and C. Xiao, Variability of MLT winds and waves over mid-latitude during the 2000/2001 and 2009/2010 winter stratospheric sudden warming, *Ann. Geophys.*, *30*(6), 991–1001, doi:10.5194/angeo-30-991-2012, 2012.
- Chshyolkova, T., A. Manson, C. Meek, S. Avery, D. Thorsen, J. MacDougall, W. Hocking, Y. Murayama, and K. Igarashi, Planetary wave coupling processes in the middle atmosphere (30–90 km): A study involving MetO and MFR data, *J. Atmos. Solar-Terr. Phys.*, *68*(3–5), 353 – 368, doi:http://dx.doi.org/10.1016/j.jastp.2005.05.011, 2006.
- Chshyolkova, T., A. H. Manson, C. E. Meek, T. Aso, S. K. Avery, C. M. Hall, W. Hocking, K. Igarashi, C. Jacobi, N. Makarov, N. Mitchell, Y. Murayama, W. Singer, D. Thorsen, and M. Tsutsumi, Polar vortex evolution during Northern Hemispheric winter 2004/05, *Ann. Geophys.*, *25*(6), 1279–1298, doi:10.5194/angeo-25-1279-2007, 2007.
- Daubechies, I., *Ten Lectures on Wavelets*, Society for Industrial and Applied Mathematics, 1995.
- Day, K. A., R. E. Hibbins, and N. J. Mitchell, Aura MLS observations of the westward-propagating s=1, 16-day planetary wave in the stratosphere, mesosphere and lower thermosphere, *Atmos. Chem. Phys.*, *11*(9), 4149–4161, doi:10.5194/acp-11-4149-2011, 2011.
- de Grandpré, J., S. R. Beagley, V. I. Fomichev, E. Griffioen, J. C. McConnell, A. S. Medvedev, and T. G. Shepherd, Ozone climatology using interactive chemistry: Results from the Canadian Middle Atmosphere Model, *J. Geophys. Res.*, *105*(D21), 26,475–26,491, doi:10.1029/2000JD900427, 2000.
- Dee, D. P., S. M. Uppala, A. J. Simmons, P. Berrisford, P. Poli, S. Kobayashi, U. Andrae, M. A. Balmaseda, G. Balsamo, P. Bauer, P. Bechtold, A. C. M. Beljaars, L. van de Berg, J. Bidlot, N. Bormann, C. Delsol, R. Dragani, M. Fuentes, A. J. Geer, L. Haimberger, S. B. Healy, H. Hersbach, E. V. Hólm, L. Isaksen, P. Kållberg, M. Köhler, M. Matricardi, A. P. McNally, B. M. Monge-Sanz, J.-J. Morcrette, B.-K. Park, C. Peubey, P. de Rosnay, C. Tavolato, J.-N. Thépaut, and F. Vitart, The ERA-Interim reanalysis: configuration and performance of the data assimilation system, *Quart. J. R. Met. Soc.*, *137*(656), 553–597, doi:10.1002/qj.828, 2011.

- Drob, D. P., J. T. Emmert, G. Crowley, J. M. Picone, G. G. Shepherd, W. Skinner, P. Hays, R. J. Niciejewski, M. Larsen, C. Y. She, J. W. Meriwether, G. Hernandez, M. J. Jarvis, D. P. Sipler, C. A. Tepley, M. S. O'Brien, J. R. Bowman, Q. Wu, Y. Murayama, S. Kawamura, I. M. Reid, and R. A. Vincent, An empirical model of the Earth's horizontal wind fields: HWM07, *J. Geophys. Res.*, *113*(A12), doi:10.1029/2008JA013668, 2008.
- Farge, M., Wavelet Transforms and their Applications to Turbulence, *Annu. Rev. Fluid Mech.*, *24*(1), 395–458, doi:10.1146/annurev.fl.24.010192.002143, 1992.
- Forbes, J. M., Tidal and planetary waves, in *The Upper Mesosphere and Lower Thermosphere: A Review of Experiment and Theory*, *Geophys. Monogr. Ser.*, vol. 87, edited by R. M. Johnson and T. L. Killeen, pp. 67 – 87, AGU, Washington, D. C., doi:doi:10.1029/GM087p0067, 1995.
- Fritz, S., and S. D. Soules, Large-Scale Temperature Changes in the Stratosphere Observed from Nimbus III, *J. Atmos. Sci.*, *27*(7), 1091 – 1097, doi:10.1175/1520-0469(1970)027<1091:LSTCIT>2.0.CO;2, 1970.
- Funke, B., M. Lopez-Puertas, D. Bermejo-Pantaleon, M. Garcia-Comas, G. P. Stiller, T. von Clarmann, M. Kiefer, and A. Linden, Evidence for dynamical coupling from the lower atmosphere to the thermosphere during a major stratospheric warming, *Geophys. Res. Lett.*, *37*, L13803, doi:10.1029/2010GL043619, 2010.
- Geller, M. A., Dynamics of the Middle Atmosphere, in *Progress in Solar-Terrestrial Physics*, edited by J. Roederer, pp. 359 – 375, Springer Netherlands, doi:10.1007/978-94-009-7096-0_28, 1983.
- Goncharenko, L. P., and S.-R. Zhang, Ionospheric signatures of sudden stratospheric warming: Ion temperature at middle latitude, *Geophys. Res. Lett.*, *35*, L21103, doi:10.1029/2008GL035684, 2008.
- Gregory, J. B., and A. H. Manson, Wind and waves to 110 km at mid-latitudes: III. Responses of mesospheric and lower thermospheric winds to major stratospheric warmings, *J. Atmos. Sci.*, *32*, 1676 – 1681, 1975.
- Gu, S.-Y., T. Li, X. Dou, Q. Wu, M. G. Mlynczak, and J. M. Russell, Observations of Quasi-Two-Day wave by TIMED/SABER and TIMED/TIDI, *J. Geophys. Res.*, *118*(4), 1624–1639, doi:10.1002/jgrd.50191, 2013.
- Hocking, W., B. Fuller, and B. Vandeppeer, Real-time determination of meteor-related parameters utilizing modern digital technology, *J. Atmos. Solar-Terr. Phys.*, *63*(2-3), 155 – 169, 2001.
- Hocking, W., W. Singer, J. Bremer, N. Mitchell, P. Batista, B. Clemesha, and M. Donner, Meteor radar temperatures at multiple sites derived with SKiYMET radars and compared to OH, rocket and lidar measurements, *J. Atmos. Solar-Terr. Phys.*, *66*(6-9), 585 – 593, 2004.

Bibliography

- Hoffmann, P., W. Singer, and D. Keuer, Variability of the mesospheric wind field at middle and arctic latitudes in winter and its relation to stratospheric circulation disturbances, *J. Atmos. Solar-Terr. Phys.*, *64*, 1229 – 1240, 2002.
- Hoffmann, P., W. Singer, D. Keuer, W. K. Hocking, M. Kunze, and Y. Murayama, Latitudinal and longitudinal variability of mesospheric winds and temperatures during stratospheric warming events, *J. Atmos. Solar-Terr. Phys.*, *69*, 2355–2366, doi:10.1016/j.jastp.2007.06.010, 2007.
- Hoffmann, P., E. Becker, W. Singer, and M. Placke, Seasonal variation of mesospheric waves at northern middle and high latitudes, *J. Atmos. Solar-Terr. Phys.*, *72*, 1068–1079, doi:DOI:10.1016/j.jastp.2010.07.002, 2010.
- Holton, J. R., A semi-spectral numerical model for wave-mean flow interactions in the stratosphere- Application to sudden stratospheric warmings, *J. Atmos. Sci.*, *33*(8), 1639–1649, doi:10.1175/1520-0469(1976)033<1639:ASSNMF>2.0.CO;2, 1976.
- Holton, J. R., The influence of gravity wave breaking on the general circulation of the middle atmosphere, *J. Atmos. Sci.*, *40*(10), 2497–2507, doi:10.1175/1520-0469(1983)040\$<2497:TIOGWB\$>2.0.CO;2, 1983.
- Holton, J. R., *An introduction to dynamic meteorology, International Geophysics Series*, vol. 88, fourth ed., Academic Press, 2004.
- Holton, J. R., and M. J. Alexander, The role of waves in the transport circulation of the middle atmosphere, in *Atmospheric Science Across the Stratopause, Geophys. Monogr. Ser.*, vol. 123, edited by D. E. Siskind, S. D. Eckermann, and M. E. Summers, pp. 21 – 35, AGU, Washington, D. C., doi:10.1029/GM123p0021, 2000.
- Jacobi, C., R. Schminder, and D. Kürschner, The winter mesopause wind field over Central Europe and its response to stratospheric warmings as measured by LF D1 wind measurements at Collm, Germany, *Adv. Space Res.*, *20*(6), 1223–1226, doi:10.1016/S0273-1177(97)00775-8, 1997.
- Jacobi, C., R. Schminder, and D. Kürschner, Non-linear interaction of the quasi 2-day wave and long-term oscillations in the summer midlatitude mesopause region as seen from LF D1 wind measurements over Central Europe (Collm, 52°N, 15°E), *J. Atmos. Solar-Terr. Phys.*, *60*(12), 1175 –, doi:http://dx.doi.org/10.1016/S1364-6826(98)00076-5, 1998a.
- Jacobi, C., R. Schminder, and D. Kürschner, Planetary wave activity obtained from long-period (2–18 days) variations of mesopause region winds over Central Europe (52°N, 15°E), *J. Atmos. Solar-Terr. Phys.*, *60*(1), 81–93, doi:10.1016/S1364-6826(97)00117-X, 1998b.
- Jacobi, C., Y. Portnyagin, T. Solovjova, P. Hoffmann, W. Singer, A. Fahrutdinova, R. Ishmuratov, A. Beard, N. Mitchell, H. Müller, R. Schminder, D. Kürschner, A. Manson, and C. Meek, Climatology of the semidiurnal tide at 52–56°N from ground-based radar wind measurements 1985–1995, *J. Atmos. Solar-Terr. Phys.*, *61*(13), 975 – 991, doi:10.1016/S1364-6826(99)00065-6, 1999.

- Jacobi, C., C. Viehweg, D. Kürschner, W. Singer, P. Hoffmann, and D. Keuer, Comparison of mesopause region meteor radar winds, medium frequency radar winds and low frequency drifts over Germany, *Adv. Space Res.*, *43*(2), 247 – 252, doi:10.1016/j.asr.2008.05.009, 2009.
- Jonsson, A. I., J. de Grandpré, V. I. Fomichev, J. C. McConnell, and S. R. Beagley, Doubled CO₂-induced cooling in the middle atmosphere: Photochemical analysis of the ozone radiative feedback, *J. Geophys. Res.*, *109*(D24), doi:10.1029/2004JD005093, 2004.
- Keuer, D., P. Hoffmann, W. Singer, and J. Bremer, Long-term variations of the mesospheric wind field at mid-latitudes, *Ann. Geophys.*, *25*(8), 1779–1790, 2007.
- Kodera, K., Influence of stratospheric sudden warming on the equatorial troposphere, *Geophys. Res. Lett.*, *33*(6), doi:10.1029/2005GL024510, 2006.
- Krüger, K., B. Naujokat, and K. Labitzke, The unusual midwinter warming in the southern hemisphere stratosphere 2002: A comparison to northern hemisphere phenomena, *J. Atmos. Sci.*, pp. 603–613, doi:10.1175/JAS-3316.1, 2004.
- Kurihara, J., Y. Ogawa, S. Oyama, S. Nozawa, M. Tsutsumi, C. M. Hall, Y. Tomikawa, and R. Fujii, Links between a stratospheric sudden warming and thermal structures and dynamics in the high-latitude mesosphere, lower thermosphere, and ionosphere, *Geophys. Res. Lett.*, *37*, L13806, doi:10.1029/2010GL043643, 2010.
- Kuttippurath, J., and G. Nikulin, The sudden stratospheric warming of the Arctic winter 2009/2010: comparison to other recent warm winters, *Atmos. Chem. Phys. Discuss.*, *12*(3), 7243–7271, doi:10.5194/acpd-12-7243-2012, 2012.
- Labitzke, K., On the signal of the 11-year sunspot cycle in the stratosphere over the Antarctic and its modulation by the Quasi-Biennial Oscillation (QBO), *METZ*, *13*(4), 263–270, doi:10.1127/0941-2948/2004/0013-0263, 2004.
- Labitzke, K., and M. Kunze, On the remarkable Arctic winter in 2008/2009, *J. Geophys. Res.*, *114*(D1), doi:10.1029/2009JD012273, 2009.
- Labitzke, K., and B. Naujokat, The lower Arctic stratosphere in winter since 1952, *SPARC Newsletter*, *15*, 11–14, 2000.
- Limpasuvan, V., D. W. J. Thompson, and D. L. Hartmann, The life cycle of the northern hemisphere sudden stratospheric warmings, *J. Climate*, *17*, 2584–2596, doi:10.1175/1520-0442(2004)017<\$<2584:TLCOTN>\$2.0.CO;2, 2004.
- Limpasuvan, V., D. L. Wu, M. J. Schwartz, J. W. Waters, Q. Wu, and T. L. Killeen, The two-day wave in EOS MLS temperature and wind measurements during 2004–2005 winter, *Geophys. Res. Lett.*, *32*(17), doi:10.1029/2005GL023396, 2005.
- Limpasuvan, V., J. H. Richter, Y. J. Orsolini, F. Stordal, and O.-K. Kvissel, The roles of planetary and gravity waves during a major stratospheric sudden warming as characterized in WACCM, *J. Atmos. Solar-Terr. Phys.*, *78-79*, 84 – 98, doi:10.1016/j.jastp.2011.03.004, 2012.

Bibliography

- Lindzen, R. S., Thermally driven diurnal tide in the atmosphere, *Quart. J. R. Met. Soc.*, *93*(395), 18–42, doi:10.1002/qj.49709339503, 1967.
- Liu, H.-L., and R. G. Roble, A study of a self-generated stratospheric sudden warming and its mesospheric–lower thermospheric impacts using the coupled TIME-GCM/CCM3, *J. Geophys. Res.*, *107*(D23), ACL 15–1–ACL 15–18, doi:10.1029/2001JD001533, 2002.
- Liu, H.-L., R. G. Roble, M. J. Taylor, and W. R. Pendleton, Mesospheric planetary waves at northern hemisphere fall equinox, *Geophys. Res. Lett.*, *28*(9), 1903–1906, doi:10.1029/2000GL012689, 2001.
- Liu, H.-L., E. R. Talaat, R. G. Roble, R. S. Liebermann, D. M. Riggan, and J.-H. Yee, The 6.5-day wave and its seasonal variability in the middle and upper atmosphere, *J. Geophys. Res.*, *109*(D2), D21112, doi:10.1029/2004JD004795, 2004.
- Liu, H.-L., W. Wang, A. D. Richmond, and R. G. Roble, Ionospheric variability due to planetary waves and tides for solar minimum conditions, *J. Geophys. Res.*, *115*, A00G01, doi:10.1029/2009JA015188, 2010.
- Livesey, N., W. Van Snyder, W. Read, and P. Wagner, Retrieval algorithms for the eos microwave limb sounder (mls), *Geoscience and Remote Sensing, IEEE Transactions on*, *44*(5), 1144 – 1155, doi:10.1109/TGRS.2006.872327, 2006.
- Livesey, N. J., W. G. Read, A. Lambert, R. E. Cofield, D. T. Cuddy, L. Froidevaux, R. A. Fuller, R. F. Jarnot, J. H. Jiang, Y. B. Jiang, B. W. Knosp, L. J. Kovalenko, H. M. Pickett, H. C. Pumphrey, M. L. Santee, M. J. Schwartz, P. C. Stek, P. A. Wagner, J. W. Waters, and D. L. Wu, EOS MLS Version 2.2 level 2 data quality and description document, *Technical Report, Version 2.2 D-33509, Jet Propulsion Lab., California Institute of Technology, Pasadena, California, 91198-8099*, 2007.
- Lübken, F.-J., M. J. Jarvis, and G. O. L. Jones, First in situ temperature measurements at the Antarctic summer mesopause, *Geophys. Res. Lett.*, *26*, 3581–3584, 1999.
- Lucchesi, R., File Specification for MERRA Products, *GMAO Office Note No. 1 (Version 2.3)*, 82 pp, available from http://gmao.gsfc.nasa.gov/pubs/office_notes, 2012.
- Manney, G. L., K. Krüger, J. L. Sabutis, S. Amina Sena, and S. Pawson, The remarkable 2003–2004 winter and other recent warm winters in the Arctic stratosphere since the late 1990s, *J. Geophys. Res.*, *110*, D04107, doi:10.1029/2004JD005367, 2005.
- Manney, G. L., K. Krüger, S. Pawson, K. Minschwaner, M. J. Schwartz, W. H. Daffer, N. J. Livesey, M. G. Mlynczak, E. E. Remsberg, J. M. Russell, and J. W. Waters, The evolution of the stratopause during the 2006 major warming: Satellite data and assimilated meteorological analyses, *J. Geophys. Res.*, *113*(D11), doi:10.1029/2007JD009097, 2007.
- Manney, G. L., M. J. Schwartz, K. Krüger, M. L. Santee, S. Pawson, J. N. Lee, W. H. Daffer, R. A. Fuller, and N. J. Livesey, Aura Microwave Limb Sounder observations of

- dynamics and transport during the record-breaking 2009 Arctic stratospheric major warming, *Geophys. Res. Lett.*, *36*(12), doi:10.1029/2009GL038586, 2009.
- Manson, A. H., C. Meek, T. Chshyolkova, C. McLandress, S. K. Avery, D. C. Fritts, C. M. Hall, W. K. Hocking, K. Igarashi, J. W. MacDougall, Y. Murayama, C. Rigin, D. Thorsen, and R. A. Vincent, Winter warmings, tides and planetary waves: comparisons between CMAM (with interactive chemistry) and MFR-MetO observations and data, *Ann. Geophys.*, *24*(10), 2493–2518, doi:10.5194/angeo-24-2493-2006, 2006.
- Manson, A. H., C. E. Meek, X. Xu, T. Aso, J. R. Drummond, C. M. Hall, W. K. Hocking, M. Tsutsumi, and W. E. Ward, Characteristics of Arctic winds at CANDAC-PEARL (80°N, 86°W) and svalbard (78°N, 16°E) for 2006/2009: radar observations and comparisons with the model CMAM-DAS, *Ann. Geophys.*, *29*(10), 1927–1938, doi:10.5194/angeo-29-1927-2011, 2011.
- Matsuno, T., A dynamical model of the stratospheric sudden warming, *J. Atmos. Sci.*, *28*(8), 1479–1494, doi:10.1175/1520-0469(1971)028<1479:ADMOTS>2.0.CO;2, 1971.
- Matthias, V., P. Hoffmann, M. Rapp, and G. Baumgarten, Composite analysis of the temporal development of waves in the polar MLT region during stratospheric warmings, *J. Atmos. Solar-Terr. Phys.*, *90 – 91*, 86 – 96, doi:10.1016/j.jastp.2012.04.004, 2012a.
- Matthias, V., T. G. Shepherd, P. Hoffmann, and M. Rapp, Characteristics of the Hiccup of the fall transition, in *Proceedings of the Thirteenth International Workshop on Technical and Scientific Aspects of MST Radar*, 19-23 March 2012, Kühlungsborn, Germany, accepted for publication, 2012b.
- Matthias, V., P. Hoffmann, A. Manson, C. Meek, G. Stober, P. Brown, and M. Rapp, The impact of planetary waves on the latitudinal displacement of sudden stratospheric warmings, *Ann. Geophys.*, *31*(8), 1397–1415, doi:10.5194/angeo-31-1397-2013, 2013.
- Meek, C. E., and A. H. Manson, Mesospheric motions observed by simultaneous medium-frequency interferometer and spaced antenna experiments, *J. Geophys. Res.*, *92*(D5), 5627–5639, doi:10.1029/JD092iD05p05627, 1987.
- Mukhtarov, P., D. Pancheva, B. Andonov, N. J. Mitchell, E. Merzlyakov, W. Singer, W. Hocking, C. Meek, A. Manson, and Y. Murayama, Large-scale thermodynamics of the stratosphere and mesosphere during the major stratospheric warming in 2003/2004, *J. Atmos. Solar-Terr. Phys.*, *69*(17-18), 2338–2354, doi:10.1016/j.jastp.2007.07.012, 2007.
- Naito, Y., and S. Yoden, Behavior of Planetary Waves before and after Stratospheric Sudden Warming Events in Several Phases of the Equatorial QBO, *J. Atmos. Sci.*, *63*, 1637 – 1649, doi:10.1175/JAS3702.1, 2006.

Bibliography

- NASA, Formation Flying: The Afternoon A-Train Satellite Constellation, *Tech. Rep. FS-2003-1-053-GSFC*, Goddard Space Flight Center, Greenbelt, Maryland 20771, A-Train fact sheet, http://aqua.nasa.gov/doc/pubs/A-Train_Fact_sheet.pdf, 2003.
- Nash, E. R., P. A. Newman, J. E. Rosenfield, and M. R. Schoeberl, An objective determination of the polar vortex using Ertel's potential vorticity, *J. Geophys. Res.*, *101*(D5), 9471–9478, doi:10.1029/96JD00066, 1996.
- Offermann, D., P. Hoffmann, P. Knieling, R. Koppmann, J. Oberheide, D. M. Riggan, V. M. Tunbridge, and W. Steinbrecht, Quasi 2 day waves in the summer mesosphere: Triple structure of amplitudes and long-term development, *J. Geophys. Res.*, *116*(D4), doi:10.1029/2010JD015051, 2011.
- Orsolini, Y. J., J. Urban, D. P. Murtagh, S. Lossow, and V. Limpasuvan, Descent from the polar mesosphere and anomalously high stratopause observed in 8 years of water vapor and temperature satellite observations by the Odin Sub-Millimeter Radiometer, *J. Geophys. Res.*, *115*(D12), doi:10.1029/2009JD013501, 2010.
- Palo, S. E., J. M. Forbes, X. Zhang, J. M. Russell III, C. J. Mertens, M. G. Mlynczak, G. B. Burns, P. J. Espy, and T. D. Kawahara, Planetary wave coupling from the stratosphere to the thermosphere during the 2002 southern hemisphere pre-stratwarm period, *Geophys. Res. Lett.*, *32*, L23809, doi:10.1029/2005GL024298, 2005.
- Pancheva, D., Quasi-2-day wave and tidal variability observed over Ascension Island during January/February 2003, *J. Atmos. Solar-Terr. Phys.*, *68*(3-5), 390–407, doi:10.1016/j.jastp.2005.02.028, 2006.
- Pancheva, D., E. Merzlyakov, N. Mitchell, Y. Portnyagin, A. Manson, C. Jacobi, C. Meek, Y. Luo, R. Clark, W. Hocking, J. MacDougall, H. Muller, D. Kürschner, G. Jones, R. Vincent, I. Reid, W. Singer, K. Igarashi, G. Fraser, A. Fahrutdinova, A. Stepanov, L. Poole, S. Malinga, B. Kashcheyev, and A. Oleynikov, Global-scale tidal variability during the PSMOS campaign of June–August 1999: interaction with planetary waves, *J. Atmos. Solar-Terr. Phys.*, *64*(17), 1865 – 1896, doi: [http://dx.doi.org/10.1016/S1364-6826\(02\)00199-2](http://dx.doi.org/10.1016/S1364-6826(02)00199-2), 2002.
- Pancheva, D., N. Mitchell, A. Manson, C. Meek, C. Jacobi, Y. Portnyagin, E. Merzlyakov, W. Hocking, J. MacDougall, W. Singer, K. Igarashi, R. Clark, D. Riggan, S. Franke, D. Kürschner, A. Fahrutdinova, A. Stepanov, B. Kashcheyev, A. Oleynikov, and H. Muller, Variability of the quasi-2-day wave observed in the MLT region during the PSMOS campaign of June–August 1999, *J. Atmos. Solar-Terr. Phys.*, *66*(6–9), 539 – 565, doi:<http://dx.doi.org/10.1016/j.jastp.2004.01.008>, 2004.
- Pancheva, D., P. Mukhtarov, N. J. Mitchell, B. Andonov, E. Merzlyakov, W. Singer, Y. Murayama, S. Kawamura, J. Xiong, W. Wan, W. K. Hocking, D. Fritts, D. Riggan, C. E. Meek, and A. H. Manson, Latitudinal wave coupling of the stratosphere and mesosphere during the major stratospheric warming in 2003/2004, *Ann. Geophys.*, *26*(3), 467–483, doi:10.5194/angeo-26-467-2008, 2008a.

- Pancheva, D., P. Mukhtarov, N. J. Mitchell, E. Merzlyakov, A. K. Smith, B. Andonov, W. Singer, W. K. Hocking, C. E. Meek, A. H. Manson, and Y. Murayama, Planetary waves in coupling the stratosphere and mesosphere during the major stratospheric warming in 2003/2004, *J. Geophys. Res.*, *113*, D12105, doi:10.1029/2007JD009011, 2008b.
- Pancheva, D., P. Mukhtarov, and B. Andonov, Global structure, seasonal and interannual variability of the migrating semidiurnal tide seen in the SABER/TIMED temperatures (2002–2007), *Ann. Geophys.*, *27*(2), 687–703, doi:10.5194/angeo-27-687-2009, 2009a.
- Pancheva, D., P. Mukhtarov, B. Andonov, N. J. Mitchell, and J. M. Forbes, Planetary waves observed by TIMED/SABER in coupling the stratosphere-mesosphere-lower thermosphere during the winter of 2003/2004: Part 2–Altitude and latitude planetary wave structure, *J. Atmos. Solar-Terr. Phys.*, *71*(1), 75 – 87, doi:10.1016/j.jastp.2008.09.027, 2009b.
- Pancheva, D., R. Mukhtarov, B. Andonov, N. J. Mitchell, and J. M. Forbes, Planetary waves observed by TIMED/SABER in coupling the stratosphere-mesosphere-lower thermosphere during the winter of 2003/2004: Part 1–Comparison with the UKMO temperature results, *J. Atmos. Solar-Terr. Phys.*, *71*(1), 61 – 74, doi:10.1016/j.jastp.2008.09.016, 2009c.
- Pedatella, N. M., T. Fuller-Rowell, H. Wang, H. Jin, Y. Miyoshi, H. Fujiwara, H. Shinagawa, H.-L. Liu, F. Sassi, H. Schmidt, V. Matthias, and L. Goncharenko, The neutral dynamics during the 2009 sudden stratosphere warming simulated by different whole atmosphere models, *J. Geophys. Res.*, *119*(2), 1306–1324, doi:10.1002/2013JA019421, 2014.
- Picone, J. M., A. E. Hedin, D. P. Drob, and A. C. Aikin, NRLMSISE-00 empirical model of the atmosphere: Statistical comparisons and scientific issues, *J. Geophys. Res.*, *107*(A12), SIA 15–1–SIA 15–16, doi:10.1029/2002JA009430, 2002.
- Plumb, R. A., Baroclinic instability of the summer mesosphere: A mechanism for the quasi-two-day wave?, *J. Atmos. Sci.*, *40*(1), 262 – 270, doi:10.1175/1520-0469(1983)040<0262:BIOTSM>2.0.CO;2, 1983.
- Plumb, R. A., On the Three-Dimensional Propagation of Stationary Waves, *J. Atmos. Sci.*, *42*, 217–229, doi:10.1175/1520-0469(1985)042<0217:OTTDPO>2.0.CO;2, 1985.
- Polavarapu, S., S. Ren, Y. Rochon, D. Sankey, N. Ek, J. Koshyk, and D. Tarasick, Data assimilation with the canadian middle atmosphere model, *Atmosphere-Ocean*, *43*(1), 77–100, doi:10.3137/ao.430105, 2005.
- Polvani, L. M., and D. W. Waugh, Upward Wave Activity Flux as a Precursor to Extreme Stratospheric Events and Subsequent Anomalous Surface Weather Regimes, *J. Climate*, *17*(18, 0894-8755), 3548 – 3554, doi:10.1175/1520-0442(2004)017<3548:UWAFAA>2.0.CO;2, 2004.

Bibliography

- Quiroz, R. S., The warming of the upper stratosphere in february 1966 and the associated structure of the mesosphere, *Mon. Weather Rev.*, *97*(8), 541–552, doi:10.1175/1520-0493(1969)097<0541:TWOTUS>2.3.CO;2, 1969.
- Rienecker, M. M., M. J. Suarez, R. Gelaro, R. Todling, J. Bacmeister, E. Liu, M. G. Bosilovich, S. D. Schubert, L. T. G.-K. Kim, S. Bloom, J. Chen, D. Collins, A. Conaty, A. da Silva, W. Gu, J. Joiner, R. D. Koster, R. Lucchesi, A. Molod, T. Owens, S. Pawson, P. Pegion, C. R. Redder, R. Reichle, F. R. Robertson, A. G. Ruddick, M. Sienkiewicz, and J. Woollen, MERRA: NASA’s Modern-Era Retrospective Analysis for Research and Applications, *J. Climate*, *24*, doi:10.1175/JCLI-D-11-00015.1, 2011.
- Rossby, C.-G., Relation between variations in the intensity of the zonal circulation of the atmosphere and the displacements of the semipermanent centers of action, *J. Mar. Res.*, *2*, 38 – 55, 1939.
- Scherhag, R., Die explosionsartige Stratosphärenerwärmung des Spätwinters 1951/52, *Ber. Deut. Wetterdienst*, *38*, 51–63, 1952.
- Schoeberl, M., A. Douglass, E. Hilsenrath, P. Bhartia, R. Beer, J. Waters, M. Gunson, L. Froidevaux, J. Gille, J. Barnett, P. Levelt, and P. DeCola, Overview of the eos aura mission, *Geoscience and Remote Sensing, IEEE Transactions on*, *44*(5), 1066 – 1074, doi:10.1109/TGRS.2005.861950, 2006.
- Schwartz, M. J., A. Lambert, G. L. Manney, W. G. Read, N. J. Livesey, L. Froidevaux, C. O. Ao, P. F. Bernath, C. D. Boone, R. E. Cofield, W. H. Daffer, B. J. Drouin, E. J. Fetzer, R. A. Fuller, R. F. Jarnot, J. H. Jiang, Y. B. Jiang, B. W. Knosp, K. Krüger, J.-L. F. Li, M. G. Mlynczak, S. Pawson, J. M. Russell, M. L. Santee, W. V. Snyder, P. C. Stek, R. P. Thurstans, A. M. Tompkins, P. A. Wagner, K. A. Walker, J. W. Waters, and D. L. Wu, Validation of the Aura Microwave Limb Sounder temperature and geopotential height measurements, *J. Geophys. Res.*, *113*, doi:10.1029/2007JD008783, 2008.
- Scinocca, J. F., N. A. McFarlane, M. Lazare, J. Li, and D. Plummer, The CCCma third generation AGCM and its extension into the middle atmosphere, *Atmos. Chem. Phys. Discuss.*, *8*(2), 7883–7930, doi:10.5194/acpd-8-7883-2008, 2008.
- Shepherd, G. G., G. Thuillier, W. A. Gault, B. H. Solheim, C. Hersom, J. M. Alunni, J.-F. Brun, S. Brune, P. Charlot, L. L. Cogger, D.-L. Desaulniers, W. F. J. Evans, R. L. Gattinger, F. Girod, D. Harvie, R. H. Hum, D. J. W. Kendall, E. J. Llewellyn, R. P. Lowe, J. Ohrt, F. Pasternak, O. Peillet, I. Powell, Y. Rochon, W. E. Ward, R. H. Wiens, and J. Wimperis, WINDII, the wind imaging interferometer on the Upper Atmosphere Research Satellite, *J. Geophys. Res.*, *98*(D6), 10,725–10,750, doi:10.1029/93JD00227, 1993.
- Shepherd, G. G., J. Stegman, P. Espy, C. McLandress, G. Thuillier, and R. H. Wiens, Springtime transition in lower thermospheric atomic oxygen, *J. Geophys. Res.*, *104*(A1), 213–223, doi:10.1029/98JA02831, 1999.

- Shepherd, M., D. Wu, I. Fedulina, S. Gurubaran, J. Russell, M. Mlynczak, and G. Shepherd, Stratospheric warming effects on the tropical mesospheric temperature field, *J. Atmos. Solar-Terr. Phys.*, *69*(17 – 18), 2309 – 2337, doi:10.1016/j.jastp.2007.04.009, 2007.
- Singer, W., P. Hoffmann, A. H. Manson, C. E. Meek, R. Schminder, D. Kürschner, G. A. Kokin, A. K. Knyazev, Y. I. Portnyagin, N. A. Makarov, A. N. Fakhruddinova, V. V. Sidorov, G. Cevolani, H. G. Muller, E. S. Kazimirovsky, V. A. Gaidukov, R. R. Clark, R. P. Chebotarev, and Y. Karadjaev, The wind regime of the mesosphere and lower thermosphere during the DYANA campaign - I. Prevailing winds, *J. Atmos. Terr. Phys.*, *56*, 1717–1729, doi:10.1016/0021-9169(94)90006-X, 1994.
- Singer, W., D. Keuer, and W. Eriksen, The ALOMAR MF Radar : Technical Design and First Results, in *European Rocket and Balloon Programmes and Related Research*, *ESA Special Publication*, vol. 397, edited by B. Kaldeich-Schürmann, pp. 101–104, 1997.
- Singer, W., J. Bremer, W. K. Hocking, J. Weiss, R. Latteck, and M. Zecha, Temperature and wind tides around the summer mesopause at middle and Arctic latitudes, *Adv. Space Res.*, *31*(9), 2055–2060, doi:10.1016/S0273-1177(03)00228-X, 2003.
- Siskind, D. E., L. Coy, and P. Espy, Observations of stratospheric warmings and mesospheric coolings by the TIMED SABER instrument, *Geophys. Res. Lett.*, *32*, L09804, doi:10.1029/2005GL022399, 2005.
- Stober, G., C. Jacobi, V. Matthias, P. Hoffmann, and M. Gerding, Neutral air density variations during strong planetary wave activity in the mesopause region derived from meteor radar observations, *J. Atmos. Solar-Terr. Phys.*, *74*(0), 55 – 63, doi: 10.1016/j.jastp.2011.10.007, 2012.
- Taylor, M. J., W. R. Pendleton, H.-L. Liu, C. Y. She, L. C. Gardner, R. G. Roble, and V. Vasoli, Large amplitude perturbations in mesospheric OH Meinel and 87-km Na lidar temperatures around the autumnal equinox, *Geophys. Res. Lett.*, *28*(9), 1899–1902, doi:10.1029/2000GL012682, 2001.
- Torrence, C., and G. P. Compo, A practical guide to wavelet analysis, *Bull. Amer. Meteorol. Soc.*, *79*(1), 61–78, doi:10.1175/1520-0477(1998)079\$<\$0061:APGTWA\$>2.0.CO;2, 1998.
- Tunbridge, V. M., D. J. Sandford, and N. J. Mitchell, Zonal wave numbers of the summertime 2 day planetary wave observed in the mesosphere by EOS Aura Microwave Limb Sounder, *J. Geophys. Res.*, *116*, D11103, doi:10.1029/2010JD014567, 2011.
- Wang, L., and M. J. Alexander, Gravity wave activity during stratospheric sudden warmings in the 2007/2008 Northern Hemisphere winter, *J. Geophys. Res.*, *114*, D18108, doi:10.1029/2009JD011867, 2009.
- Waters, J. W., L. Froidevaux, R. S. Harwood, R. F. Jarnot, H. M. Pickett, W. G. Read, P. H. Siegel, R. E. Cofield, M. J. Filipiak, D. A. Flower, J. R. Holden, G. K. Lau,

Bibliography

- N. J. Livesey, G. L. Manney, H. C. Pumphrey, M. L. Santee, D. L. Wu, D. T. Cuddy, R. R. Lay, M. S. Loo, V. S. Perun, M. J. Schwartz, P. C. Stek, R. P. Thurstans, M. A. Boyles, K. M. Chandra, M. C. Chavez, G.-S. Chen, B. V. Chudasama, R. Dodge, R. A. Fuller, M. A. Girard, J. H. Jiang, Y. Jiang, B. W. Knosp, R. C. LaBelle, J. C. Lam, K. A. Lee, D. Miller, J. E. Oswald, N. C. Patel, D. M. Pukala, O. Quintero, D. M. Scaff, W. Van Snyder, M. C. Tope, P. A. Wagner, and M. J. Walch, The Earth Observing System Microwave Limb Sounder (EOS MLS) on the Aura Satellite, *Geoscience and Remote Sensing, IEEE Transactions on*, *44*(5), 1075–1092, doi:10.1109/TGRS.2006.873771, 2006.
- Wu, D. L., P. B. Hays, and W. R. Skinner, Observations of the 5-day wave in the mesosphere and lower thermosphere, *Geophys. Res. Lett.*, *21*(24), 2733–2736, doi:10.1029/94GL02660, 1994.
- Wu, D. L., P. B. Hays, and W. R. Skinner, A Least Squares Method for Spectral Analysis of Space-Time Series, *J. Atmos. Sci.*, *52*(20), 3501–3511, doi:10.1175/1520-0469(1995)052<3501:ALSMFS>2.0.CO;2, 1995.
- Yoden, S., T. Yamaga, S. Pawson, and U. Langematz, A composite analysis of the stratospheric sudden warmings simulated in a perpetual January integration of the Berlin TSM GCM, *J. Met. Soc. Japan*, *77*, 431–445, 1999.
- Yoo, J.-M., Y.-I. Won, M.-J. Jeong, K.-M. Kim, D.-B. Shin, Y.-R. Lee, and Y.-J. Cho, Intensity of Climate Variability Derived from the Satellite and MERRA Reanalysis Temperatures: AO, ENSO, and QBO, *J. Atmos. Solar-Terr. Phys.*, doi:10.1016/j.jastp.2013.01.002, 2013.
- Zülicke, C., and E. Becker, The structure of the mesosphere during sudden stratospheric warmings in a global circulation model, *J. Geophys. Res.*, doi:10.1002/jgrd.50219, 2013.

Acknowledgements

First I would like to thank my supervisor Prof. Markus Rapp and the director Prof. Franz-Josef Lübken for giving me the great opportunity to work at the IAP. The ideas of Markus Rapp and my discussions with him have contributed not only this thesis very much. My special thanks goes to Peter Hoffmann. In our countless discussions we found solutions for problems occurring during the data analysis and discussed the geophysics behind the results. His support has been very important for finishing my thesis. I also want to thank my colleagues Manja Placke and Gunter Stober for their interdisciplinary and sometimes funny discussions and the rest of the radar department for providing the radar data and the friendly environment. I would like to thank Christoph Zülicke, Axel Gabriel and Erich Becker for their helpful discussions especially on the theoretical background of planetary waves. My thanks goes also to Jens Hildebrand who helped me to solve my \LaTeX problems and who proof reads my thesis. Also many thank to the second careful proofreader of my thesis Timo Viehl.

I also thank the Jet Propulsion Laboratory/NASA for providing access to the Aura/MLS level 2.2 retrieval products and acknowledge the Global Modeling and Assimilation Office (GMAO) and the GES DISC for the dissemination of MERRA. Additionally, I gratefully acknowledge the European Centre for Medium-Range Weather Forecasts (ECMWF) for providing ERA-Interim data and the Canadian Space Agency through the CMAM20 project. In this context I want to thank Gerd Baumgarten for providing the ECMWF and MERRA data.

Finally, I want to thank my parents Simone and Hans-Joachim as well as my sister Adrienne for their continuous help and support not only during my work.

Curriculum Vitae

Name	Vivien Matthias
Date of Birth	5th September 1984
Place of Birth	Berlin, Germany

Education

since 04/2010	Dissertation at the Leibniz-Institute of Atmospheric Physics e.V. at the University of Rostock. “The role of planetary waves in coupling processes of the middle atmosphere”
10/2004 – 11/2009	Diploma in Mathematics at the Otto-von-Guericke-University Magdeburg
08/1997 – 07/2004	Abitur, Marie-Curie-Gymnasium Hohen Neuendorf

Work experience

09/2011 – 12/2011	Stay abroad at the University of Toronto due to a collaboration with Theodore G. Shepherd to elaborate the topic “Characteristics of the "Hiccup" of the fall transition”
05/2009 – 11/2009	Diploma thesis at the Otto-von-Guericke-University Magdeburg. Title: “Nachweis der starken Sperner-Eigenschaft mittels $sl(2, \mathbb{C})$ -Darstellungen”
02/2009 – 03/2009	Practical training at the German Aerospace Center (DLR) in Braunschweig: “Is it possible for an aircraft to fly in the danger area of its own wake vortex during a spiral descent?”
04/2007 – 08/2008	Tutor at the faculty of mathematics at the Otto-von-Guericke-University Magdeburg

Erklärung

Hiermit versichere ich an Eides statt, die vorgelegte Arbeit selbstständig und ohne fremde Hilfe verfasst, keine außer den von mir angegebenen Hilfsmitteln und Quellen dazu verwendet und die den benutzten Werken inhaltlich und wörtlich entnommenen Stellen als solche kenntlich gemacht zu haben.

Die Arbeit wurde bisher weder im Inland noch im Ausland in gleicher oder ähnlicher Form einer anderen Prüfungsbehörde vorgelegt. Weiterhin erkläre ich, dass ich ein Verfahren zur Erlangung des Doktorgrades an keiner anderen wissenschaftlichen Einrichtung beantragt habe.

Kühlungsborn, den 21.11.2013

(Vivien Matthias)